SELF-ASSEMBLY OF POLYSTYRENE-POLY(ETHYLENE OXIDE) BLOCK COPOLYMERS AND POLYMER-STABILIZED CADMIUM SULFIDE NANOPARTICLES AT THE AIR-WATER INTERFACE: PATTERNING SURFACE FEATURES FROM THE BOTTOM UP

By

Robert Bruce Cheyne
B.Sc., The University of Victoria, 2003

A Thesis Submitted in Partial Fulfillment of the
Requirements for the Degree of

MASTER of SCIENCE

in the Department of Chemistry

ABSTRACT

The self-assembly and interfacial behaviour of two relatively hydrophobic PS-*b*-PEO diblock copolymers at the air-water interface are studied as a function of spreading solution concentration. For PS-*b*-PEO(11.4%) (11.4 wt.% PEO), atomic force microscopy (AFM) on Langmuir-Blodgett (LB) films formed at the interface show a marked dependence of aggregate morphology on spreading concentration, with dots and spaghetti aggregates being observed for all spreading concentrations, and two novel morphologies, rings and chains, being found below a critical concentration of spreading solution ($\leq$ 0.25 mg/mL). Complimentary investigations into the effect of spreading solution concentration on the surface pressure (π) – area (A) isotherms of both copolymers, PS-*b*-PEO(11.4%) and PS-*b*-PEO(18.9%), suggest that the PS aggregates at the surface are less densely-packed, with greater PEO adsorption under the aggregates, below the critical spreading concentration. We use AFM evidence to suggest a new mechanism for the formation of PS-*b*-PEO aggregates at the air-water interface, which starts with dewetting of an evaporating polymer solution, leading to the formation of a cellular network of holes and rims, followed by the breakdown of the rims into various morphologies, depending on the extent of chain entanglements before vitrification of the polymer. The self-assembling properties of the amphiphilic PS-*b*-PEO diblock copolymers are also used to direct the organization of polymer-stabilized cadmium sulfide nanoparticles (PS-CdS) at the air-water interface. This novel, nonlithographic technique produces a range of interesting NP / polymer superstructures, including nanocables, branched nanowires and nanorings with an even distribution of NPs throughout the polymer matrix. A combination of AFM and transmission electron microscopy (TEM) highlights the unique structural hierarchy of these NP / polymer hybrid features, which combine NP organization on a combination of vastly disparate length scales via a single self-assembly step.

Supervisor: Dr. M. G. Moffitt (Department of Chemistry)

Acknowledgements

This thesis is dedicated to the late Douglas Cheyne for instilling in me the ability to face adversity with the utmost optimism; a quality that has afforded me the opportunity to complete this work despite the inevitable setbacks that come with research
--- *and life*.

I would like to express my most sincere thanks to Professor Matthew Moffitt for his infectious enthusiasm that has driven me to push myself to become a better scientist and person. Without his efforts and understanding, my achievements would not have been possible.

I cannot give enough thanks to my parents, Bob and Lynn, and my brothers Ian and Jay, for their unqualified love and support, especially in this last year. Their consistent encouragement throughout my work truly inspired me.

My grandparents, Lois and Bruce Buchanan, showed genuine interest in my work and challenged my curiosity. Verna and Doug Cheyne instilled in me the belief that with hard work and a little humour, I can accomplish anything.

The Dawson family must be thanked for their unparalleled affection and for keeping my spirits boosted and life balanced over the years. I drew on their strength during the many long hours.

In addition, I would like to thank:

My group members; Jo Wang, who so charitably supplied the PS-*b*-PtBA starting material, and Huda Yusuf and Yunyong Guo for their kind support over the years.

Professor Frank van Veggel for kindly sharing the AFM and to Peter Diamente for his patient training on the instrument. My work certainly could not have been completed without their generosity.

Our resident antiquarian Brent Gowen, for his help with the TEM.

All the Chemistry Faculty and staff and fellow graduate students. They all made my time at UVic a truly wonderful experience.

And last but certainly not least, to my faithful buddies for religiously calling me from the Peak every time Whistler Mountain got more than 5 cm of snow. I will always be there for you

"In my experience, the glittering prizes in life come more to those who persevere despite setback and disappointment than they do to the exceptionally gifted who, with the confidence of the talents bestowed upon them, often pursue the tasks leading to success with less determination."

Bryce Courtenay "*The Power of One*"

Table of Contents

CHAPTER 2

CHAPTER 3

List of Schemes and Figures

List of Tables

Chapter 1

General Introduction

1.1. Introduction

Semiconducting or metallic nanoparticles (NPs) feature unique size-dependant optical, electronic and chemical properties arising from their high surface-to-volume ratios and quantum confinement effects.[1-10] The size-tunable luminescent properties of these colloidal particles make them promising candidates as the ultimate miniature devices,[11] with potential applications in fields ranging from optoelectronics[12] and sensing,[13] to catalysis and medicine.[14] In order to exploit the favourable properties afforded by these NPs in specific device applications, it is necessary to gain control over their assembly at multiple length scales. Inorganic NPs are notoriously insoluble in organic media, a property that severely impedes their processability and implementation into functional devices. To counter this effect, the surface of NPs are often passivated with an organic[15] or polymer[16] layer resulting in a colloidal species with superior performance over a wide range of environmental conditions. Functionalization of NPs with a polymer layer offers the additional advantage of increasing their compatibility within an external polymer matrix; as many future NP-based devices will require the functional NP core to be dispersed within a medium of desirable mechanical and optical properties. Despite important advances in the surface functionalization of metal and semiconducting NPs, their controlled assembly into one-, two-, and three-dimensional (1D, 2D, 3D) arrays organized on multiple length scales remains at the limit of modern scientific knowledge.

There exist two main approaches to controlled assembly and pattern formation as modern science begins to converge on control at the nano-level: the "top-down," or lithographic approach, and the "bottom-up" or self-assembly approach.[17] Lithographic

tactics[18] rely on the design and use of sophisticated instruments to externally direct the assembly of atoms or molecules into predetermined arrangements. This approach has proved to be extremely useful in a myriad of applications ranging from the positioning of single atoms on solid surfaces,[19] to the construction of the first computer chip capable of holding 10^{12} bytes of information per square inch.[20] As conventional lithographic processes are inherently energy intensive, inefficient, and expensive, an increasing amount of scientific focus has centered on nonlithographic techniques. Nature has proven that the self-assembly approach can be exceedingly efficient[21] and has inspired an immense amount of research in this area. Current research is largely focused on identifying relevant materials with properties that may be exploited at the molecular level, and understanding how these materials behave under various conditions in an effort to achieve molecular control over various dimensions and length scales.

An interesting and important class of molecules that combines the physical properties of polymers with self-assembling characteristics are amphiphilic diblock copolymers. A wealth of research on amphiphilic diblock copolymers has shown that when they are deposited at the air-water interface, the hydrophilic blocks spontaneously orient towards the water subphase, whereas the hydrophobic blocks face the air, and tend to aggregate into a range of surface features.[22-44] Depending on the composition, and relative lengths of the blocks, various surface morphologies have been observed, and are tunable by varying these parameters. For example, when polystyrene-*block*-poly(ethylene oxide) (PS-*b*-PEO) is deposited from a non-selective solvent at the air-water interface, spontaneous assembly occurs resulting in a range of structures including 0-dimensional 'dots', 1-dimensional 'spaghetti' wires and 2-dimensional, planar

'continents'.[39-42] It has been shown that dots are commonly observed for more hydrophilic diblocks, and a mixture of dots, spaghetti, and planar continents for more hydrophobic diblocks.[39-42] It has also been shown that the predominance of these various PS-*b*-PEO surface morphologies are tunable by controlling the spreading solution concentration.[42]

The idea behind this work was to harness the self-assembling properties of a PS-*b*-PEO diblock copolymer, in order to direct the organization of photoluminescent cadmium sulfide (CdS) NPs into low-dimensional NP / polymer surface features. To accomplish this goal, we first considered the spontaneous self-assembly of pure PS-*b*-PEO diblock copolymers at the air-water interface, as described in the first part of this thesis, with particular emphasis on the effect of spreading solution concentration on the structure of the aggregates. The surface features formed at the air-water interface were transferred to glass substrates via the Langmuir-Blodgett (LB) technique and imaged with atomic force microscopy (AFM). Additionally, self-assembled PS-*b*-PEO films were studied at the water surface through compression and expansion isotherms, where the surface pressure (π) was monitored as a function of available area (A) at the interface; these experiments reveal important information on the structure of the aggregates under different spreading conditions. The second part of the thesis demonstrates the feasibility and promise of our original idea, describing the application of PS-*b*-PEO interfacial self-assembly to direct the organization of polymer-stabilized CdS NPs into interesting and resilient hybrid structures at the air-water interface.

The remainder of this chapter is designed to give the reader the background necessary to understand the content of the thesis. Sections 1.2 and 1.3 introduce

polymers, diblock copolymers, and the use of ion-containing block copolymers as a template in the synthesis of inorganic NPs surrounded by a stabilizing polymer brush. Section 1.4 establishes the source of the size-dependent opto-electronic properties displayed by semiconducting NPs through a discussion of the quantum confinement effect. Section 1.5 introduces the air-water interface and its effect on the self-assembly of amphiphilic copolymers, along with describing the various techniques for studying interfacial monolayer films. Section 1.6 is concerned with the salient characterization techniques employed in this thesis, including gel permeation chromatography (GPC), static and dynamic light scattering (SLS and DLS), AFM and TEM. Section 1.7 provides a brief description of the remaining chapters in this thesis.

1.2. General Background

1.2.1. Polymers

Our understanding of polymeric macromolecules has greatly improved since the Nobel Laureate Herman Staudinger first postulated their existence in 1927.[45] Defined as a large molecule constructed from many smaller structural units called monomers, the diversity of properties exhibited by polymers reflects the near limitless possibilities in covalently linking the monomeric units together. There are several levels of characterization that are necessary to unambiguously define a given polymer; however, only the salient characteristics of polymers are considered in the present thesis and the interested reader is referred to other, more detailed sources.[46,47]

An essential characteristic of any polymer sample is the 'size' or 'length' of the macromolecules. An inherent issue concerning synthetic high polymers is that a single

molecular weight is never achieved, and a distribution of molecular weights arises from the random nature of the polymerization events. A typical distribution of molecular weights is provided in Figure 1.

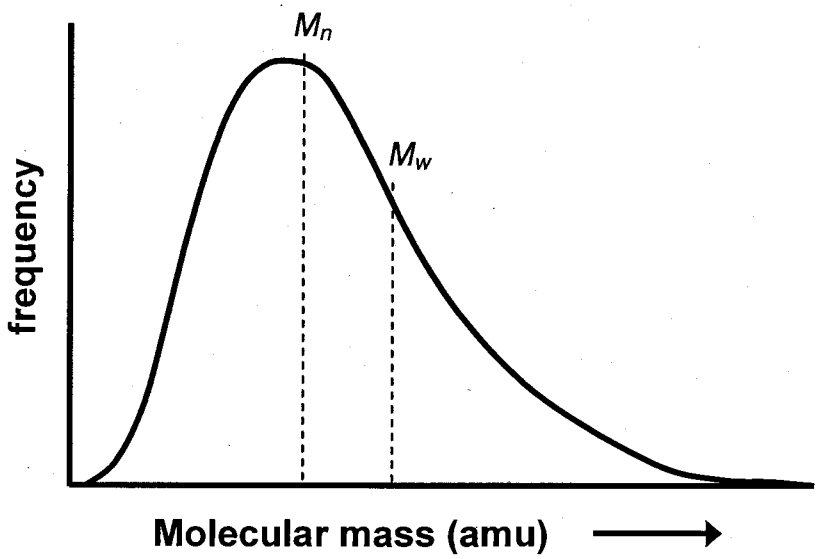

Figure 1.1. Molecular weight distribution of a theoretical polymer sample highlighting the positions of the defined molecular weights

As suggested by the figure, the molecular weight is defined by more than one average value. The number-average molecular weight (M_n) is calculated by taking the weight of the entire sample and dividing this by the total number of molecules present in the sample (Equation 1):

$$M_n = \frac{\sum N_i M_i}{\sum N_i} \qquad \textbf{1.1}$$

where N_i refers to the number of molecules of species i of molecular weight M_i. M_n can be determined from characterization methods sensitive to the total number of molecules in a system (i.e.colligative methods), including vapor pressure lowering, boiling point elevation, freezing point depression and osmotic pressure.

The weight-average molecular weight (M_w) is a larger value than M_n and is defined as:

$$M_w = \frac{\sum W_i M_i}{\sum W_i} = \frac{\sum N_i M_i^2}{\sum N_i M_i} \qquad \textbf{1.2}$$

where W_i is the weight of all molecules of species i with molecular weight M_i. Analytical methods that are sensitive to the sizes, or degree of polymerization, of the molecules are used in the determination of M_w. The most common method employed to measure M_w is light scattering, whereby each macromolecule in a population contributes to the intensity of scattered light relative to its size. Although other molecular weight definitions are also used, including the z-average molecular weight, and the viscosity-average molecular weight, these were not considered here.

From the various definitions of molecular weight, there exist various definitions of the degree of polymerization (x), another very important parameter in polymer chemistry. The degree of polymerization is obtained by dividing an average molecular weight describing the polymer sample by the molecular weight of an individual repeat unit, thus giving the number of repeat units in an average polymer chain. Each of the above molecular weight averages can be used to calculate a degree of polymerization. For example, the number-average degree of polymerization (x_n) is defined as:

$$x_n = \frac{M_n}{M_0} \qquad \textbf{1.3}$$

where M_0 is the molecular weight of an individual repeat unit.

The width of the distribution of molecular weights shown schematically in Figure 1 is quantified by the polydispersity index (P.I.), obtained by dividing M_w by M_n:

$$\text{P.I.} = \frac{M_w}{M_n} \qquad \textbf{1.4}$$

Polymers with very narrow size distributions have P.I. values that approach unity and are said to be relatively monodisperse whereas broad distributions have large P.I. values and are said to be relatively polydisperse. Certain polymerization techniques afford some control over the P.I., thus through judicious choice of reaction conditions it is possible to obtain a polymer product with low polydispersity. Living polymerization processes including anionic polymerization are well known for their narrow size distributions,[48] and often result in P.I. values in the range of 1.01 to 1.10. Step-growth polymerization reactions, including condensation reactions, result in a theoretical P.I. of 2.0, and thus produce a much broader size distribution. As the present study employed polymers synthesized using living, anionic polymerization, this method will be qualitatively described, though a more detailed description[49, 50] is beyond the scope of this work.

1.2.2. Sequential Anionic Polymerization

All addition polymerization techniques involve three distinct processes: *initiation*, where the reactive species are created, *propagation*, where the polymer chain is grown through the addition of monomers, and finally *termination*, where the chain growth is stopped when a species that is incapable of continuing the polymerization is added to the growing chain. What separates living polymerization techniques from other addition polymerization reactions is that the propagating species are resistant to termination or chain transfer reactions.[46] 'Living' systems, for example anionic polymerization, require categorical care and attention to the elimination of impurities like water, molecular oxygen, alcohols, carbon dioxide, etc., which are known to terminate the propagating species and thus 'kill' the reaction. For this reason, anionic polymerization is performed using carefully distilled reagents, in an inert environment, under vacuum.

The monomers used in anionic polymerization reactions are always substituted vinyl molecules; for example, styrene, *tert*-butylacrylate, etc. The polymerization is initiated by electron transfer to the vinyl substituent from an appropriate donor such as *sec*-butyl lithium as described in Scheme 1.1 using styrene as the monomer:

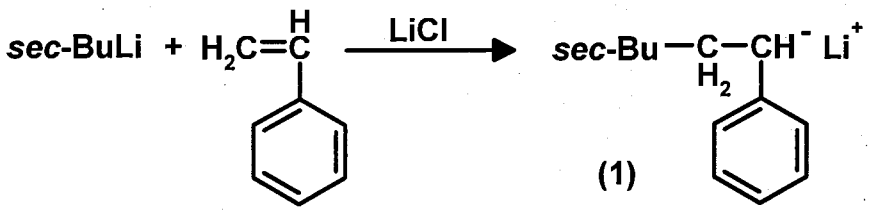

Scheme 1.1. Initiation of styrene with *sec*-butyllithium

The presence of LiCl affords favourable control over the polymerization kinetics.[50] The Li^+ "gegen ion" provides stabilization of the living species in solution, decreasing the tendency of the reactive ends to undergo unfavourable chain termination and chain transfer events.[51-53]

After the initiation, monomers are added to the 'active' solution where they sequentially react with the living terminus of the growing polymer chain created in the initiation step. The propagation step proceeds via addition of unreacted monomer to the living end of the growing polymer as described in Scheme 1.2:

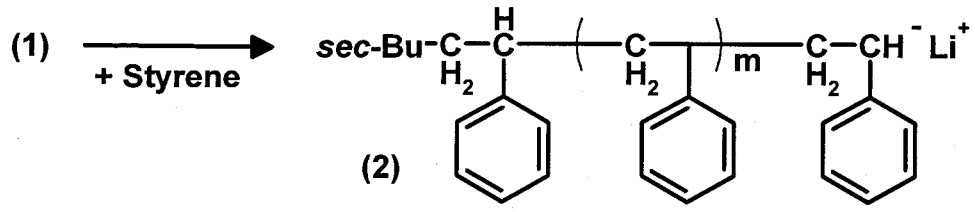

Scheme 1.2. Addition of styrene to activated complex (**1**), where m refers to the number of repeat units with given structure.

As suggested by Scheme 1.2, the living end will persist even after all monomers have reacted. This species may be terminated through the introduction of an appropriate agent such as methanol, which immediately reacts with the living anion and terminates the reaction. If the polymerization is terminated at this point the product would be termed a homopolymer, as the polymer would be made up exclusively of one monomer type. However, addition of a second type of monomer will result in a diblock copolymer, with a chain of one monomer type covalently linked at one end to a chain of the other monomer type. The term copolymer refers to the presence of two types of monomer in a

chain and there are various other classes of copolymers including random copolymers, alternating copolymers, and graft copolymers, but they are not of concern to this thesis and an interested reader is directed to other sources. [46, 47, 54, 55]

Scheme 1.3 illustrates the propagation of a *tert*-butylacrylate (*t*-BA) chain by initial reaction with the living terminus of the polystyrene chain, yielding the diblock copolymer polystyrene-*block*-poly(*tert*-butylacrylate) (PS-*b*-PtBA):

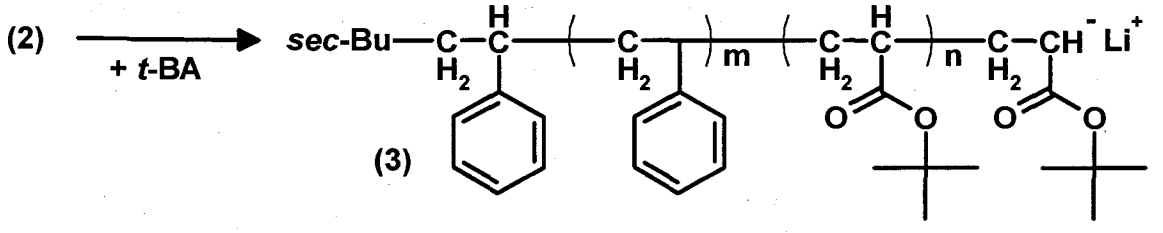

Scheme 1.3. Copolymerization of the active styrene polymer via sequential addition of *tert*-butylacrylate (*t*-BA) to yield polystyrene-*block*-poly(*tert*-butylacrylate) (PS-*b*-PtBA) with m average PS units, and n average PtBA repeat units.

It is possible to continue this sequence of reactions through the addition of a third monomer to yield a triblock copolymer, and so on, but this was not the focus of the present study. To produce the PS-*b*-PtBA polymer used in this work, the species (**3**) was terminated through the addition of methanol.

1.3. Amphiphilic Molecules in Solution

Amphiphilic molecules are important and fundamentally interesting species. They constitute a class of molecules with a hydrophobic part on one end and a hydrophilic part on the other end. An example of an amphiphile is a surfactant molecule with a polar, hydrophilic head group (e.g. carboxylic acid) attached to a hydrophobic alkane tail. These molecules have numerous interesting and applicable properties, many of which go well beyond the scope of this work.[56,57]

Diblock copolymers can be tailor-made to be amphiphilic through judicious choice of the respective blocks. This class of polymeric amphiphile can be designed with specific properties in mind for studies and applications that are not accessible using conventional surfactants and other "small molecule" amphiphiles. These properties are beginning to be applied in a diverse range of fields including polymer-mediated drug delivery,[58] lubrication,[59] adhesion,[60] and generation of three dimensional patterns through microphase separation.[61] Amphiphilic diblock copolymers have also been successfully used to template the synthesis of inorganic NPs,[9,10,16,62,63] an approach which was executed in the present study. Also relevant to this thesis is the property of amphiphilic diblock copolymers to self-assemble into unique, low-dimensional structures when deposited at interfaces that are selective for one of the blocks.[22,23,25-32,39-42,61,64-67]

1.3.1. Micellization of Neutral Diblock Copolymers in Dilute Solution

As detailed discussions of theories pertaining to the micellization of diblock copolymers have been presented elsewhere,[68-70] the purpose of this section is to introduce some useful terminology and concepts of particular relevance to the present study.

When a neutral amphiphilic diblock copolymer is dissolved in a medium that is thermodynamically favourable for one of blocks, the insoluble blocks will attempt to minimize unfavourable enthalpic interactions with the solvent by coming together; the result is a micellar aggregate, or block copolymer micelle, consisting of a relatively dense core of the insoluble blocks surrounded by a brush of the soluble chains, also known as the corona. This process is spontaneous when the concentration of block copolymers in the selective solvent reaches a certain level, known as the critical micelle concentration (CMC). For historical reasons, if the micelles are formed in aqueous media, with a hydrophobic core and a hydrophilic corona, they are referred to as regular micelles; conversely, if the micelles are formed in organic solvent, with a hydrophilic core and a hydrophobic corona, they are known as reverse micelles. Additionally, if the corona-forming block is large with respect to the core-forming block, the micelle is called "star-like," and if the reverse is true they are described as "crew-cut" micelles. These classification schemes are represented pictorially in Figure 1.2.

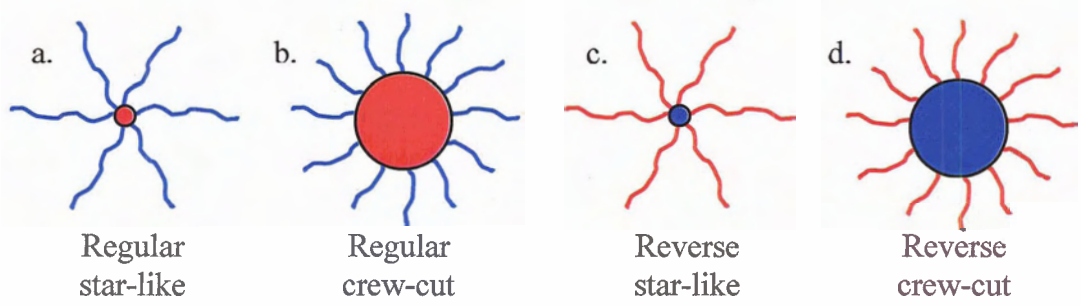

Figure 1.2. Illustrations of the various definitions of amphiphilic diblock copolymer micelles in; (a, b) aqueous solvent, and; (c, d) organic solvent. Red indicates relatively hydrophobic and blue represents the relatively hydrophilic block, respectively.

1.3.2. Micellization of Ionic Diblock Copolymers in Dilute Solution

The blocks forming the core or corona may be neutral or charged. Diblock copolymers that possess a charged block are categorized as ionic block copolymers. Depending on the system, the properties of ionic block copolymers will be affected by either short-range or long-range electrostatic interactions, in the core or within the corona and between micelles. For the present work, an ionic block copolymer was employed to template the synthesis of an inorganic NP, using the metal counterions of a negatively-charged polyacrylate core as precursors in the reaction. This specific example is discussed below.

Polystyrene-*block*-poly(acrylic acid) (PS-*b*-PAA) is soluble in a mixed benzene / methanol solvent system at low pH; however, upon addition of a base ($Cd(CH_3COO)_2$ in the present case), the labile proton on the carboxylic acid group can be removed, thus creating a negatively-charge ionic block. This simple procedure will induce micellization due to extremely unfavourable interactions between the apolar organic solvent and the charged block, forming a block ionomer micelle with a poly(cadmium acrylate) (PACd) core and a polystyrene (PS) corona. This process is schematically illustrated in Scheme 1.4, and has shown to be extremely useful in the synthesis of polymer-stabilized inorganic NPs, as described below.

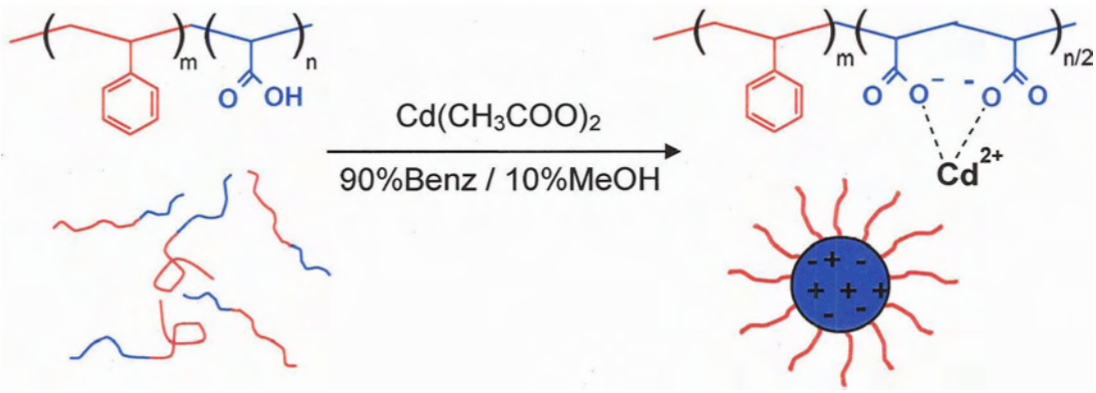

Scheme 1.4. Formation of the block ionomer micelle by selectively removing the acidic proton on the poly(acyrlic acid) (PAA) chain inducing micellization. Top structures detail the chemical before and after addition of $Cd(CH_3COO)_2$ base. Bottom cartoons illustrate the configuration of the diblock copolymers (ionomers) before and after base addition

1.3.3. Block Ionomer Micelles in the Templated Synthesis of Inorganic Nanoparticles

Of particular interest to the present study is the existence of a high local concentration of cadmium ions contained within the micelle core. This ion-containing core provides a discrete region where subsequent chemistry can be performed, and can therefore be regarded as a nanoreactor. Considering Scheme 1.4, it has been shown that the Cd^{2+} counterions in the core can be reacted with H_2S, thus generating a CdS particle with dimensions determined by the amount of Cd^{2+} ions initially present,[62] as described in Scheme 1.5. This template approach therefore offers significant control over the size of the resultant NPs via careful choice of the PAA block length, which determines the aggregation number of the initial block ionomer micelle.[62] An additional advantage of this technique is that the NP is encapsulated and stabilized within a polymer layer,

therefore imparting improved compatibility with polymer media compared to more typical NPs stabilized by small molecule organic ligands (e.g. trioctylphosphine oxide, or TOPO).

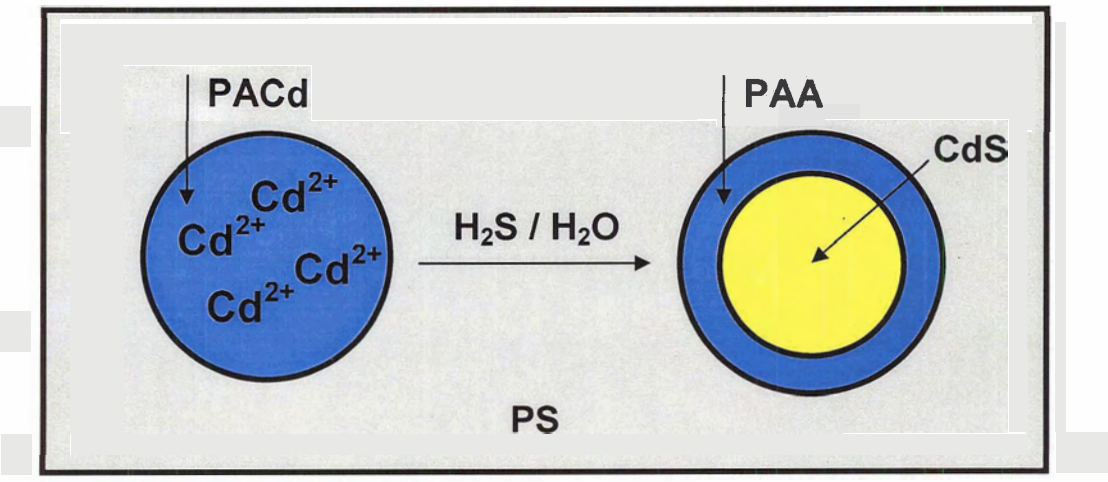

Scheme 1.5. Poly(cadmium acrylate) (PACd) microreactor used in the preparation of a poly(acrylic acid) (PAA) stabilized CdS nanoparticle in a PS matrix (grey background).[64]

1.4. Inorganic Semiconducting Nanoparticles

Inorganic metallic or semiconducting nanoparticles (NPs) are pseudo zero-dimensional particles with dimensions between ca. 1 – 10 nm.[1] The size of these materials therefore falls between that of single atoms and their respective bulk material. Of interest is the fact that the chemical and physical properties of these NPs have properties that are fundamentally different from the bulk material. As scientists begin to understand and exploit these size-dependant properties, a plethora of fundamental experiments and practical applications can be imagined.[71-74]

The size-dependent properties of semiconducting NPs, or quantum dots, are determined mainly by two factors: 1) a significant increase in the relative surface area compared to bulk materials and 2) changes in the electronic structure due to quantum confinement effects.[1-10] The increased surface area has numerous ramifications; for example, drastic reductions in melting points for NPs with respect to the bulk have been observed.[75] Additionally, due to the large percentage of surface atoms, the photoluminescence properties of these NPs can be tuned by simple chemistry at the particle surface.[9,10,15,76-79] The second factor influencing size-dependant properties is the quantum confinement effect, which is examined in Section 1.4.1.

1.4.1. The Quantum Confinement Effect

Given enough energy, an electron in a bulk semiconductor can be promoted into the valence band, leaving a positive hole in the conduction band. This electron - hole pair is termed an exciton and has an energy that is virtually identical to that of the bandgap. When the size of the semiconducting particle is reduced to the size of the Bohr exciton radius, the band structure becomes localized and the energy of the exciton increases.[1] Much theoretical and experimental effort has been made in an attempt to describe this intriguing phenomenon, and for a comprehensive list the interested reader is directed to a recent text on the subject[71] as only the approach of Brus[80] is summarized here. Brus treated the problem using a variant on the classic particle-in-a-box model with the "particle" being the electron and the "box" being the spherical NP. By introducing an infinitely high potential at the surface, the movement of the electron is confined and a

quantum mechanical solution provides the energy states of the system. Brus[80] thus calculated the energy of the first exciton (E^*) in this spherical box of radius R to be:

$$E^* \cong E_g + \frac{\hbar^2\pi^2}{2R^2}\left[\frac{1}{m_e} + \frac{1}{m_h}\right] - \frac{1.8e^2}{\varepsilon R} + \ldots \qquad \textbf{1.5}$$

The bandgap energy of the bulk semiconductor, E_g, is dependant on the material of interest. The second term on the right, the confinement term, arises from the aforementioned quantum mechanical treatment where $\hbar$ is Planck's constant, and m_e and m_h are the effective masses of an electron and a hole. This confinement term is inversely proportional to the squared radius of the NP, and therefore causes an increase in the exciton energy as the particle size decreases. A correction for electron – hole interactions is provided by the third term, the Coulombic interaction term. The Coulomb energy scales as the inverse of the electron – hole distance and has a stabilizing effect on the exciton, resulting in a reduction in the exciton energy as R decreases. This quantum confinement effect is easily probed through absorption spectroscopy, with the absorption spectra being observed to blue-shift as semiconducting NPs decrease in size, due to the predominance of the second term in Equation 1.5.

CdS QDs have proved to be an effective model material for fundamental studies of quantum size effects, since the exciton is in the visible region for most sizes of NPs and is thus easily probed through conventional UV / vis absorption spectroscopy (Figure 1.3).[1] As the exciton diameter is ~ 5.8 nm in bulk CdS, particles larger than this have electronic and optical properties identical to bulk material, and absorb above ~515 nm, corresponding to the bulk CdS bandgap. By decreasing the size of the NP below this

critical threshold, the energy of the exciton increases as shown in Figure 1.3, and in agreement with Equation 1.5.

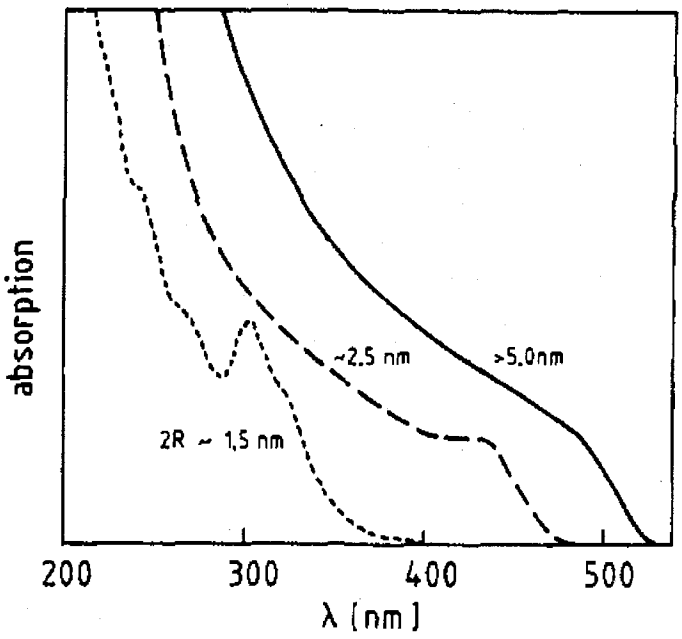

Figure 1.3. UV-Vis absorption spectra of CdS nanoparticles of different mean particle sizes.[1]

1.5. Insoluble Monolayers at the Air-Water Interface

As major focus of this thesis is on the behaviour of molecules at the air-water interface, we now present a brief introduction to the air-water interface, including a description of differences between surfaces and the bulk, surface tension and its measurement, and the behaviour and orientation of insoluble molecules at the air-water interface.

1.5.1. The Air-Water Interface

Surfaces are fundamentally different from bulk materials. Molecules in the bulk (of a liquid for example) are completely surrounded by like molecules, and therefore experience maximum intermolecular forces, equal in all directions. Molecules at the surface experience an imbalance of forces resulting from a larger attraction in the direction of the bulk. The result of this energetic effect is that surface molecules are less stable than bulk molecules, and the liquid tends to minimize their numbers by minimizing the exposed surface area.[81] This property of surfaces is quantified by the surface tension (γ), which has been described as the contractile force which always exists in the boundary between two phases at equilibrium.[82] There are numerous methods available to measure this contractile force and for a complete list the interested reader is directed to several good references.[82-86] One efficient and effective method to measure γ is the Wilhelmy plate method. A thin plate is partially immersed in the subphase (Figure 1.4) and the force resulting from γ at the interface is measured through a sensitive balance.

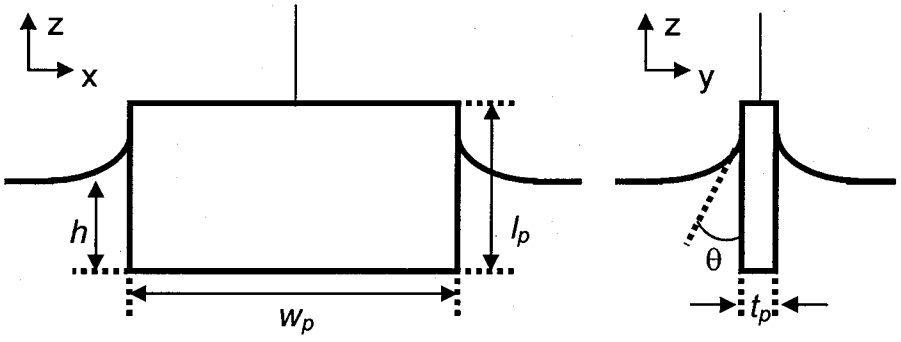

Figure 1.4. Schematic representation of a Wilhelmy plate viewed from two sides and submerged in a subphase

Immediately apparent from Figure 1.4 is that a meniscus exists on the plate with a definable contact angle θ, which is defined as the angle that is formed at the junction of the three phases: solid (the plate), liquid and gas. The manifestation of γ and θ in this situation is the entrainment of a meniscus around the perimeter of the suspended plate, and since the meniscus is held up by the tension on the liquid the weight measured by the apparatus can be analyzed to yield a value for γ.[82]

As this is a static, equilibrium phenomenon, the force (F) acting on the plate results from the weight of the plate, the buoyant force of the displaced water and the γ of the subphase. For our investigation, the change in force (ΔF) acting on the plate is the important parameter, which simplifies the relation by nullifying the weight and buoyancy contributions yielding equation 1.6, after considering the dimensions of the plate.

$$\Delta F = 2(w_p + t_p)\gamma\cos\theta \qquad \textbf{1.6}$$

With the exception of θ, all of the variables in the above expression are easily and independently obtainable. Because θ is often difficult to measure accurately, the Wilhemly plate is generally made of a material (e.g. Pt) that is completely wetted by the subphase yielding a θ of 0, thus the vertical contribution to the force (cos θ) = 1. Additionally the plate is manufactured with $t_p << w_p$, reducing equation 1.6 to:

$$\Delta F \cong 2w_p\gamma \qquad \textbf{1.7}$$

where ΔF is measured through a sensitive balance and directly converted to γ.

1.5.2. Insoluble Monolayers at the Air-Water Interface

Oily films at the air-water interface have had a colourful history. At a 1774 meeting, Benjamin Franklin presented to the Royal Society a description of his famous experiment on Clapham Pond:[85, 87]

> "... the oil, though not more than a teaspoon, produced an instant calm over a space several yards square, which spread amazingly and extended itself gradually till it reached the lee side, making all that a quarter of the pond, perhaps half an acre, as smooth as a looking glass."

An elementary calculation shows that the thickness of the film described by Franklin was minute, ~ 2 nm. It took a century before scientists realized the implications of this observation and since that time much work has been dedicated to understanding the behaviour and manipulation of monomolecular films at interfaces.

For the last 100 years, a major focus has been on the behaviour of amphiphilic molecules at the air-water interface. It is well established that long-chain fatty acids spread on water form thin films that are one molecule thick, oriented with their hydrophilic acid component (the head) into the water subphase and their fatty tail away from the water.[56,69,70] Studies covering these monomolecular films at the air-water interface (Langmuir films) at the air-water interface have been carried out through a variety of analytical techniques and on a wide range of amphiphilic and epiphilic (surface loving) molecules.

The packing of amphiphiles at the air-water interface depends on their surface concentration, or surface density (Γ). These systems have been compared to their three-dimensional counterparts in terms of the 'phases' used to describe their packing density, fluidity, etc.[88] When Γ is small, the surface molecules are said to exist in a gaseous state: they are free to move about the surface with relatively little interaction between other surface molecules. Increasing Γ results in more interactions between surface molecules yielding the liquid phase, where movement is possible but impeded. Further increase in Γ results in the formation of the 2D solid state where the molecules are maximally packed and lateral diffusive movement is restricted. These typical 2D phases are pictorially described in Figure 1.5:

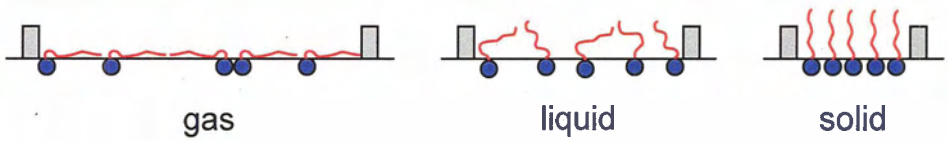

Figure 1.5. Orientation of typical non-aggregating amphiphiles at the air-water interface at various surface densities (Γ).

The polar (sometimes charged) head groups of the amphiphiles disrupt the tight packing of water molecules at the surface, causing a decrease in γ due to the reduction in cohesive energy between water molecules at the surface. By reducing the area available to the surface molecules, their surface density inherently increases, eventually resulting in repulsive interactions between amphiphiles and a further reduction in γ. What is most often measured is the difference between the surface tension of the monolayer-containing

film (γ) from that of the pure air-water interface (γ_0), which is expressed as the surface pressure (π):

$$\pi = \gamma_o - \gamma \qquad \textbf{1.8}$$

Monitoring π as a function of the available area (A) is an extremely useful method that allows one to obtain information pertaining to the conformation and behaviour of the respective parts of the amphiphile under study. When performed at constant temperature, these plots are referred to as $\pi - A$ isotherms. A simplified $\pi - A$ isotherm is provided in Figure 1.6 along with the identification of the various phases described in Figure 1.5.

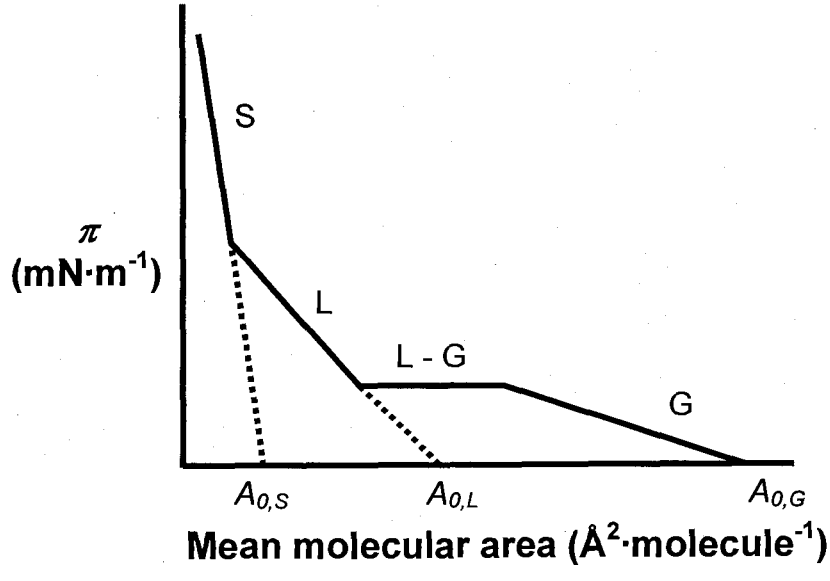

Figure 1.6. Simplified $\pi - A$ isotherm identifying the 2D gas-like phase (G), the 2D liquid phase (L) and the 2D solid (S) phase, and the respective extrapolated limiting mean molecular areas ($A_{0,X}$). The liquid – gas phase transition region (L - G) was identified as the plateau in the isotherm

The abundance of information available from $\pi - A$ isotherms makes an exhaustive description well beyond the scope of this thesis and an interested reader is directed to several good references.[37,38,82,85,86,89] Two important parameters are considered here: the limiting mean molecular area ($A_{0,x}$), and the isothermal compressibility (C_m). A_0 is defined as the area occupied by an average molecule in a given phase, and is obtained by extrapolating a particular linear region of the isotherm to $\pi = 0$. Depending on the tendency of molecules to exhibit more than one phase over the range of A investigated, more than one A_0 may be obtained as shown in Figure 1.6. For example, a typical fatty acid has been shown to exist in three distinct phases on the $\pi - A$ isotherm (gas, liquid and solid) which corresponds to the three distinct molecular conformations described previously in Figure 1.5.[82]

Qualitatively, C_m is a measure of the ease with which a monolayer can be deformed by an applied stress. It too has been compared to its three-dimensional counterpart, where compressibility of a 3D system is a measure of the relative volume (V) change in response to a pressure (P) change at constant temperature, i.e.:

$$C = \frac{-1}{V}\left(\frac{\partial V}{\partial P}\right)_T \qquad \textbf{1.9}$$

It has been shown that the compressibility of a two-dimensional monolayer may be analogously defined as:[84]

$$C_m = \frac{-1}{A}\left(\frac{\partial A}{\partial \pi}\right)_T \qquad \textbf{1.10}$$

where $\left(\frac{\partial A}{\partial \pi}\right)_T$ is the reciprocal of the slope of the isotherm in a given region, and A may also be taken directly from the isotherm; C_m calculated for a monolayer is commonly expressed in units of $m \cdot mN^{-1}$. From Figure 1.5, it is easy to appreciate that it requires less force to bring together the 'floppy' tails of our fatty acid in the gas state, compared to the same molecules in the tightly-packed solid phase. This generally results in larger C_m values for less condensed phases, as suggested by the decrease in slope on moving from the solid to gas regions of Figure 1.6.

The above description of surfactant molecules at the air-water interface was provided as a simple example of the effect of A (or Γ) on π, and how the relationship between these parameters can be measured in the form of $\pi - A$ isotherms, which yield important information on surface structures and phases at the air-water interface. It should be noted that amphiphilic block copolymers behave in an analogous fashion to the surfactant example, complicated however by their increased size and tendency to aggregate. These more complex systems will be the subject of subsequent chapters.

1.5.3. Langmuir-Blodgett Films

Monitoring materials at the air-water interface through $\pi - A$ isotherms has been shown to provide important information on their interfacial behaviour. However, for many investigations and applications, it is advantageous to transfer films formed at the air-water interface to solid substrates for analysis and / or use in functional materials. There are several techniques available to transfer Langmuir monolayers to solid substrates, with the most common being the Blodgett[90] and the Schaefer[91] methods. The

difference between the two is that in the Blodgett, or Langmuir-Blodgett (LB) method, the film is transferred via a vertical dip, whereas for the Schaefer method, the dip is horizontal. Each method has its specific applications, and for the present work, where a relatively hydrophilic substrate (glass) was used, it was advantageous to employ the LB technique; this approach took advantage of favourable interactions between the hydrophilic groups of the block copolymer amphiphile and the glass, leading to good adhesion between the LB film and the substrate. A schematic representation of a typical LB transfer of a Langmuir monolayer is provided as Figure 1.7, where the solid substrate (light blue) is initially submerged and then slowly raised through the interface containing the Langmuir film. The moveable paddles are electronically controlled through a feedback loop to maintain the desired π as material is transferred from the interface, thus promoting a homogeneous transfer event. It should be noted that multiple dip cycles are possible where the substrate is raised and lowered through the interface, as desired. The film transfer is quantified by a characteristic transfer ratio (*TR*) which is a measure of the efficiency of the transfer event, and calculated through:

$$TR = \frac{\Delta A_T}{A_S} \qquad \textbf{1.11}$$

where ΔA_T is the change in trough area during transfer (i.e. change in area to maintain a constant π), and A_S is the total surface area of the substrate raised or lowered through the interface. Transfer ratios are optimized at 1.0, however many factors can cause deviations from this value.[87]

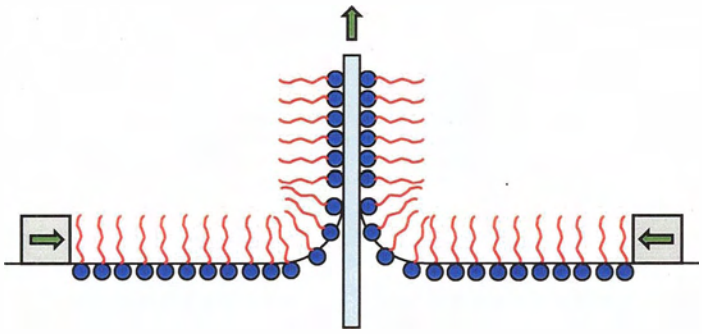

Figure 1.7. Vertical transfer of a Langmuir film at the air-water interface via the Langmuir-Blodgett method

1.6. Characterization Techniques

To accurately interpret the results presented in the thesis, it was absolutely essential that the fundamental building blocks, along with the final structures, were well characterized. For small molecule chemistry, this process is often taken for granted, as conventional spectroscopic techniques (NMR and FTIR for example) are often sufficient to elucidate the chemical structure of the materials involved. However, polymers, diblock copolymer micelles, and supermicellar aggregates, all exhibit colloidal behaviour and structural characteristics that cannot be probed by NMR and FTIR. To obtain information on the molecular weight distributions, structure, and interparticle interactions for the complex colloidal systems that were the building blocks for this work, gel permeation chromatography (GPC) and light scattering (LS) methods were employed, as described below. The final self-assembled structures, transferred from the air-water interface to solid substrates, were characterized using a combination of atomic force microscopy (AFM) and transmission electron microscopy (TEM), and these methods are described in the following sections.

1.6.1. Laser Light Scattering

Light scattering (LS) is by far the most popular method for the determination of M_w for polymers and colloidal particles in solution. When particles are small with respect to the wavelength of light, incident radiation that strikes the particle displaces the electrons causing them to oscillate about their equilibrium position at the same frequency as the incident radiation, inducing a transient dipole in the particle.[46] The result of this process is the creation of a secondary scattering centre (the particle) which re-emits radiation of the same frequency as the incident light in all directions. This 'scattering' process may be observed (through sensitive detectors) over a multitude of time scales.

When data acquisition is on the order of seconds, an average scattering intensity is collected, which is the basis behind static light scattering (SLS). SLS studies are generally used to obtain: 1) the weight-average molecular weight (M_w), 2) the radius of gyration (R_g), which is a measure of the average distance between the centre of gravity of the particle and to the chain end, and 3) the second virial coefficient (A_2), which is a thermodynamic term describing the extent of attractive or repulsive interactions in the polymer / solvent system.

Dynamic light scattering (DLS) experiments allow detection of fast fluctuations in the scattered light intensity caused by solution density fluctuations. These fluctuations are due to Brownian motion of particles in solution, and can be analyzed to yield the diffusion coefficient D_0 of the particles. The diffusion coefficient can then be used to calculate the hydrodynamic radius (R_h), which is a measure of particle size in solution including any solvent molecules that move with the particle. Further details on both SLS and DLS measurements and data analysis are described in Chapter 4.

1.6.2. Gel Permeation Chromatography

GPC is a powerful and versatile analytical tool that provides invaluable information pertaining to polymer performance. It is the only proven technique for characterizing the complete size distribution of a polymer. A schematic representation of the salient components involved in GPC is outlined in Figure 1.8. As shown in the figure, an appropriate solvent is continuously pumped through the system at a rate chosen by the user, and the sample is injected into the solvent stream. The sample is carried through at least one column, which separates the molecules on the basis of relative molecular weight. The efficiency of the column is dependant on the use of mechanically stable, highly cross-linked polymer gels with a distribution of pore sizes, which by means of a sieving action separate the polymer sample into fractions based on the hydrodynamic size of particles.[46] This separation process is outlined in the magnified cross section of a hypothetical column which shows that the larger polymer molecules (green) spend relatively little time in the pores of the gel and spend the majority of their time in the larger spaces between the gel particles. The smaller molecules (red), on the other hand, are able to penetrate the pores of the gel, which increases their pathlength in the column, resulting in a longer elution time. The result of this process is that polymers of higher molecular weight in the distribution (larger particles) elute first, followed by particles of decreasing molecular weight (smaller particles), all other parameters being equal. Following fractionation, the eluent is passed through a series of detectors which are sensitive to various aspects of the polymer fractions, including refractive index (RI), UV / vis, viscosity, and right-angle and low-angle light scattering (RALS, LALS). We note that the use of a light scattering detector allows the weight-average molecular weight of

the fractionated sample to be determined directly from the combined LALS and RI detector signals, without the need of calibration standards of known molecular weights.

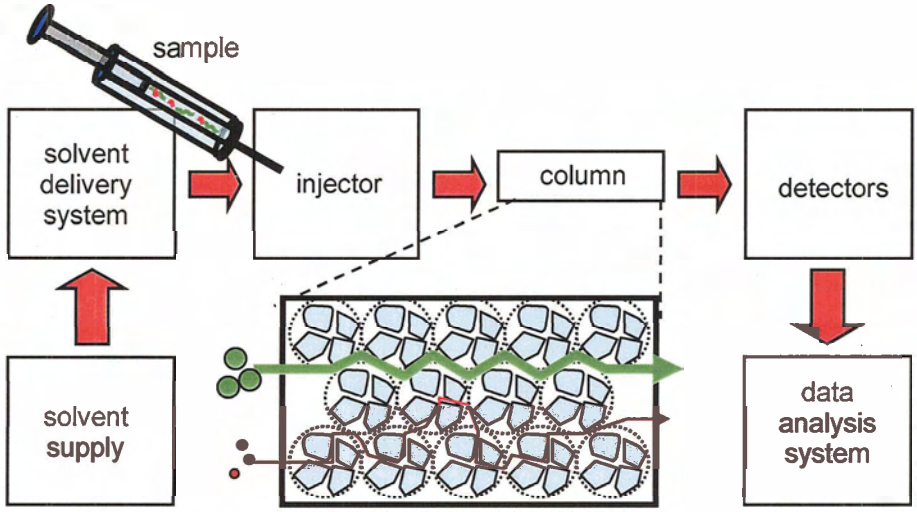

Figure 1.8. Experimental setup of Gel Permeation Chromatography (GPC). The magnified cross-section of the column highlights paths taken from two different sized molecules. The larger molecules (green) traveling around the porous silica beads (blue), whereas the smaller molecules (red) fit into the pores.

1.6.3. Microscopies

As a major focus of the present investigation was the spontaneous creation of low-dimensional surface features, it was necessary to employ techniques that provided a discernable means to characterize the final structures. The various polymer and NP / polymer features produced in our work exhibited organization on combination of length scales, ranging from nanometers to micrometers, such that a combination of microscopy techniques was required. To this end, we employed atomic force microscopy (AFM) to gain insight into the mesoscopic topology of the surface features, and transmission electron microscopy (TEM) to study their nanoscopic internal structure.

1.6.3.1. Atomic Force Microscopy

AFM is a subset of the scanning probe microscope (SPM) and relies on the use of a mechanical probe for the generation of images. AFM was the method of choice for this work, as it allows for the imaging of non-conductive samples (eg. polymers). AFM data acquisition may be completed in two primary scanning modes: contact mode and dynamic mode. In dynamic mode, the tip oscillates above the surface; as the tip nears the surface, attractive forces between the tip and the sample will change the oscillation amplitude of the probe tip.[93] Contact mode, on the other hand, may be described as a 'molecular record player': the force between the surface and tip is held constant such that features on the surface cause the tip to deflect, following the contours of the contact line and producing a topological map of the surface. The present investigation used contact mode exclusively, so the remainder of the discussion focuses on this technique; however,

the general features of the experimental setup are applicable to both methods. A simplified picture of the AFM is provided in Figure 1.9.

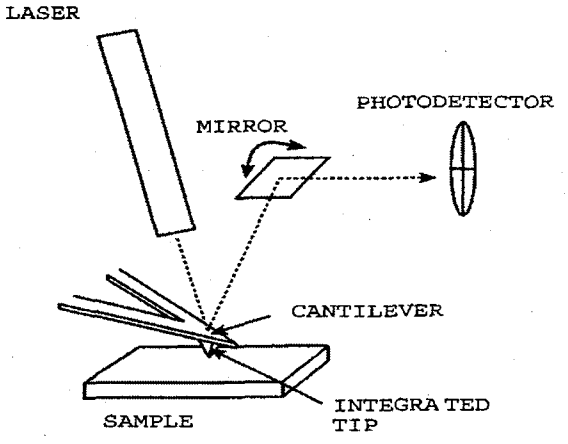

Figure 1.9. Schematic representation of the Atomic Force Microscope (AFM)[94]

In contact mode AFM, a laser light source is focused on the back of a mirrored cantilever supporting a sharp tip on the opposing side. The laser is reflected off of the cantilever and onto a four-quadrant photodetector via a second mirror. As the tip moves up and down across the surface of a rough sample the reflected beam strikes various regions of the photodetector which is correlated with the height (z) of the image at a particular (x, y) coordinate. The movement of the cantilever / tip must be very precise to ensure image quality and therefore advanced materials capable of fine movement must be employed. This movement is controlled via a piezoelectric ceramic which has the convenient function that a change in the electric potential across the material results in a corresponding change in the physical dimensions. A constant challenge with vibration-sensitive techniques like AFM is isolation from potential vibration sources. Considering

this, AFM measurements are typically performed on a vibration isolation platform, with the instrument being contained within a dampening shield to minimize air currents and sound waves.

1.6.3.2. Transmission Electron Microscopy

A limitation of conventional AFM is that it only provides a topographical contour map of the surface, such that internal structure cannot be detected by this method. An important result of the present study was the organization of CdS NPs inside a polymeric feature. We therefore required a microscopy technique that permitted the location of these "internal" NPs to be determined. To this end, we employed transmission electron microscopy (TEM), which is sensitive to a material's transparency to a focused electron beam.

Electron microscopy occupies a fundamental niche in science. Before its theoretical design in 1924, and development in the 1930's, imaging was reliant on light microscopy. Due to the diffraction limit, a typical light microscope has a spatial resolution on the order of the wavelength used.[94] For example, optical microscopy with green light would allow a resolution ~500 nm, which is two orders of magnitude larger than the smallest features (the CdS NPs) in our materials. X-rays may seem the obvious answer to this issue as they have significantly shorter wavelengths than visible light; however, x-rays are not easily refracted from a surface and therefore the resultant image quality is poor.[94] As the electron is a charged particle, it is easily refracted by a magnetic field and scattered by regions of high electron density. Additionally, it can be accelerated when subjected to an electrical potential. The stronger the accelerating potential, the

faster the electrons travels and the shorter its wavelength in accordance with the de Broglie relationship:[95]

$$\lambda = \frac{h}{mv} \qquad \textbf{1.12}$$

where λ is the wavelength of an electron of mass m traveling at a velocity v, and h refers to Planck's constant. All TEM imaging completed in this thesis was performed at an accelerating voltage of 75 kV, which would result in a theoretical resolution of ~5 pm. While this resolution would very much please Feyman,[96] it is orders of magnitude beyond the current state-of-the-art, and certainly beyond the technology available for this work. We employed a Hitachi H-700 electron microscope, with a spatial resolution of ~1 nm.[97] Figure 1.10 is a schematic representation of a typical TEM. The electron gun fires a monochromatic stream of electrons which are focused to a thin, coherent beam through a series of condenser lenses (only one lens is shown). This thin beam then strikes the specimen and the electrons are either[95] a) transmitted through the specimen without any significant interaction with the specimen, b) elastically scattered whereby the electrons are deflected by a region of the specimen without a loss of energy, or c) inelastically scattered where the electrons lose energy when they interact with the specimen. These various processes result in a distribution of electrons that may or may not pass through the objective aperture. Regions of the specimen that consist of relatively light atoms result in more transmitted than scattered electrons, and appear as light regions after being focused through a series of lenses onto a fluorescent screen or photographic plate. The

opposite is true for heavy atoms or molecules (e.g. CdS NPs), which scatter a relatively large number of electrons and appear as dark regions in the image.

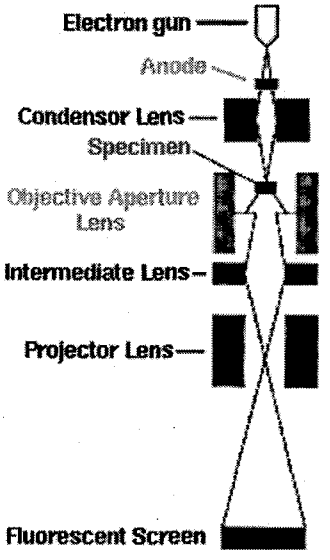

Figure 1.10. Schematic representation of a transmission electron microscope (TEM)[96]

1.7. Content of the Thesis

The body of this thesis consists of three chapters, each building on the previous chapter and leading ultimately to the directed assembly of polymer-stabilized CdS NPs at the air-water interface The content of these three chapters is as follows:

Chapter 2 focuses exclusively on the behaviour and surface morphologies of a single PS-*b*-PEO (11.4 wt%-PEO) diblock copolymer at the air-water interface as a function of spreading solution concentration. The interfacial behaviour of the Langmuir films is examined through the $\pi - A$ isotherms, and the influence of spreading solution concentration on the limiting mean molecular area and monolayer compressibility are

examined. Surface morphologies are then studied by AFM of LB films transferred from the air-water interface, and analyzed in the context of the $\pi - A$ isothermal data.

Chapter 3 is an extension of Chapter 2 with a more hydrophilic PS-*b*-PEO (18.9wt%-PEO) copolymer being included in the investigation. This more hydrophilic PS-*b*-PEO copolymer permits independent study of the PEO pancake phase, which is not exhibited in the isotherm data of PS-*b*-PEO (11.4wt%-PEO). Additionally, hysteresis effects resulting from multiple compression / expansion isotherms are studied for both copolymers as a function of spreading solution concentration. This combination of data provides a consistent picture of the surface structure of PS-*b*-PEO aggregates for different spreading concentrations, and a new simple model is presented. This chapter also presents for the first time fascinating microscopy evidence of the role of polymer solution dewetting from the air-water interface in the development of various 2D PS-*b*-PEO surface features—challenging the notion that these block copolymer surface aggregates are simply 2D analogues of the various thermodynamic block copolymer micelle morphologies found in 3D solutions.

Chapter 4 describes a new and versatile method of patterning polymer-stabilized CdS NPs into low-dimensional hybrid surface features through a nonlithographic self-assembly mechanism. Polymer-stabilized CdS NPs (PS-CdS) are blended with PS-*b*-PEO diblock copolymers (11.4wt% and 18.9wt%-PEO) and deposited from chloroform solutions at the air-water interface. The concentration of the spreading solution and weight fraction of PS-CdS in the blends is varied in an effort to tune the hierarchical surface morphologies. AFM is employed to probe the mesoscopic topological structure and TEM is applied to discern the nanoscopic organization of CdS NPs within the

polymer matrix. The surface behaviour of the various blends is also considered in a detailed $\pi - A$ isothermal investigation.

The thesis concludes in Chapter 5 with a summary of the salient and novel findings over the course of this work. Suggestions are also made for future investigations, concerning both interfacial amphiphilic diblock copolymer self-assembly and its role in the self-assembly of inorganic nanoparticles.

1.8. References

(1) Henglein, A. *Chem. Rev.* **1989,** *89*, 1861.

(2) Steigerwald, M. L.; Brus, L. E. *Acc. Chem. Res.* **1990,** *23*, 183.

(3) Weller, H. *Angew. Chem., Int. Ed. Engl.* **1993,** *32*, 41.

(4) Alivisatos, A. P. *Science* **1996,** *271*, 933.

(5) Collier, C. P.; Vossmeyer, T.; Heath, J. R. *Annu. Rev. Phys. Chem.* **1998,** *49*, 371.

(6) Murray, C. B.; Kagan, C. R.; Bawendi, M. G. *Annu. Rev. Mater. Sci.* **2000,** *30*, 545.

(7) El-Sayed, M. A. *Acc. Chem. Res.* **2001,** *34*, 257.

(8) Sapra, S.; Nanda, J.; Sarma, D. D. *In Proc. of the Plenary 90th Session of Indian Science Congress: Bangalore* **2003**, 3.4.

(9) Wang, C.-W.; Moffitt, M. G. *Langmuir* **2004,** *20*, 11784.

(10) Wang, C.-W. *M.Sc. thesis* (University of Victoria) **2005**.

(11) Shenhar, R.; Norsten, T. B.; Rotello, V. M. *Adv. Mater.* **2005,** *17*, 657.

(12) Trindade, T.; O'Brien, P.; Pickett, N. L. *Chem. Mater.* **2001,** *13*, 3843.

(13) Shipway, A. N.; Katz, E.; Willner, I. *ChemPhysChem* **2000,** *1*, 18.

(14) Daniel, M.-C.; Astruc, D. *Chem. Rev.* **2004,** *104*, 293.

(15) Kim, S.; Bawendi, M. G. *J. Am. Chem. Soc.* **2003,** *125*, 14652.

(16) Moffitt, M.; Vali, H.; Eisenberg, A. *Chem. Mater.* **1998,** *10*, 1021.

(17) Ozin, G. A. *Adv. Mater.* **1992,** *4*, 612.

(18) Kramer, S.; Fuierer, R. R.; Gorman, C. B. *Chem. Rev.* **2003,** *103*, 4367.

(19) Eigler, D. M.; Schweizer, E. K. *Nature* **1990,** *344*, 524.

(20) Vettiger, P.; Cross, G.; Despont, M.; Drechsler, U.; Durig, U.; Gotsmann, B.; Haberle, W.; Lantz, M. A.; Rothuizen, H. E.; Stutz, R.; Binnig, G. K. *IEEE T. Nanotechnol.* **2002,** *1*, 39.

(21) Vukusic, P.; Sambles, J. R. *Nature* **2003,** *424*, 852.

(22) Zhu, J.; Eisenberg, A.; Lennox, R. B. *J. Am. Chem. Soc.* **1991,** *113*, 5583.

(23) Zhu, J.; Eisenberg, A.; Lennox, R. B. *Langmuir* **1991,** *7*, 1579.

(24) Zhu, J.; Eisenberg, A.; Lennox, R. B. *Die Makromol. Chem., Macromol. Symp.* **1992,** *53*, 211.

(25) Zhu, J.; Eisenberg, A.; Lennox, R. B. *J. Phys. Chem.* **1992,** *96*, 4727.

(26) Zhu, J.; Eisenberg, A.; Lennox, R. B. *Macromolecules* **1992,** *25*, 6547.

(27) Li, S.; Hanley, S.; Khan, I.; Varshney, S. K.; Eisenberg, A.; Lennox, R. B. *Langmuir* **1993,** *9*, 2243.

(28) Meszaros, M.; Eisenberg, A.; Lennox, R. B. *Faraday Discuss.* **1994,** *98*, 283.

(29) Li, Z.; Zhao, W.; Quinn, J.; Rafailovich, M. H.; Sokolov, J.; Lennox, R. B.; Eisenberg, A.; Wu, X. Z.; Kim, M. W.; Sinha, S. K.; Tolan, M. *Langmuir* **1995,** *11*, 4785.

(30) Li, S.; Clarke, C. J.; Lennox, R. B.; Eisenberg, A. *Colloid Surface, A.* **1998,** *133*, 191.

(31) Cox, J.; Eisenberg, A.; Lennox, R. B. *Curr. Opin. Col. Int. Sci.* **1999,** *4*, 52.

(32) Li, S.; Clarke, C. J.; Eisenberg, A.; Lennox, R. B. *Thin Solid Films* **1999,** *354*, 136.

(33) Gragson, D. E.; Jensen, J. M.; Baker, S. M. *Langmuir* **1999,** *15*, 6127.

(34) Dewhurst, P. F.; Lovell, M. R.; Jones, J. L.; Richards, R. W.; Webster, J. R. P. *Macromolecules* **1998,** *31*, 7851.

(35) Goncalves da Silva, A. M.; Filipe, E. J. M.; d'Oliveira, J. M. R.; Martinho, J. M. G. *Langmuir* **1996,** *12*, 6547.

(36) Goncalves da Silva, A. M.; Simoes Gamboa, A. L.; Martinho, J. M. G. *Langmuir* **1998,** *14*, 5327.

(37) Faure, M. C.; Bassereau, P.; Carignano, M.; Szleifer, I.; Gallot, Y.; Andelman, D. *Eur. Phys. J. B.* **1998,** *3*, 365.

(38) Faure, M. C.; Bassereau, P.; Lee, L. T.; Menelle, A.; Lheveder, C. *Macromolecules* **1999,** *32*, 8538.

(39) Cox, J. K.; Yu, K.; Eisenberg, A.; Lennox, R. B. *Phys. Chem. Chem. Phys.* **1999,** *1*, 4417.

(40) Cox, J. K.; Yu, K.; Constantine, B.; Eisenberg, A.; Lennox, R. B. *Langmuir* **1999,** *15*, 7714.

(41) Baker, S. M.; Leach, K. A.; Devereaux, C. E.; Gragson, D. E. *Macromolecules* **2000,** *33*, 5432.

(42) Devereaux, C. A.; Baker, S. M. *Macromolecules* **2002,** *35*, 1921.

(43) Barentin, C.; Muller, P.; Joanny, J. F. *Macromolecules* **1998,** *31*, 2198.

(44) Cheyne, R. B.; Moffitt, M. M. *Langmuir* **2005,** *21*, 5453.

(45) Staudinger, H. *The Nobel Prize in Chemistry* **1953**.

(46) Cowie, J. M. G., *Polymers: Chemistry and Physics of Modern Materials*. 2nd Edition, Nelson Thornes, 1991

(47) Bandrup, J.; Immergut, E. H.; Grulke, E. A. (Eds), *Polymer Handbook* 4th edition, John Wiley & Sons, Inc., New York, 1999

(48) Riess, G. *Prog. Polym. Sci.* **2003,** *28*, 1107.

(49) Morton, M., *Anionic Polymerization: Principles and Practice*, Academic Press, 1983

(50) Szwarc, M., *Carbanions, Living Polymers and Electron Transfer Processes.*, Interscience Publishers, 1968

(51) Hautekeer, J.-P.; Varshney, S. K.; Fayt, R.; Jacobs, C.; Jerome, R.; Teyssie, P. *Macromolecules* **1990,** *23*, 3893.

(52) Zhong, X. F.; Varshney, S. K.; Eisenberg, A. *Macromolecules* **1992,** *25*, 7160.

(53) Gao, Z.; Zhong, X.-F.; Eisenberg, A. *Macromolecules* **1994,** *27*, 794.

(54) Bodor, G., *Structural Investigation of Polymers.*, Ellis Horwood Ltd., 1991

(55) Manson, J. A.; Sperling, L. H., *Polymer Blends and Composites.*, Plenum Press, 1976

(56) Myers, D., *Surfactant Science and Technology.*, John Wiley & Sons Inc., 1988

(57) Holmberg, K.; Jonsson, B.; Kronberg, B.; Lindman, B., *Surfactants and Polymers in Aqueous Solution,* 2nd Ed., John Wiley & Sons, Ltd., 2003

(58) Malmsten, M., *Surfactants and Polymers in Drug Delivery. Drugs and the Pharmaceutical Sciences. Volume 122.*, Marcel Dekker, Inc., 2002

(59) Raviv, U.; Giasson, S.; Kampf, N.; Gohy, J.-F.; Jerome, R.; Klein, J. *Nature* **2003,** *425*, 163.

(60) Brown, H. R. *IBM J. Res. Develop* **1994,** *38*, 379.

(61) Green, P. F.; Limary, R. *Adv. Colloid Interface Sci* **2001,** *94*, 53.

(62) Moffitt, M.; Eisenberg, A. *Macromolecules* **1997,** *30*, 4363.

(63) Moffitt, M., Ph.D, thesis (McGill University) **1997**.

(64) Xia, Y.; Rogers, J. A.; Paul, K. E.; Whitesides, G. M. *Chem. Rev.* **1999,** *99*, 1823.

(65) Spatz, J. P. E., P.; Mossmer, S.; Moller, M.; Kramarenko, E. Yu.; Khalatur, P. G.; Potemkin, I. I.; Khokhlov, A. R.; Winkler, R. G.; Reineker, P. *Macromolecules* **2000,** *33*, 150.

(66) Zhang, L.; Eisenberg, A. *Science* **1995,** *268*, 1728.

(67) Whitesides, G. M.; Grzybowski, B. *Science* **2002,** *295*, 2418.

(68) Israelachvili, J., *Intermolecular and Surface Forces,* 2nd Ed., Academic Press Ltd., 1992

(69) Gelbart, W. M.; Ben-Shaul, A.; Roux, D., *Micelles, Membranes Microemulsions and Monolayers.*, Springer-Verlag, Inc., 1994

(70) Jones, M. N.; Chapman, D., *Micelles, Monolayers and Biomembranes.*, John Wiley & Sons, Inc., 1995

(71) Woggon, U., *Optical Properties of Semiconductor Quantum Dots.*, Springer, 1997

(72) BruchezJr, M.; Moronne, M.; Gin, P.; Weiss, S.; Alivisatos, A. P. *Science* **1998,** *281*, 2013.

(73) Tessler, N.; Medvedev, V.; Kazes, M.; Kan, S. H.; Banin, U. *Science* **2002,** *295*, 1506.

(74) Coe, S.; Woo, W.-K.; Bawendi, M.; Bulovic, V. *Nature* **2002,** *420*, 800.

(75) Goldstein, A. N.; Echer, C. M.; Alivisatos, A. P. *Science* **1992,** *256*, 1425.

(76) Dannhauser, T.; O'Neil, M.; Johansson, K.; Whitten, D.; McLendon, G. *J. Phys. Chem.* **1986,** *90*, 6074.

(77) Herron, N.; Wang, Y.; Eckert, H. *J. Am. Chem. Soc.* **1990,** *112*, 1322.

(78) Murray, C. B.; Norris, D. J.; Bawendi, M. G. *J. Am. Chem. Soc.* **1993,** *115*, 8706.

(79) Ni, T.; Nagesha, D. K.; Robles, J.; Materer, N. F.; Mussig, S.; Kotov, N. A. *J. Am. Chem. Soc.* **2002,** *124*, 3980.

(80) Brus, L. *J. Phys. Chem.* **1986,** *90*, 2555.

(81) McMurry, J.; Fay, R. C., *Chemistry,* 2nd ed., Prentice Hall, 1998

(82) Hiemenz, P. C., *Principles of Colloid and Surface Chemistry.*, Marcel Dekker Inc., 1977

(83) van Olphen, H.; Mysels, K. J., *Physical Chemistry: Enriching Topics From Colloid and Surface Science*, Theorex, 1975

(84) MacRitchie, F., *Chemistry at Interfaces.*, Academic Press Inc., 1990

(85) Gaines, G. L., *Insoluble Monolayers at Liquid-Gas Interfaces.*, Wiley and Interscience Publishers, 1966

(86) Ulman, A., *An Introdiction to Ultrathin Organic Films: From Langmuir-Blodgett to Self-Assembly.*, Academic Press, 1991

(87) *KSV 3000 Instruction Manual*, KSV Instruments Ltd., 2001. p. 58

(88) Harkins, W. D., *The Physical Chemistry of Surface Films.*, Reinhold, 1952

(89) des Cloizeaux, J. *J. Phys. (Paris)* **1975,** *36*, 281.

(90) Blodgett, K. A.; Langmuir, I. *Phys. Rev.* **1937,** *51*, 964.

(91) Langmuir, I.; V.J., S. *J. Am. Chem. Soc.* **1938,** *60*, 1351.

(92) *KSV 3000 Instruction Manual*, KSV Instruments Ltd., 2001

(93) Marek, T., *ThermoMicroscopes Explorer Instrument Operation Manual.*, 2001

(94) Pennycook, S. J.; Lupini, A. R.; Varela, M.; Borisevich, A.; Peng, Y.; Nellist, P. D., *Quantum Mechanical Resolution Limits to Imaging and Spectroscopy in the Transmission Electron Microscope.*, Old Dominion University, 2003, p. 126.

(95) Agar, A. W.; Alderson, R. H.; Chescoe, D., *Principles and Practice of Electron Microscope Operation.*, North Holland Publishing Co., 1974

(96) Feyman, R. P. *Engineering and Science* **1960,** February 22.

(97) Gowen, B., Personal Communication. December, 2004.

Chapter 2

Novel Two Dimensional "Ring and Chain" Morphologies in Langmuir-Blodgett Monolayers of PS-b-PEO Block Copolymers: Effect of Spreading Solution Concentration on Self-Assembly at the Air-Water Interface

2.1. Introduction

The process of self-assembly; the autonomous organization of components into patterns or structures,[1] offers many advantages to conventional lithographic, or 'top down' methods for the formation of functional structures. Even with recent advances in materials science and chemical engineering,[2] large-scale arrays of features below ca. 100 nm have yet to be efficiently achieved solely through lithographic techniques. Nanostructures in two and three dimensions are easily and efficiently produced through self-assembly, and for that reason, much effort has been directed to understanding its fundamentals and many intricacies.

Structural control via self-assembly is dependent on design at the molecular level since a combination of environmental and molecular factors dictate kinetic and thermodynamic aspects of self-assembly. Amphiphilic diblock copolymers are an interesting and important class of molecules that have been shown to self-assemble into well-defined nanoscale structures over many length scales, and there exist many examples of these macromolecules forming low-dimensional features[3-22] (whereby at least one dimension is on the order of nanometers) and three dimensional features.[23-37]

In recent years, extensive work has been carried out on the self-assembly at the air-water interface of diblock copolymers based on a hydrophobic polystyrene (PS) block and a hydrophilic poly(ethylene oxide) (PEO) block.[13-21] The surface-active nature of PEO promotes its spontaneous adsorption at the air-water interface,[18,38-42] although above a critical two-dimensional (2D) overlap density, the solubility of PEO causes it to become easily detached from the interface and dissolved in the aqueous subphase. To combat this

effect, the hydrophobic PS block is required to tether the PEO blocks to the surface above the critical surface density.

The properties of PS-*b*-PEO monolayers have been widely studied using Langmuir isotherms.[13-21,43-48] The Langmuir film produced by spreading PS-*b*-PEO at the air-water interface can be regulated by compression or expansion of the monolayer via moveable paddles which can either increase or decrease the area (A) available to the molecules, effecting changes in surface tension (γ) as a function of the surface coverage (Γ). The change in γ is reported as surface pressure ($\pi = \gamma_0 - \gamma$) as defined in Chapter 1. When the relative surface area of the PS buoy blocks is small compared with the spread PEO blocks, compression of the monolayer films above a critical PEO density results in an increase in π with decreasing A followed by a plateau region (constant π) in the π - A plot, indicating a first-order phase transition. This plateau has been attributed to a "pancake-to-brush" transition as tethered PEO chains submerge into solution,[16,17,42-46] although an alternative view suggests that the observed phase transition is related to a conformational change in PEO at the water surface.[14,38]

Irrespective of the nature of the PEO phase transition, there is strong evidence that this transition can be hindered when the area occupied by the PS anchoring blocks becomes comparable to the predicted pancake area of the PEO blocks due to steric interactions between PS surface domains upon compression[20,21] and repulsive interactions between PS and PEO at the interface.[18-21] The projected area of insoluble PS blocks at the water surface has been estimated from Langmuir isotherm studies of Kumaki,[49,50] who studied dilute solutions of PS homopolymer deposited onto the air-water interface and found a linear relation between molecular weight, M, and the limiting areas of PS

globules: $A_{0,PS} = 0.04M$ Å^2/molecule.[50] As suggested by Baker et al.,[20,21] the predicted pancake areas for the PEO blocks can be calculated on the basis of the work of Goncalves da Silva et al., who studied Langmuir isotherms for PS-*b*-PEO diblocks of varying PEO block lengths and relatively small PS anchoring blocks and determined a limiting area per adsorbed PEO monomer of 27-31 Å^2;[17,43] these values suggest that tethered PEO blocks are more compact at the air-water interface than PEO homopolymer, which has shown to occupy an area of ~ 28 - 40 Å^2 per EO monomer.[38,51]

In a series of recent studies, Baker and co-workers have studied Langmuir isotherms and surface morphologies for monolayers of various PS-*b*-PEO diblocks of high molecular weight (> 50 k), covering the composition regime where the PS blocks begin to impede the PEO phase transition.[20,21] For a copolymer with 15.5 wt% PEO (ratio of PEO / PS limiting area ~ 3:1), only a small "pseudoplateau" was observed in the compression isotherm, although the limiting pancake area did not appear to be influenced by PS, with a value of 30 Å^2 per PEO monomer,[20] in good agreement with results obtained for PS-*b*-PEO with small PS blocks.[17,43] However, when the relative contribution of PS was increased further, with a copolymer of 7 wt% PEO (ratio of PEO/PS limiting area ~ 1:1), no plateau was observed in the isotherm and the limiting area was < 20 Å^2 per PEO monomer, [21] significantly below the predicted value and suggesting that PEO monomers become desorbed due to the repulsive effect of PS domains at the interface.[20,21] The absence of a plateau in compression isotherms of PS-*b*-PEO diblocks with relatively long PS blocks has also been demonstrated by Cox et al.[14,15]

A strong effect of relative PS block lengths on PS-*b*-PEO surface morphologies has also been demonstrated by Devereaux and Baker, who carried out atomic force

microscopy (AFM) of Langmuir-Blodgett (LB) films transferred from the air-water interface.[20,21] They found that circular and uniform nanoscale aggregates of PS blocks (dots) formed from diblocks with PEO contents of 15.5 wt% and higher, while for the 7 wt% PEO sample, the kinetic restrictions of PS chain entanglement competed with surface spreading to give a mixture of dots, spaghetti, and large planer aggregates, termed continents, as observed previously by Cox et al.[15] Devereaux et al. also found that the predominance of certain morphologies was affected by the concentration of the spreading solution, with dots favoured at lower concentrations and the larger continent structures favoured at higher concentrations, suggesting that more extensive PS entanglement at higher deposition concentrations leads to larger surface aggregates.[21]

In this chapter, we investigate the properties of a new high-molecular-weight (141k) PS-*b*-PEO diblock copolymer with PEO content of 11.4 wt% deposited at the air-water interface. The effect of spreading solution concentration on surface morphologies of LB films is studied for this copolymer, which has a predicted ratio of PEO / PS limiting area of ~ 2:1. The present diblock therefore falls between the two compositions recently studied by Baker and co-workers[20,21] and shows a number of intriguing effects that have not been reported for these other systems. In agreement with Devereaux et al.,[21] we find that the morphology of surface aggregates depends on the concentration of the spreading solution; however, in the present system, no continent structures are observed over the investigated concentration range (0.10 - 2.0 mg/mL), with dots and spaghetti structures being predominant for spreading concentrations $\geq$ 0.50 mg/mL. Interestingly, two novel 2D aggregate morphologies, rings and chains, become prominent features for spreading concentrations $\leq$ 0.25 mg/mL.

Despite the apparent influence of spreading solution concentration on the surface morphologies of PS-*b*-PEO aggregates, a detailed investigation into the $\pi - A$ isotherms as a function of concentration has not been considered. Considering this, we further the findings of Devereaux et al.,[21] and provide the first observation of an effect of spreading concentration on compression isotherms. The isotherms reveal a constant limiting mean molecular areas for higher spreading concentrations that are close to the calculated PS limiting area, while for lower spreading concentrations, corresponding to the appearance of rings and chains, an increase in the limiting mean molecular area is observed. The correspondence of rings and chains with an increase in the limiting mean molecular area below a critical concentration of spreading solution suggests that the formation of these structures is driven by improved spreading of PEO at the air-water interface, facilitated by a decrease in PS chain entanglement.

2.2. Experimental Section

2.2.1. Materials

The MW = 141k, 11.4 wt% PEO copolymer, PS(1200)-*b*-PEO(366) (M_w/M_n = 1.04) where the numbers in parentheses indicate number-average degrees of polymerization of each block (Polymer Source, Inc., sample no. P119-SEO). A ~ 5 mg/mL stock solution was prepared by weighing an appropriate amount of PS-*b*-PEO (dried overnight in a dark dessicator) accurate to 0.1 mg (Sartorius analytical balance, CP224S) and gravitometrically diluting with glass-distilled, HPLC-grade chloroform (Sigma-Aldrich, 99.9+%) in new glassware that had been cleaned three times with acetone and three times with spectroscopic-grade chloroform (Aldrich, 99.8%).

Spreading solutions of various concentrations were prepared by dilution from this stock solution; solutions were prepared 24 h prior to use to allow for equilibration and used within 2 days for isotherm trials and within 7 days for dipping studies. Prepared solutions were sealed with Teflon and refrigerated in the dark. Solid PS-*b*-PEO was stored in a sealed vial covered in aluminum foil at -20 °C. These precautions were necessary to minimize the degradation of the PEO block via oxidation.[52] A comparison of the 250 MHz ^{1}H NMR spectra from the supplier and after completion of this study confirmed that no PEO degradation occurred in the solid polymer sample.

2.2.2. Dynamic Light Scattering

Dynamic light scattering (DLS) experiments were carried out on a Brookhaven Instruments photon correlation spectrometer equipped with a BI-200SM goniometer, a BI-9000AT digital autocorrelator, and a Melles Griot He-Ne Laser (632.8 nm) with maximum power output of 75 mW. As all light scattering techniques are ultrasensitive to dust impurities, great care was taken to eliminate contamination by dust. A 5 mg/mL solution was filtered through two 0.45 μm pore diameter Teflon filters (Target) into a new scintillation vial (Brookhaven, 12mL) that was cleaned three times with acetone, and vortexed (VWR Scientific, MV1) three times with spectroscopic grade chloroform (Sigma-Aldrich, 99.9+%). Spectroscopic grade chloroform was added to this vial through two 0.20 μm pore diameter Teflon filters (Target) to a final concentration of 2.0mg/mL for analysis. Five replicate measurements of the autocorrelation function were obtained at 90° obtained in a refractive index matching solvent (decalyn) regulated (Polyscience) at 23 °C.

2.2.3. Surface Pressure – Area Isotherms

Surface pressure-area (π- A) isotherms were obtained using a KSV 3000 Langmuir trough (KSV Instruments Ltd.) secured inside a dust shield. The total trough surface area was 150 × 515 mm^2 and total trough volume was ~1 L. The trough area was robotically controlled by two hydrophobic paddles which compressed the spread film symmetrically and bilaterally at a rate of 10 mm/min. House-distilled, deionized water (Barnstead NANOpure Diamond, 18.2 mΩ·cm) was used as the subphase in all trials. Prior to each trial, the water surface was cleaned by aspirating off any debris such that the surface pressure remained < 0.20 mN/m over a full compression. The LB components were cleaned daily with absolute ethanol before replacing the deionized water subphase. Surface pressure measurements were made from a roughened platinum Wilhemly plate (perimeter of 39.240 mm) which was flamed prior to each trial to ensure cleanliness. PS-*b*-PEO solutions in chloroform were spread on the subphase from a gastight Hamilton syringe. Spreading solution volumes depended on the concentration of the spreading solution and ranged from 10 to 1000 μL, so that a constant mass of copolymer was deposited for each trial unless otherwise stated. The spreading solution was deposited dropwise (~2 μL drop volume) at regularly spaced locations on the trough. In all trials, a 15 min evaporation period between the last deposited drop of solution and the beginning of compression ensured complete solvent evaporation.

One aspect of the present isotherm investigations is that the volume of solution deposited must proportionately increase with decreasing concentration to maintain a constant mass of deposited copolymer. This introduces an increased risk of contaminating the surface with impurities that may contribute to the isotherm. To examine this

possibility, three trials using 1000 μL of 99.9+% chloroform (the same volume as the 0.10 mg/mL trial) were carried out. For the resulting compression isotherms, the observed surface pressure did not exceed 0.4 mN/m over a full compression, indicating that impurities from the largest solvent volumes employed do not contribute significantly to the isotherms.

2.2.4. Langmuir-Blodgett

Langmuir films were prepared as described above (Section 2.2.3) on the KSV 3000, except the volume of the spreading solution was exactly half. This was necessary to optimize the transfer ratio (1.1 ● 0.2), and independent AFM analysis confirmed that the volume deposited had no discernable influence on the surface morphologies. All other parameters were identical to that of the $\pi - A$ section up to the transfer point, where the desired π was maintained for 10 minutes, followed by an upward transfer of a submerged substrate. Glass substrates (VWR Scientific 18 x 18 mm^2) were cleaned first with methanol, sonicated (Branson 3510) in spectroscopic-grade chloroform (99.8%, Aldrich) for 20 min, dried, and used immediately. All transferred thin films were dried vertically for a minimum of 12 h and imaged within a week.

2.2.5. Atomic Force Microscopy

All AFM imaging was conducted on a Veeco (ThermoMicroscopes Explorer) instrument equipped with a Veeco tip (NanoProbe-MLCT-EXMT-A) run in contact mode. Tip velocity was typically maintained at 10 μm/s, and the resolution of each image was held at 500 scans/image. The AFM tips have a radius of < 50 nm, resulting in a

maximum systematic error in lateral dimensions of <15 nm (calculated on the basis of geometrical considerations of the tip and surface features); this error is significantly less than the standard deviations of feature widths reported in Table 2.1. To ensure that the friction of the tip did not perturb the surface features, a 10 μm × 10 μm area was imaged several times followed by a 20 μm × 20 μm scan of the same region; there was no obvious agitation of the observed aggregate structures from tip contact during the repeated scans. The AFM probe was housed within a vibration-resistant case on a vibration isolation platform maintained at 80 psi (Newport). Each sample was imaged several times at different locations on the substrate to ensure reproducibility. In all cases, the imaging of LB films was performed far from the edge of the glass substrate to minimize any local effects caused by turbulent water flow at the boundary and meniscus effects during transfer. In some cases, brightness, contrast, and contour levels of AFM images were adjusted to improve clarity for presentation, however, statistical analysis was conducted on unmodified images.

2.3. Results and Discussion

2.3.1. Surface Pressure – Area Isotherms

An analysis of π- A isotherms for the 141k, 11.4 wt% PEO copolymer was carried out for a range of spreading solution concentrations from 0.10 to 2.0 mg/mL. For these experiments, the mass of polymer deposited on the interface was held constant, such that the volume of deposited solution varied with the concentration of spreading solution. At least five isotherm trials were completed for each reported concentration.

Figure 1 shows representative π - A isotherms of deposition / compression experiments for monolayers deposited from 0.10 and 0.50 mg/mL solutions.

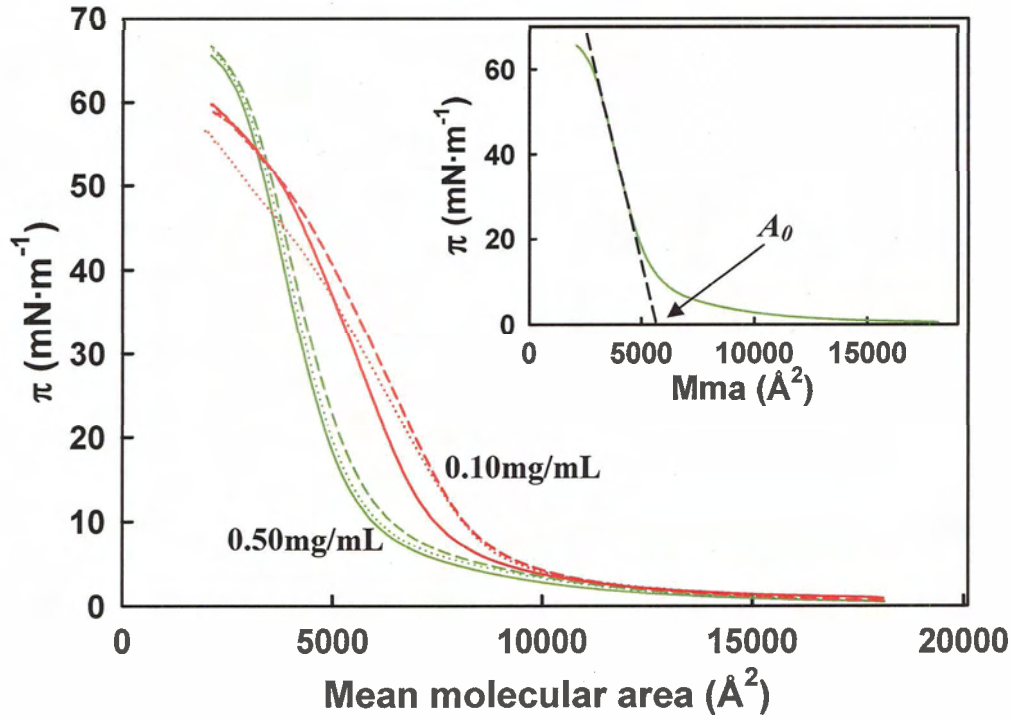

Figure 2.1. Triplicate π - A isotherms of PS-*b*-PEO spread from 0.50 mg/mL (green) and 0.10 mg/mL (red) chloroform solutions at the air-water interface. Solid, dotted, and dashed lines represent replicate trials for each concentration.

PS-*b*-PEO films in which the limiting PEO pancake area is sufficiently greater than the PS block limiting area in air show isotherms with a significant plateau region of constant $\pi \sim 10$ mN/m,[17-20,43,44,47] associated with overlap of PEO chains above a critical surface density such as is found in isotherms of pure PEO homopolymer.[18,22,44,51] However, as the relative area of the PS block increases, steric interactions between PS domains and repulsive interactions between PS and PEO at the air-water interface begin to hinder the PEO phase transition, such that the plateau region becomes less prominent,[15,18,21] until isotherms resemble those obtained for PS homopolymer.[49,50] The isotherms obtained in the present study were consistent with a significant contribution from the PS domains, showing no plateau or pseudoplateau at $\pi \sim 10$ mN/m for any concentration of spreading solution (Figure 2.1). However, despite the absence of these features, the isotherms were markedly different from those reported for monolayers of PS homopolymer in which a more sudden increase in surface pressure at the onset of the liquid condensed phase is observed.[50,53] The present isotherms for the 11.4 wt%-PEO polymer at different concentrations of spreading solution showed that, in all cases, the surface pressure gradually increased with compression up to $\pi \sim 8$ mN/m, followed by a marked increase in slope near this point (π_{on}). Beyond π_{on}, the surface pressure increased with decreasing mean molecular area until the collapse pressure, π_c, was reached (~ 60 - 70 mN/m). Studies on PS homopolymer have shown π_c to be ~ 60-70 mN/m.[50]

Since none of our isotherms showed a plateau or pseudoplateau, the independent determination of a limiting pancake area, $A_{0,p}$, and limiting brush area, $A_{0,b}$, as defined by Goncalves da Silva, was not possible.[17] However, for each isotherm, a limiting mean molecular area, A_0, could be determined by extrapolation of the maximum slope of the

isotherm to $\pi = 0$ (Figure 2.1, inset). This was achieved by determining the inflection point of the π - A isotherm (defined by $d^2\pi/dA^2 = 0$) and extrapolating the tangent at this point to $\pi = 0$. The A_0 values for PS-*b*-PEO films deposited from spreading solutions in the range of 0.10 - 2.0 mg/mL were determined from five replicate trials and are reported in Figure 2.2. At spreading solutions $\geq$ 0.50 mg/mL, the limiting mean molecular areas are fairly constant for different spreading concentrations, with $A_0 \sim 5400$ Å^2/(PS-*b*-PEO) or ~15 Å^2/PEO monomer. This limiting area is in reasonable agreement with the area of the PS block predicted from Kumaki's results,[50] 5000 Å^2, and significantly less than the predicted limiting area of the PEO pancake from the literature value of 27 Å^2/monomer,[17] 9800 Å^2/(PS-*b*-PEO). This suggests that, for higher concentrations of spreading solution, the increase in surface pressure upon compression is dominated by the overlap of PS blocks; as well, the effective area of the PEO blocks is significantly reduced from the predicted pancake value for more hydrophilic diblocks, as found by Devereaux et al. for a PS-*b*-PEO diblock with 7 wt% PEO.[21] The latter effect may be explained by repulsive interactions between PS and PEO at the air-water interface, which force some of the PEO monomers to become desorbed from the interface prior to reaching the critical surface density.

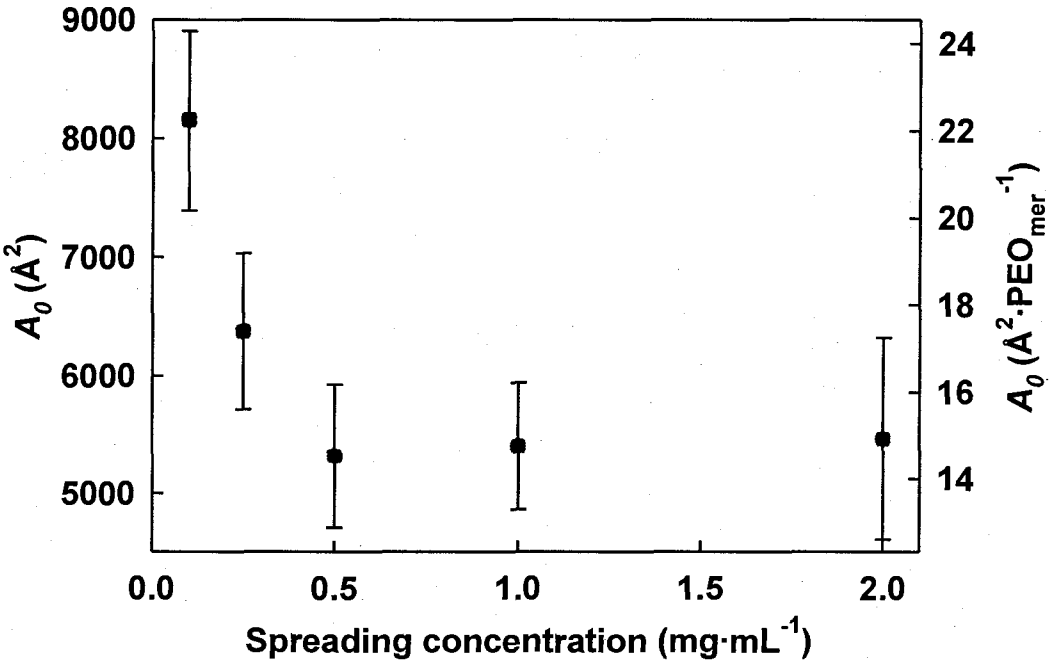

Figure 2.2. Plot of limiting mean molecular area (A_0) versus spreading solution concentration for PS-*b*-PEO monolayers deposited from chloroform solutions at the air – water interface.

Of particular interest is the significant increase in A_0 with decreasing spreading solution concentration for concentrations $\leq$ 0.25 mg/mL, with average A_0 values of 6400 Å^2 (~17 Å^2/PEO monomer) determined for a spreading solution of 0.25 mg/mL and 8200 Å^2 (~22 Å^2/PEO monomer) for a spreading solution of 0.10 mg/mL (Figure 2.2). Similar to isotherms from higher deposition concentrations, the 0.25 and 0.10 mg/mL isotherms show no plateau for the PEO phase transition, although the limiting areas are significantly higher than the limiting area of PS blocks (5000 Å^2),[50] increasing toward the PEO pancake area as the deposition concentration decreases. The monolayer compressibility (C_m) was also determined using $C_m = -1/A_0\ (\partial A/\partial \pi)_T$, (Figure 2.3), where $(\partial A/\partial \pi)_T$ was taken at the inflection point of the π - A isotherm, and results for different spreading

solution concentrations were compared. Interestingly, the compressibility values of monolayers from spreading solutions ≤ 0.25 mg/mL are within 10% of that of a pure PS monomolecular particle film (7.8×10^{-3} m/mN),[50] whereas the monolayer compressibility for the most dilute (0.10 mg/mL) spreading solution was found to be 10.9×10^{-3} m/mN, indicating a significantly more compressible film than either collapsed PS monomolecular films or the PS-*b*-PEO cast from the more concentrated solutions. We note that the maximum compressibility from our most dilute spreading solution concentration is still much less than the C_m of PEO homopolymer (50×10^{-3} m/mN; calculated from data in ref 48), and the limiting area is still less than the predicted PEO pancake area of 27 Å^2/PEO monomer. These trends in C_m and A_0 suggest that the interfacial adsorption of PEO monomers increases as the spreading solution concentration decreases below a critical value, increasing the monolayer limiting area and compressibility beyond that of the PS blocks alone. To our knowledge, this is the first time that this effect has been reported. Baker et al. have reported that the formation of surface aggregates is affected by the concentration of the spreading solution for a largely hydrophobic PS-*b*-PEO diblock, and this was attributed to a decrease in PS entanglement before and during solvent evaporation.[20,21] Chain entanglement effects can also explain the observed dependence of the A_0 and C_m on the spreading solution concentration since a decrease in PS entanglement would result in less kinetic restriction to the favourable spreading of PEO blocks, allowing a greater percentage of PEO monomers to be adsorbed at the air-water interface following solvent evaporation. To further explore this possibility, we consider differences in the morphology of PS aggregates formed from spreading solution concentrations corresponding to the aforementioned isotherm data.

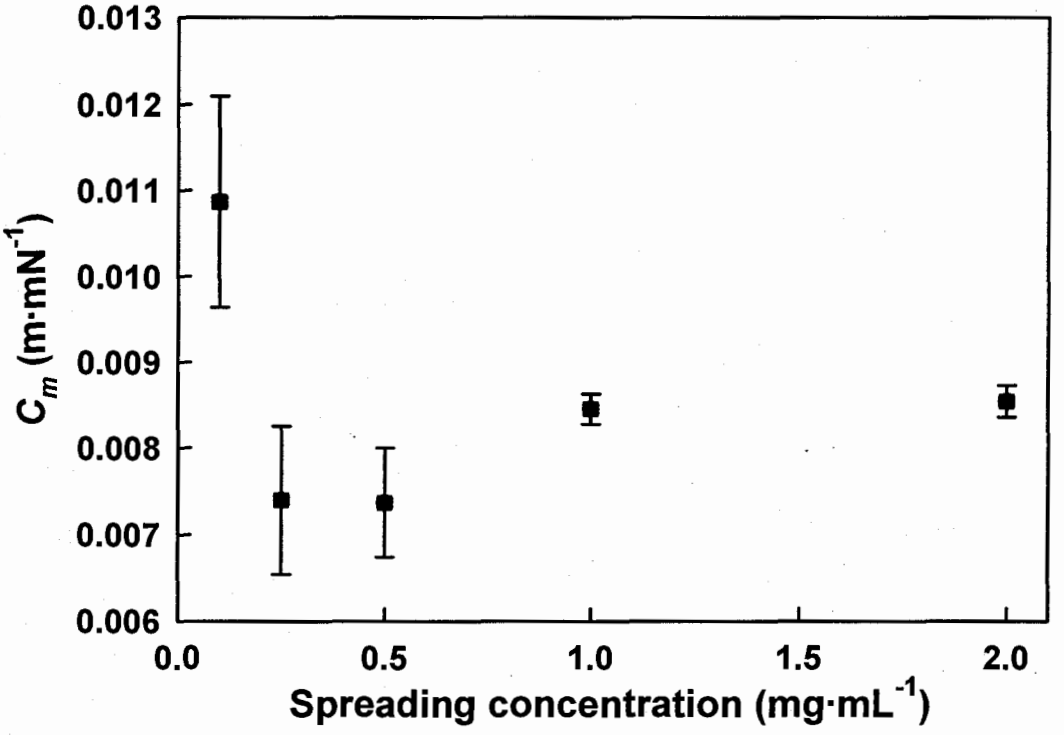

Figure 2.3. Plot of compressibility (C_m) versus spreading solution concentration for PS-*b*-PEO monolayers deposited from chloroform solutions at the air-water interface.

2.3.2. Langmuir-Blodgett Film Morphology

The structure of PS surface aggregates at the air-water interface was determined from AFM images of PS-*b*-PEO monolayer films transferred to a glass substrate via the LB method (Figures 2.4 - 2.6). Inspired by the recent results of Devereaux et al.,[21] and considering the observed effect of spreading solution concentration on isotherms obtained in the present system, we have investigated LB film morphology of the 141k, 11.4 wt% PEO copolymer for different spreading solution concentrations in the range of 0.10 - 2.0 mg/mL. Unless otherwise stated, compression speed and deposition pressure were held constant at 10 mm/min and 2.0 mN/m, respectively; these parameters have been shown to have a minimal influence on the overall aggregate structure[21] since PS aggregates at the air-water interface become kinetically "frozen" and resistant to morphological transformation following solvent evaporation.[14,20,21] This assumption was briefly investigated by imaging several LB films transferred at deposition pressures of 0.5 and 4.0 mN/m. The aggregate morphologies observed after transfer at different surface pressures were found to be identical to structures observed after transfer at 2.0 mN/m. A total of ~ 300 images from ~ 50 separate LB films over a range of spreading solution concentrations was collected and analyzed. To ensure no systematic bias in the sampling procedure, several AFM images were taken at random on each substrate. Each LB film was transferred from a separate monolayer deposited onto a clean air-water interface.

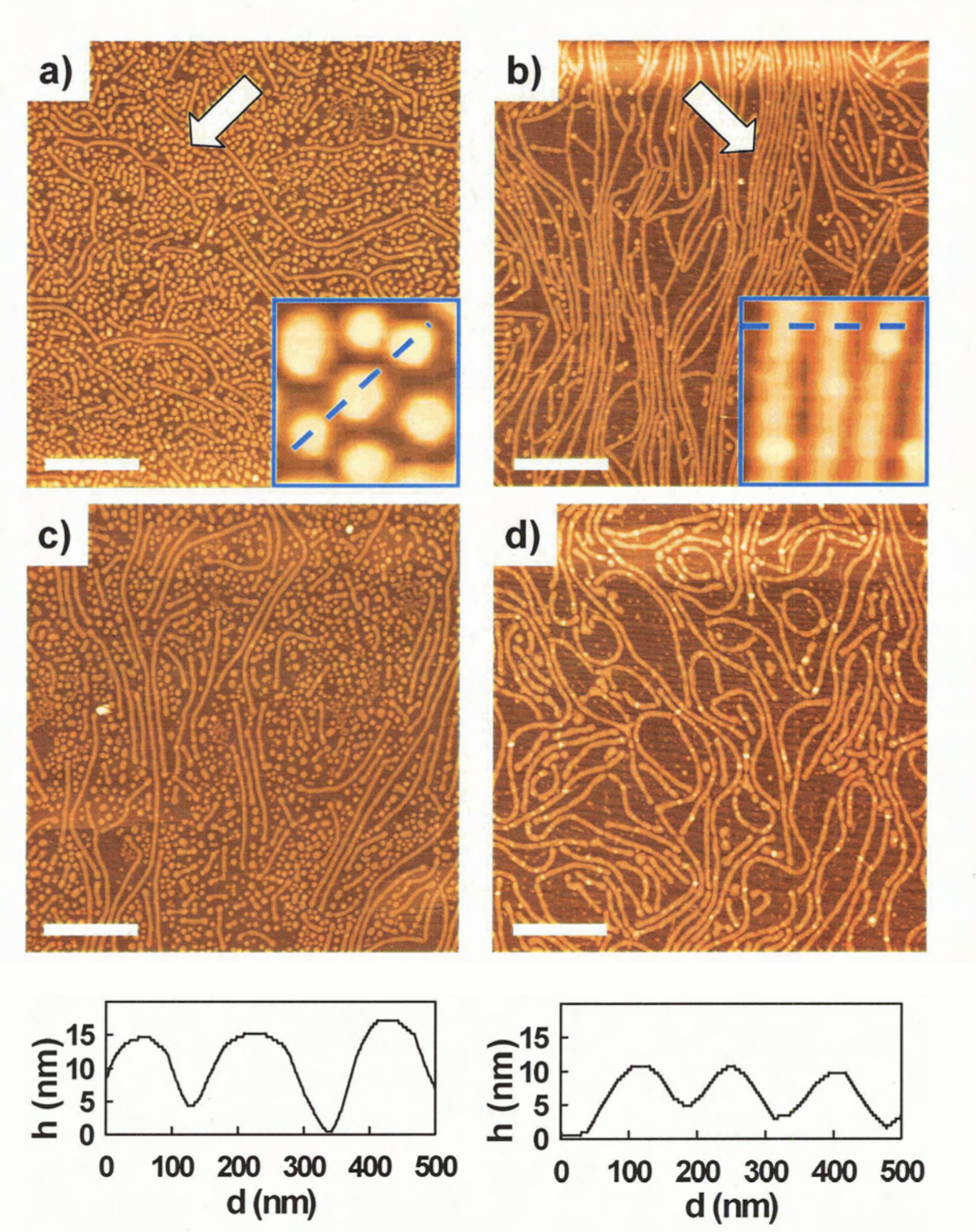

Figure 2.4. Representative AFM images of spaghetti and dot morphologies for PS-*b*-PEO transferred from the air-water interface by the Langmuir-Blodgett technique at 2.0 mN/m. Spreading solution concentrations were (a, b) 0.75 mg/mL and (c, d) 0.50 mg/mL. Scale bars represent 2 μm, and edge lengths for insets are 0.5 μm.

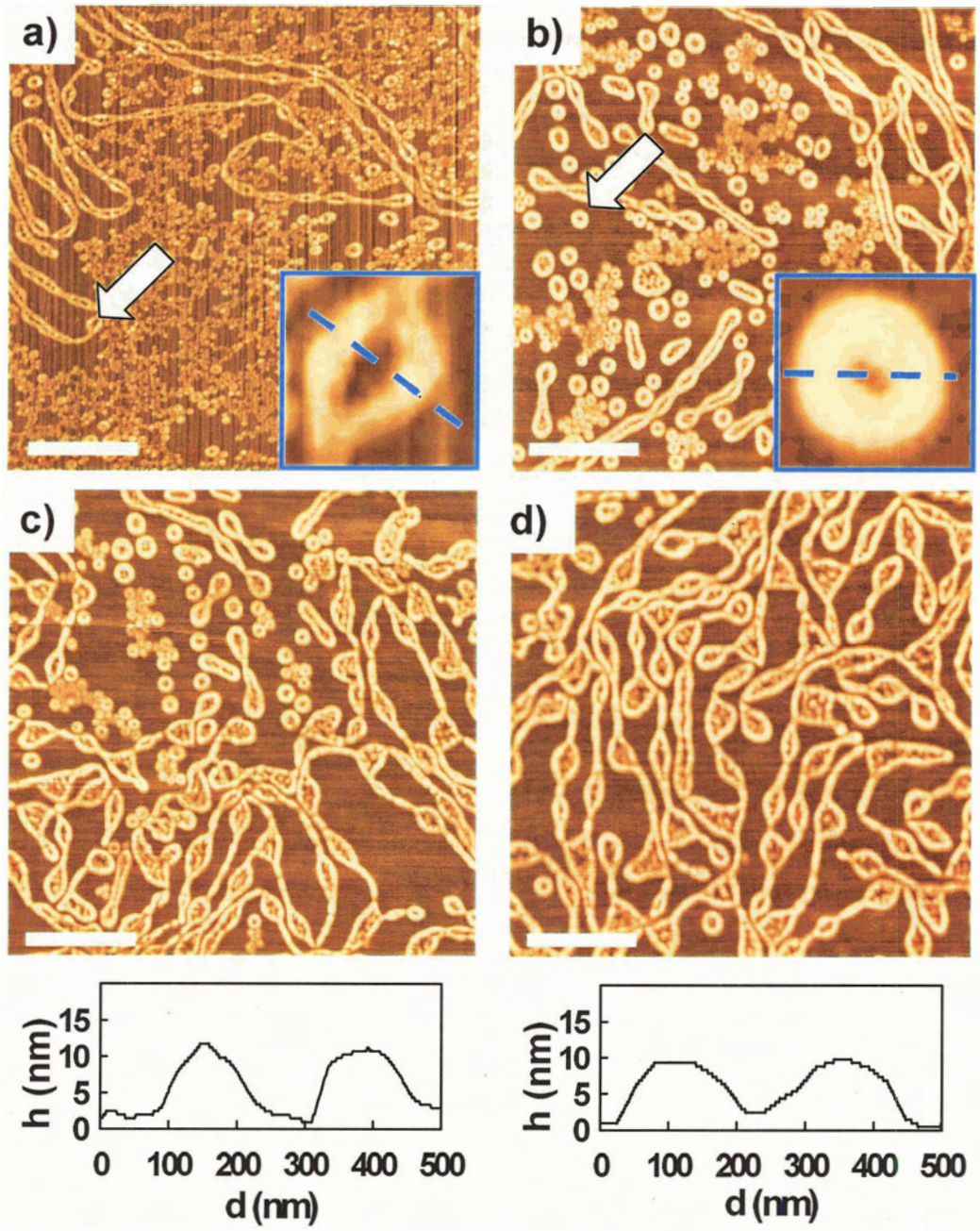

Figure 2.5. Representative AFM images of budding spaghetti morphologies for PS-*b*-PEO transferred from the air-water interface by the Langmuir-Blodgett technique. Spreading solution concentration was 0.25 mg/mL and transfer surface pressures were 2.0 mN/m. Scale bars represent 2 μm and edge lengths for insets are 0.5 μm.

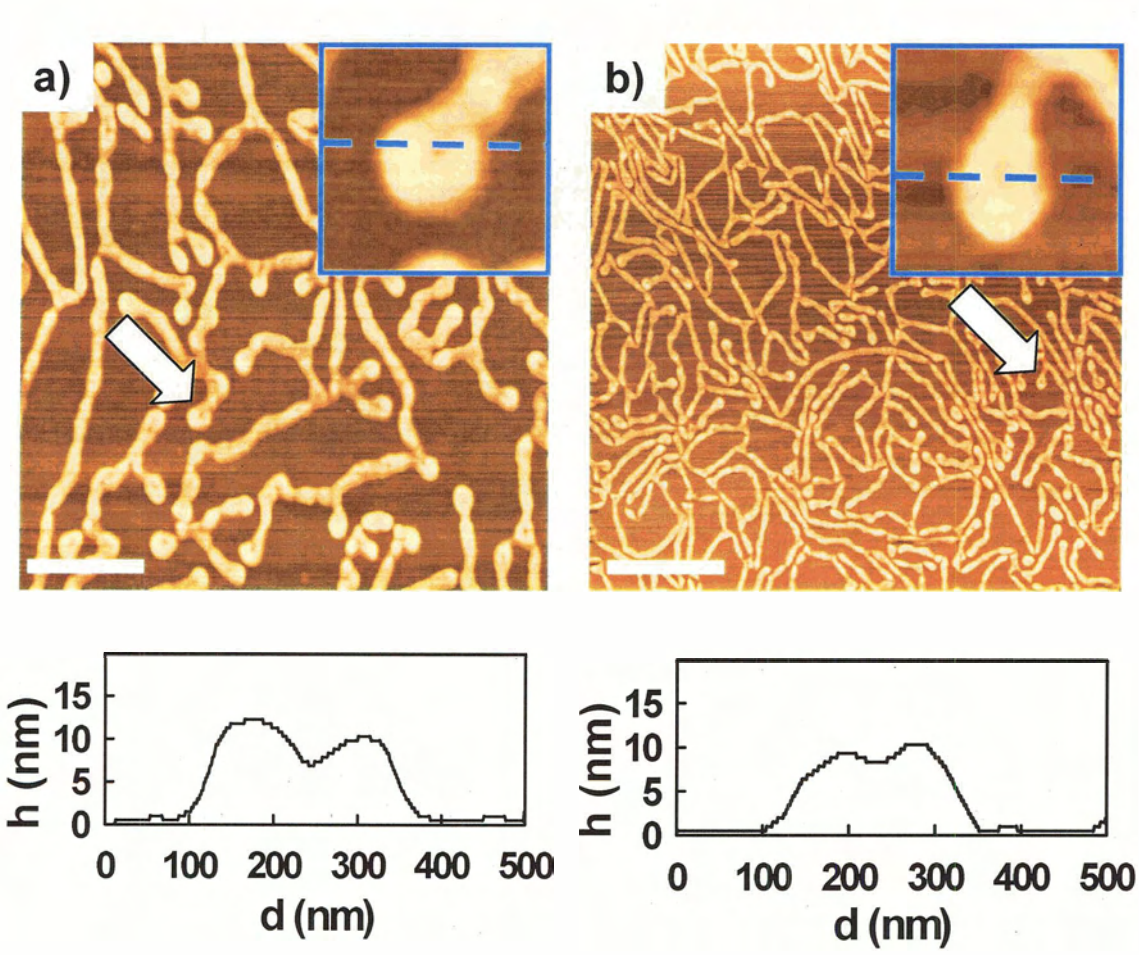

Figure 2.6. Representative AFM images of ring and chain morphologies for PS-*b*-PEO transferred from the air-water interface by the Langmuir-Blodgett technique at 2.0 mN/m. Spreading solution concentration was 0.50 mg/mL. Scale bar represent (a) 1 μm, and (b) 2 μm edge lengths for insets are 0.5 μm.

2.3.2.1. Concentration Dependence of Surface Features

For each concentration of spreading solution, a mixture of aggregate types was observed, as in previous systems of largely hydrophobic PS-*b*-PEO diblock copolymers.[15,21] At all spreading solution concentrations, features described as dots and spaghetti were present, consistent with previous results.[15,21] Figure 2.4 shows representative images of dots and spaghetti features obtained at spreading concentrations of 0.75 (a, b) and 0.50 mg/mL (c, d), highlighting both dot-rich (a, c) and spaghetti-rich (b, d) regions of each film. There was no evidence of large planar aggregates (termed continents in previous studies)[15,21] in any of our experiments. Continents have been ascribed by Devereaux et al. to a high degree of PS chain entanglement restricting spreading of the copolymer before solvent evaporation, resulting in structures with extremely large lateral dimensions.[21] Compared to this previous study,[21] both the percentage of PEO and overall length of the PEO block is greater in the present case, which should facilitate increased diblock spreading at all solution concentrations, explaining the absence of continents. However, we point out that kinetic factors attributed to chain entanglement must still play an important role in the formation of aggregates in this system on the basis of the observed mixture of different surface features and the effect of spreading solution concentration

Along with dots and spaghetti, two new types of features, termed rings and chains, became prominent features for the two lowest concentrations of spreading solutions (0.25 and 0.10 mg/mL). To our knowledge, this is the first example of 2D rings and chains resulting from the self-assembly of linear, amphiphilic diblock copolymers at the air-water interface. Figure 2.5 shows representative images of these novel PS-*b*-PEO

aggregates cast from 0.25 mg/mL solutions. Rings and chains were observed only very rarely at spreading concentrations ≥ 0.50 mg/mL, becoming frequently observed at 0.25 mg/mL, and increasing further in frequency at 0.10 mg/mL. Due to the presence of a diverse range of surface features present at all concentrations, it was difficult to come up with a comprehensive statistical approach to measure the apparent trends. To this end, the following simple approach was used to quantify the occurrence of rings and chains: each of the 275 AFM images that showed predominately chains and / or rings (i.e. ≥ 50% of the total image area contained rings and / or chains) was counted. The number of images that satisfied this condition was divided by the total number of images at that concentration and expressed as a percentage. With the exception of the 1.5 mg/mL spreading solution, our analysis of each concentration involved a minimum of 16 images from at least 3 separate LB films. These data are plotted in Figure 2.7, which clearly shows that rings and chains were extremely rare for spreading concentrations ≥ 0.50 mg/mL, but their occurrence increased sharply at concentrations ≤ 0.25 mg/mL, being found in ~75 % of images for the lowest concentration of spreading solution (0.10 mg/mL).

A fifth type of structure, classified as "budding spaghetti" was observed only for the intermediate concentration of spreading solution (0.50 mg/mL) and is believed to be a transitional morphology between spaghetti and chains (Figure 2.6). Importantly, the transition from mainly dots and spaghetti features to a high occurrence of rings and chains for spreading solution concentrations ≤ 0.25 mg/mL coincides with the observed increase in the limiting mean molecular area for spreading concentrations ≤ 0.25 mg/mL

(Figure 2.2). The relationship between the concentration dependence of isotherm data and surface morphologies is discussed in Section 2.4.1.

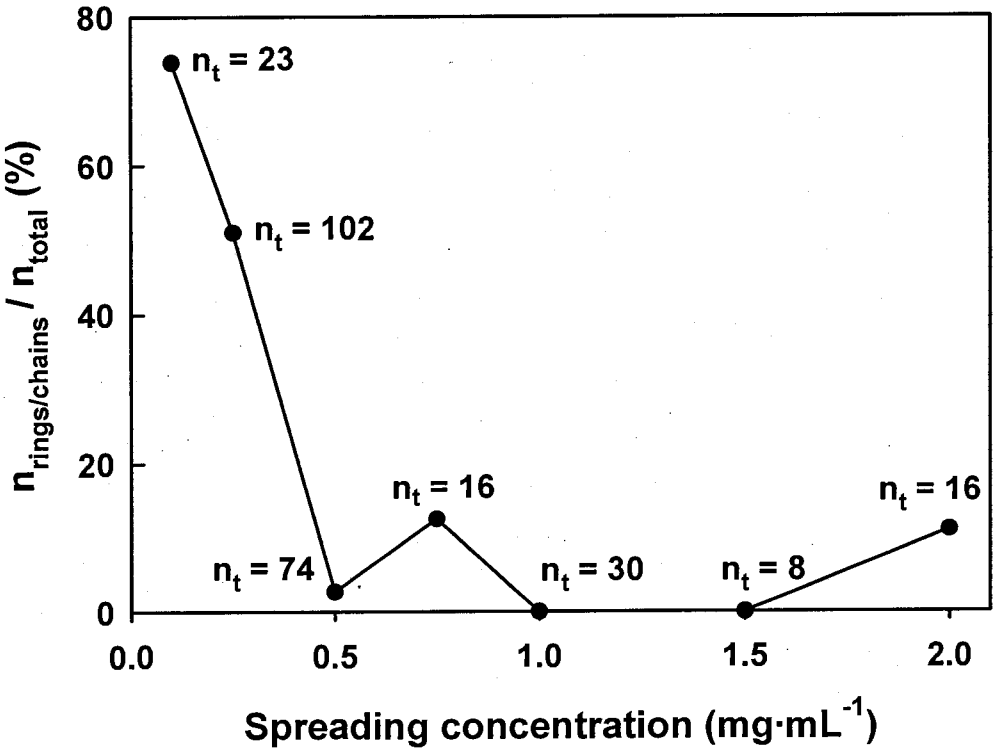

Figure 2.7. Percentage of AFM images showing predominately (> 50 %) ring and chain morphologies for different concentrations of spreading solutions. n_t indicates the total number of images evaluated at each concentration of spreading solution.

2.3.2.2. Characteristics of Surface Features

Table 2.1 describes the mean dimensions of the various surface features observed over a range of spreading solution concentrations. In determining the sizes of the observed features, image analysis software that could categorically differentiate between all of the observed morphologies was not available, and so this was completed manually. To classify the heights and widths of the observed aggregates, random sections of suitable images were selected and each surface feature was counted and measured. Surface features fitting the criteria described below were measured using the AFM software (SPM Labs) and compiled. At least 100 individual structures were measured for each of the reported morphologies.

Dots were observed at all concentrations of spreading solutions and are defined as features with roughly circular topology and bilateral aspect ratios less than 2:1. To distinguish dots from rings, dots that showed marked depressions (dimples) near the centre of the structure were excluded from the definition. No upper limit of diameter was applied to the classification of dots since the vast majority aggregates satisfying the aspect ratio and dimple restriction were < 400 nm. A lower limit of 125 nm was applied to the dots since a second population of smaller, more irregular circular aggregates was also present in many images (not shown). The majority of these smaller structures were not symmetrical, having aspect ratios outside the set limit of 2:1, and thus could also be excluded on this basis. Like dots, these smaller aggregates were noted in many of the AFM images for all concentrations of spreading solution.

In the vast majority of images that contained dots, more laterally extended spaghetti[20,21,54] structures were also present (Figure 4). Spaghetti is presently defined as

aggregates with bilateral aspect ratios greater than 3:1. No limit was put on the width or length of the structures; however, to distinguish spaghetti from budding spaghetti or chains, any significant height depression along the long axis of the structure excluded the feature from the spaghetti classification. Typical spaghetti features had aspect ratios far in excess of 3:1 and extended for many micrometers with consistent width. They appeared to resist fracture upon bending and often terminated with a hemispherical cap. As indicated by average dimensions given in Table 2.1, when the above criteria are applied to the various features, the mean widths of dots (160 nm) and spaghetti structures (170 nm) are remarkably similar, with relatively low standard deviations of < 20%.

The mean heights of dots (16 nm) and spaghetti (12 nm) from Table 2.1 can be compared with the calculated diameter of a spherical PS particle consisting of a collapsed globule of the PS block in air, using the Kumaki area[50] as the cross-section of the sphere.[21] This gives a predicted height of an individual PS block of ~ 8 nm, which suggests that dots and spaghetti structures are comprised of a monolayer of PS blocks, with PS chains extended away from the water surface relative to the height of a collapsed globule in a brushlike fashion. The fact that spaghetti features are shorter than dots indicates more extensive lateral entanglement of PS blocks in the former case and a less-compressed brush. Importantly, the widths of dots and spaghetti are ~ 20 times the dimensions of a single PS block, indicating that a large number of diblocks must overlap to form the observed surface features.

Table 2.1. Mean dimensions and standard deviations of PS-*b*-PEO surface features determined through AFM on LB films

	spaghetti	dots	rings	chains
width (nm)	160 ± 20	170 ± 30	170 ± 20	170 ± 30
height (nm)	12 ± 2	16 ± 2	10 ± 2	10 ± 2

As previously mentioned, rings and chains become prevalent features for spreading solution concentrations $\leq$ 0.25 mg/mL (Figure 2.7). Rings were defined as pseudocircular aggregates having an outer aspect ratio of less than 3:1 and showing a hole in the centre. The outer diameters of rings were polydisperse, ranging from ~ 300 nm to ~ 1 μm, although as indicated in Table 2.1, the ring walls showed relatively low polydispersity with mean dimensions of 170 nm, nearly identical to dot and spaghetti dimensions. Paralleling the dot and spaghetti morphologies, ring structures were generally accompanied by extended structures of connected links, which we term chains. Chains were defined as extended aggregates possessing two walls that are "pinched" or joined in a periodic manner along the length of the chain. In several cases, the chains contained smaller aggregates inside the links, occasionally joining the link walls. Chain links show some similarity to rings, with identical average wall dimensions (~ 170 nm), although chain links are generally elongated along the length of the chain. It should be noted that the observed chain morphology is quite different from a conventional 3D chain in that adjacent links were neither rotated 90° with respect to the subsequent link nor were the chain walls twisted in a helical fashion, as evidenced by the inset of Figure 2.5a which shows that the connection point between links has the same height as the chain walls. The mean wall heights of both rings and chains are 10 nm, somewhat shorter than dots and spaghetti and closer to the expected height of a single collapsed PS globule. Although we can only speculate on the packing density of chains within the various surface features, the shorter dimensions of rings and chains suggest that PS chains in these structures are less densely packed than in dots and spaghetti and therefore less brushlike.

A fifth morphology was observed only for spreading solution concentrations of 0.50 mg/mL (Figure 2.6). These aggregates appear at first glance to be spaghetti-like, although closer inspection reveals dimples at a swelled terminal end and depressions along the backbone of the structure. Unlike chains, which show obvious depressions extending to the water-substrate surface, these deviant structures, termed budding spaghetti, exhibit subtle depressions of smaller lateral diameter that do not appear to extend to the interface, as shown in the topology profiles in Figure 2.6c and d; however, we note that accurate determination of the height profiles for these depressions is somewhat limited by their small lateral dimensions relative to the maximum diameter of the AFM tip.

2.4. Discussion

2.4.1. Relationship of LB Film Structure to π–A Isotherms

A key result of this study is the correspondence between an increase in the occurrence of rings and chains in the LB films and an increase in the isothermal A_0 and C_m below a critical concentration of spreading solution. In this section, we discuss the relationship between the concentration dependence of surface morphologies and isotherm data, which provides some insight into the formation of these novel block copolymer surface features under controlled conditions.

The formation of PS-*b*-PEO surface features in LB films has been shown by Cox et al. to be a result of spontaneous copolymer aggregation at the air-water interface, rather than a transfer of micelles formed in the spreading solution.[15] Those authors carried out dynamic light scattering (DLS) on various concentrations of PS-*b*-PEO in chloroform and

found no evidence of micelle formation in the spreading solutions; as well, it was shown that the observed surface morphologies were the same for different spreading solvents, indicating that surface aggregation was a result of copolymer interactions with the air-water interface as the solvent evaporated and was not simply micelle formation in solution induced by an increase in concentration.[15] DLS measurements (not shown) on our most concentrated (2.0 mg/mL) PS-*b*-PEO solution confirmed that no micellar aggregates were present, in agreement with previous results.[15] This suggests that the formation of the observed surface features in Figures 2.4 – 2.6 arise from an interfacial self-assembly process where an interplay of attractive interactions between PEO and the water surface and repulsive interactions between PS and water and PS and PEO drive the assembly in the timescale of solvent evaporation. The spreading solvent medium is required to provide sufficient mobility for the chains to rearrange and optimize their free energy, such that the evaporation of chloroform, along with inducing self-assembly, ultimately "freezes" the system in a kinetic, nonequilibrium state.

Devereaux et al. have demonstrated the effect of PS chain entanglement on the development of PS-*b*-PEO surface features during evaporation of the spreading solvent, by showing that in their system (MW = 51k, 7 wt% PEO) higher concentrations of spreading solution resulted in a larger predominance of continents, whereas a lower concentration resulted in dots being predominant.[21] Compared to dots, continents were seen to be kinetically trapped further from equilibrium, since larger degrees of chain entanglement at higher concentrations restricted the thermodynamically favourable spreading of the PEO blocks at the air-water interface. In less-hydrophobic systems, the relative contribution of PS chain entanglement is minimal and uniform nanoscale dots are

generally observed with no dependence on the concentration of spreading solution. The present diblock copolymer (MW = 141k, 11.4 wt%) is found to present an intermediate situation, where PS entanglement is not sufficient to result in the formation of continents, although some entanglement effects do exist since a mixture of surface features is always observed, with the predominance of features being dependent on the concentration of spreading solution. In the present case, we find exclusively dots and spaghetti at the higher concentrations of spreading solution (> 0.50 mg/mL), although for the intermediate concentration (0.50 mg/mL), dimples and depressions are found to develop in the spaghetti structures (budding spaghetti). This suggests that spaghetti structures are in fact kinetically trapped by PS chain entanglement, and the formation of budding spaghetti represents a transition to a new morphology with lower free energy, facilitated by less-severe entanglement at a lower spreading concentration. At even lower concentrations (≤ 0.25 mg/mL), the system is allowed to progress further toward equilibrium before the solvent evaporates since PS entanglement will be even less significant. The result appears to be the formation of the chain morphology from the budding spaghetti structures. The fact that rings and chains are almost always found in the same region of the substrate further suggests that chain links may separate to form rings. The observed dependence of aggregate morphology on the concentration of spreading solution highlights the fact that morphological diversity in the 2D self-assembly of mainly hydrophobic PS-*b*-PEO is a kinetic phenomenon[11,21] resulting from various degrees of trapping in nonequilibrium states. This contrasts the range of morphologies observed from the 3D self-assembly of PS-*b*-PEO[27,55] and other amphiphilic diblock copolymers[56] in aqueous media, which is generally attributed to

different equilibrium states arising from changes in copolymer conformation or environment.

Independent of the AFM study of surface features, our isotherm data suggest that PS chain entanglement also determines the extent of PEO adsorption at the air-water interface following solvent evaporation; below a critical concentration of spreading solution, isotherms show an increased contribution from the PEO blocks in the form of positive deviations from the predicted Kumaki limiting area for the PS blocks and an increase in monolayer compressibility. To relate the formation of chains and rings to an increase in interfacial PEO adsorption requires some speculation, although we consider that a model for PS surface aggregates proposed by Cox et al. requires a thin layer of PEO to be located beneath the PS domains in order prevent direct contact between the PS and the water surface.[14] The height of our dot and spaghetti structures suggests that the PS blocks are packed in a brushlike manner, requiring a large number of PEO monomers to exist beneath the aggregates. Repulsive interactions between PS and PEO at the air-water interface would therefore result in desorption of PEO from the water surface for these structures,[18-21] even at low average coverage (i.e., before compression) since the local PS coverage is high in the vicinity of the aggregates; this would explain our observation that, at higher spreading concentrations, where dots and spaghetti predominate, the limiting area is consistent with the Kumaki area of the PS blocks alone. At lower concentrations of spreading solution, where the kinetic restrictions of PS chain entanglement are less severe, we propose that the formation of chains and rings from spaghetti structures prior to solvent evaporation is driven by an increase in interfacial adsorption of PEO monomers. One possibility is that the development of holes in the

budding spaghetti features (eventually leading to chain and ring formation) decreases local PS coverage and therefore decreases interfacial PS-PEO repulsion, allowing PEO blocks beneath the aggregates to become adsorbed at the air-water interface. As well, the height of chain and ring features (Table 2.1) suggests that the diblocks in these aggregates are less densely packed than in spaghetti and dots, which should also decrease the repulsive effect of PS on the PEO blocks and improve the interfacial adsorption of PEO monomers. We point out that, despite the observed effects of spreading concentration, none of our isotherms show the characteristic plateau of more hydrophilic diblocks; this lack of an observed PEO phase transition highlights the fact that compression isotherms in the present system are strongly influenced by the PS blocks, which exert significant interfacial repulsion on PEO monomers underneath the various surface aggregates. However, this study demonstrates that that the extent of this interfacial repulsion, the resulting conformation of PEO blocks, and the structure of the surface aggregates can all be kinetically tuned via the concentration of spreading solution.

2.4 Conclusions

A 141K, 11.4 wt% PEO PS-*b*-PEO diblock copolymer was deposited on the air-water interface from chloroform solutions of various concentrations. The 2D self-assembly of the copolymer was monitored via AFM images of the thin films transferred through the LB method. The compression isotherm behavior for the monolayers at the air-water interface was also determined. Consistent with a recent previous study,[21] the concentration of spreading solution was found to influence the predominance of certain

aggregate morphologies. Concentrated spreading solutions ($\geq$ 0.50 mg/mL) resulted in mainly nanoscale dots and spaghetti structures at the air-water interface, whereas dilute spreading solutions ($\leq$ 0.25 mg/mL) yielded unprecedented ring and chain structures. Additionally, the crossover spreading solution concentration (0.50 mg/mL) formed a "budding spaghetti" morphology, which appears to be a transitional morphology between spaghetti and chains. π- A isotherms provided further evidence for the influence of spreading solution concentration on self-assembly at the air-water interface, showing a marked concentration dependence in the lower concentration regime where the ring and chain morphologies became predominant. The limiting mean molecular areas and compressibilities of the monolayers appeared to be dominated by the PS blocks at higher spreading concentrations, whereas a greater contribution from the PEO blocks was observed in the dilute regime. These results highlight the kinetic nature of the surface features formed from nanoscale self-assembly of largely hydrophobic PS-*b*-PEO diblocks at the air-water interface, demonstrating the potential for tunable patterning of novel nanoscale features (rings and chains) via simple control of preparation conditions.

2.5 References

(1) Whitesides, G. M.; Grzybowski, B. *Science* **2002,** *295*, 2418.

(2) Xia, Y.; Rogers, J. A.; Paul, K. E.; Whitesides, G. M. *Chem. Rev.* **1999,** *99*, 1823.

(3) Zhu, J.; Eisenberg, A.; Lennox, R. B. *Langmuir* **1991,** *7*, 1579.

(4) Zhu, J.; Eisenberg, A.; Lennox, R. B. *J. Am. Chem. Soc.* **1991,** *113*, 5583.

(5) Zhu, J.; Eisenberg, A.; Lennox, R. B. *J. Phys. Chem.* **1992,** *96*, 4727.

(6) Zhu, J.; Eisenberg, A.; Lennox, R. B. *Macromolecules* **1992,** *25*, 6547.

(7) Li, S.; Hanley, S.; Khan, I.; Varshney, S. K.; Eisenberg, A.; Lennox, R. B. *Langmuir* **1993,** *9*, 2243.

(8) Meszaros, M.; Eisenberg, A.; Lennox, R. B. *Faraday Discuss.* **1994,** *98*, 283.

(9) Li, Z.; Zhao, W.; Quinn, J.; Rafailovich, M. H.; Sokolov, J.; Lennox, R. B.; Eisenberg, A.; Wu, X. Z.; Kim, M. W.; Sinha, S. K.; Tolan, M. *Langmuir* **1995,** *11*, 4785.

(10) Li, S.; Clarke, C. J.; Lennox, R. B.; Eisenberg, A. *Colloids Surf., A* **1998,** *133*, 191.

(11) Cox, J.; Eisenberg, A.; Lennox, R. B. *Curr. Opin. Colloid Interface Sci.* **1999,** *4*, 52.

(12) Li, S.; Clarke, C. J.; Eisenberg, A.; Lennox, R. B. *Thin Solid Films* **1999,** *354*, 136.

(13) Gragson, D. E.; Jensen, J. M.; Baker, S. M. *Langmuir* **1999,** *15*, 6127.

(14) Cox, J. K.; Yu, K.; Eisenberg, A.; Lennox, R. B. *Phys. Chem. Chem. Phys* **1999,** *18*, 4417.

(15) Cox, J. K.; Yu, K.; Constantine, B.; Eisenberg, A.; Lennox, R. B. *Langmuir* **1999,** *15*, 7714.

(16) Dewhurst, P. F.; Lovell, M. R.; Jones, J. L.; Richards, R. W.; Webster, J. R. P. *Macromolecules* **1998,** *31*, 7851.

(17) Goncalves da Silva, A. M.; Filipe, E. J. M.; d'Oliveira, J. M. R.; Martinho, J. M. G. *Langmuir* **1996,** *12*, 6547.

(18) Faure, M. C.; Bassereau, P.; Carignano, M.; Szleifer, I.; Gallot, Y.; Andelman, D. *Eur. Phys. J., B* **1998,** *3*, 365.

(19) Faure, M. C.; Bassereau, P.; Lee, L. T.; Menelle, A.; Lheveder, C. *Macromolecules* **1999,** *32*, 8538.

(20) Baker, S. M.; Leach, K. A.; Devereaux, C. E.; Gragson, D. E. *Macromolecules* **2000,** *33*, 5432.

(21) Devereaux, C. A.; Baker, S. M. *Macromolecules* **2002,** *35*, 1921.

(22) Barentin, C.; Muller, P.; Joanny, J. F. *Macromolecules* **1998,** *31*, 2198.

(23) Zhang, L.; Barlow, R. J.; Eisenberg, A. *Macromolecules* **1995,** *28*, 6055.

(24) Zhang, L. E., A. *J. Am. Chem. Soc.* **1996,** *118*, 3168.

(25) Yu, K.; Zhang, L.; Eisenberg, A. *Langmuir* **1996,** *12*, 5980.

(26) Kwon, G.; Naito, M.; Yokoyama, M.; Okano, T.; Sakurai, Y.; Kataoka, K. *J. Controlled Release* **1997,** *48*, 195.

(27) Yu, K.; Eisenberg, A. *Macromolecules* **1998,** *31*, 3509.

(28) Zhang, L. E., A. *Macromolecules* **1999,** *32*, 2239.

(29) Discher, B. M.; Won, Y.-Y.; Ege, D. S.; Lee, J. C.-M.; Bates, F. S.; Discher, D. E.; Hammer, D. A. *Science* **1999,** *284*, 1143.

(30) Burke, S. E.; Eisenberg, A. *Langmuir* **2001,** *17*, 8341.

(31) Luo, L.; Eisenberg, A. *Langmuir* **2001,** *17*, 6804.

(32) Burke, S. E.; Eisenberg, A. *Langmuir* **2001,** *17*, 6705.

(33) Burke, S. E.; Eisenberg, A. *Polymer* **2001,** *42*, 9111.

(34) Discher, D. E.; Eisenberg, A. *Science* **2002,** *297*, 967.

(35) Eisenberg, A.; Choucair, A. A.; Kycia, A. H. *Langmuir* **2003,** *19*, 1001.

(36) Choucair, A.; Eisenberg, A. *Eur. Phys. J., E.* **2003,** *10*, 37.

(37) Lim Soo, P.; Eisenberg, A. *J. Polym. Sci. Part B: Polym. Phys.* **2004,** *42*, 923.

(38) Shuler, R. L.; Zisman, W. A. *J. Phys. Chem.* **1970,** *74*, 1523.

(39) Kim, M. W.; Cao, B. H. *Europhys. Lett.* **1993,** *24*, 229.

(40) Cao, B. H.; Kim, M. W. *Faraday Discuss.* **1994,** *98*, 245.

(41) Kuzmenka, D. J.; Granick, S. *Langmuir* **1988,** *21*, 779.

(42) Xu, Z.; Holland, N. B.; Marchant, R. E. *Langmuir* **2001,** *17*, 377.

(43) Goncalves da Silva, A. M.; Simoes Gamboa, A. L.; Martinho, J. M. G. *Langmuir* **1998,** *14*, 5327.

(44) Bijsterbosch, H. D.; de Haan, V. O.; de Graaf, A. W.; Mellema, M.; Leermakers, F. A. M.; Cohen Stuart, M. A.; van Well, A. A. *Langmuir* **1995,** *11*, 4467.

(45) Charron, J. R.; Tilton, R. D. *Langmuir* **1997,** *13*, 5524.

(46) Sauer, B. B.; Yu, H.; Tien, C. F.; Hager, D. F. *Macromolecules* **1987,** *20*, 393.

(47) Rivillon, S.; Munoz, M. G.; Monroy, F.; Ortega, F.; Rubio, R. G. *Macromolecules* **2003,** *36*, 4068.

(48) Rother, G.; Findenegg, G. H. *Colloid Polym. Sci.* **1998,** *276*, 496.

(49) Kumaki, J. *Macromolecules* **1986,** *19*, 2258.

(50) Kumaki, J. *Macromolecules* **1988,** *21*, 749.

(51) Sauer, B. B.; Yu, H.; Yazdanian, M.; Zografi, G.; Kim, M. W. *Macromolecules* **1989,** *22*, 2332.

(52) Bailey, F. E.; Koleske, J. V., *Poly(ethylene oxide)*, Academic Press, 1976.

(53) Gaines, G. L., *Insoluble Monolayers at Liquid-Gas Interfaces*, Wiley and Interscience Publishers, 1966.

(54) Peleshanko, S.; Jeong, J.; Gunawidjaja, R.; Tsukruk, V. V. *Macromolecules* **2004,** *37*, 6511.

(55) Yu, K.; Eisenberg, A. *Macromolecules* **1996,** *29*, 6359.

(56) Zhang, L. Eisenberg, A. *Science* **1995,** *268*, 1728.

Chapter 3

Isotherm Behaviour and Aggregate Morphologies in Hydrophobic PS-b-PEO Monolayers: Is Dewetting the Genesis of Pattern Formation?

3.1. Introduction

Previous chapters have demonstrated that nonlithographic techniques leading to controllable structures occupy a fundamental niche in modern materials science. For this reason, there has been much investigation into systems that spontaneously organize into predictable structures and patterns,[1] including significant research focused on the self-assembling properties of amphiphilic diblock copolymers. In particular, amphiphilic diblock copolymer self-assembly at the air-water interface has been a topic of considerable interest for a number of groups, inspired in part by the numerous imaginable applications[2,3] of controllable nanoscale one-dimensional (1D) structures (e.g. nanowires, nanocables, nanorings) and two-dimensional (2D) patterns (e.g. arrays of nanodots, nanowires, etc.).[4-26] When deposited at the surface of water, these polymeric amphiphiles spontaneously organize due to the thermodynamic affinity of the hydrophilic blocks for water and unfavourable interactions between the hydrophobic blocks and water, as well as the relative surface tensions of the two blocks.[17] Many fundamental questions still remain regarding this self-assembly process, the conformations of both blocks within the assembled structures, and the interfacial behaviour of the copolymers under various conditions. To this end, this chapter will build on the findings of Chapter 2 in an effort to further understand the interfacial self-assembly and behaviour of amphiphilic diblock copolymers, specifically polystyrene-*block*-poly(ethylene oxide) (PS-*b*-PEO).

For PS-*b*-PEO block copolymers, patterned monolayers at the air-water interface are generally prepared by depositing solutions of PS-*b*-PEO in chloroform onto a water surface, as demonstrated in the previous chapter, with self-assembly of the diblock being induced by solvent evaporation at the interface. Along with providing a positive

spreading coefficient on water, the chloroform environment also provides mobility for the copolymer during self-assembly, with structures becoming "locked in" by the high glass transition temperature of polystyrene ($T_g \sim 100°C$) once the solvent has evaporated. It has been suggested that the interfacial self-assembly process results from a thermodynamic competition between favourable spreading of the hydrophilic blocks and aggregation of the hydrophobic blocks, along with kinetic effects arising from chain entanglements on the timescale of solvent evaporation and spreading,[25,26] such that the final structures represent a complicated interplay of kinetic and thermodynamic factors. It is well established that surface features are tunable by controlling the relative block lengths at synthesis. For PS-*b*-PEO diblock copolymers, it was found that diblocks with a PEO content of > 15 wt% formed predominately circular surface aggregates,[24] while for more hydrophobic diblocks, significant PS chain entanglements compete with PEO spreading at the interface, resulting in significantly larger aggregates of various morphologies, including planar continents and spaghetti-like wires.[17,25] The possibility of tuning aggregate morphologies via kinetics was recently demonstrated by Devereaux et al.,[25] where it was shown that by simply adjusting the concentration of the spreading solution for a single hydrophobic PS-*b*-PEO diblock copolymer, the predominant surface features could be controlled. As shown in the previous chapter,[26] we furthered this investigation by considering a new PS-*b*-PEO sample, and found that by changing the spreading solution concentration, not only were the predominant surface features controllable, but novel structures were accessible for sufficiently low concentrations which were rarely observed for higher spreading concentrations. When an 11.4 wt%-PEO PS-*b*-PEO diblock copolymer, which we refer to as PS-*b*-PEO(11.4%), was cast from spreading

solutions ≥ 0.50 mg/mL, spaghetti and dot morphologies were observed; however, deposition from more dilute solutions (≤ 0.25 mg/mL) yielded nanoscale rings and chains, the first time these structures had been observed from nonlithographic assembly of block copolymers at the air-water interface.[26]

The characterization of the aforementioned surface morphologies generally requires transfer from the water surface to a solid substrate using the Langmuir-Blodgett technique. However, an appreciable advantage to studying diblock copolymers directly at the air-water interface is the ability to study their surface behaviour via surface pressure (π) – area (A) isotherms of the Langmuir films.[14-26] It is well known that at low surface densities (Γ), PEO exists in a 'pancaked'[27] conformation maximizing interactions with the water surface, and occupying a effective area of 28 – 40 Å^2 per EO monomer.[28,29] At increased Γ, PEO undergoes a phase transition where it desorbs from the interface and becomes solublized in the subphase in a 'brush-like' conformation. This first-order 'pancake-to-brush' phase transition occurs at a constant $\pi \sim 10$ mN/m, the same π at which PEO homopolymer has been observed to desorb.[28,29] The length of the plateau in the isotherm is directly related to the length of the PEO block relative to the length of the PS block.[24] If the PEO block is large with respect to the PS, there exists a significant plateau at $\pi \sim 10$ mN/m, and two limiting mean molecular areas (A_0's) can be defined corresponding to the two phases: the limiting pancake area ($A_{0,p}$), and the limiting brush area ($A_{0,b}$), as defined by Goncalves da Silva[19,20] As the relative contribution of PEO decreases to less than ~15 wt%-PEO however, the characteristic plateau is absent as the pancake-to-brush phase transition is impeded by the large surface area of the PS aggregates, and the limiting pancake area $A_{0,p}$ cannot be determined.[24]

In the previous chapter, we studied the isotherm behaviour of PS-*b*-PEO(11.4%), which was below the composition regime where a pancake-to-brush phase transition is observed, and consequently each isotherm yielded only one A_0 value.[26] Nevertheless, we observed some very interesting effects of spreading solution concentration on the $\pi - A$ isotherms of this system.[26] When the PS-*b*-PEO was cast from dilute solutions below a critical limit ($\leq$ 0.25 mg/mL), we found a significant increase in A_0 from the resulting isotherms, indicating that the conformation and the area occupied by the blocks depends on the extent of chain entanglements during spreading.[26] Interestingly, the observed increase in A_0 corresponded with the appearance of rings and chains, suggesting that the formation of these novel surface features is driven by thermodynamically-favourable conformational changes due to a decrease in chain entanglements in dilute spreading solutions.

As the influence of spreading solution concentration on the $\pi - A$ isothermal behaviour of amphiphilic diblock copolymers had never been documented before, we wished to further our investigation by considering a system that permitted the effects of spreading concentration on both the pancake and brush regimes of the self-assembled structures. This is addressed in the present chapter, by examining a more hydrophilic (18.9 wt%-PEO) diblock copolymer, PS-*b*-PEO(18.9%), which yields a distinct plateau in the compression isotherm, and independently elucidating the effect of spreading concentration on the brush and pancake conformations. It was found that $A_{0,b}$ for PS-*b*-PEO(18.9%) increased below a critical spreading concentration, similar to the trend in A_0 described in the previous chapter for PS-*b*-PEO(11.4%).[26] Interestingly, $A_{0,p}$ was not found to follow the same trend and remained relatively constant as the spreading

concentration decreased, despite the corresponding increase in $A_{0,b}$. This chapter examines this effect and its implications to the surface structure of PS-*b*-PEO aggregates as a function of spreading solution concentration.

In addition to these original investigations, this chapter reports the first study on the influence of spreading solution concentration on compression / expansion hysteresis in PS-*b*-PEO Langmuir films. It has been previously reported that PS-*b*-PEO Langmuir films have expansion cycles that are different from the preceding compression – an effect termed isothermal hysteresis. Hysteresis can be quantified using ΔA_0, which is the difference in limiting mean molecular area on expansion (A'_0) from that obtained on compression (A_0): i.e. $\Delta A_0 = \Delta A_0 - \Delta A'_0$. In previous studies, multiple compression / expansion cycles in both the pancake and brush regimes have been performed on PS-*b*-PEO diblock copolymers at the air-water interface as a function of PEO block length and the temperature of the subphase; it was found that hysteresis in the brush regime ($\Delta A_{0,b}$) decreased with the PEO chain length and temperature, whereas the hysteresis in the pancake regime ($\Delta A_{0,p}$) increased with PEO chain length and decreased with temperature.[19] Hysteresis in the brush regime (high compression) was attributed to PEO cohesion within the brush structure after the initial compression, while hysteresis in the pancake regime (low compression) was related to some irreversible entanglement and hydration of the PEO chains when immersed in the subphase.[19] Our studies on multiple compression / expansion cycles for PS-*b*-PEO(18.9%) cast from various spreading concentrations reveal that hysteresis in the brush regime increases significantly below a critical spreading concentration, while there is a corresponding decrease in hysteresis in the pancake regime. These results shed further light on a possible model for PS-*b*-PEO

aggregates at the air-water interface under different conditions of spreading concentration.

Another important issue addressed in this chapter is the mechanism of formation for the various surface aggregates of PS-*b*-PEO at the air-water interface -- an issue that has not been resolved in the literature. It was suggested that the various aggregates of PS-*b*-PEO described in Chapter 2 were "kinetically-locked" at different stages of evolution through polymer vitrification, but fundamental questions concerning the early stages of self-assembly remain. In this chapter, we expand on the morphological trends discussed in Chapter 2 and discuss some intriguing patterns that form under conditions of high spreading concentration and for the more hydrophobic copolymer—conditions which we believe represent an early "snapshot" in the process of aggregate formation. These results suggest that the genesis of aggregate formation involves dewetting of the evaporating solution of polymer in chloroform from the water surface, resulting in hole formation and leading to an eventual 2D network of interconnected rims; driven by an increase in PEO adsorption, this network then breaks down to form the range of observed surface morphologies.

3.2. Experimental Section

3.2.1. Materials

The polymers used in the present study were all obtained from Polymer Source Ltd. (Samples, and their corresponding catalog numbers; PS-*b*-PEO(11.4%), P119-SEO; PS-*b*-PEO(18.9%), P3597-SEO; PEO, P5055-EG2OH) and were characterized by the

manufacturer (Table 3.1) where M_n is the number average molecular weight, PI is the polydispersity index (M_w / M_n), and x_n is the respective degree of polymerization.

Table 3.1. Characteristics of the polymers used in this chapter

Polymer	M_n (g/mol)	PEO wt%	$P.I.$	$M_{n,PEO}$ (g/mol)	$M_{n,PS}$ (g/mol)	$x_{n,PEO}$	$x_{n,PS}$
PS-*b*-PEO(11.4%)	141100	11.4	1.04	16100	125000	370	1200
PS-*b*-PEO(18.9%)	185000	18.9	1.09	35000	150000	800	1440
PEO	30000	-	1.09	30000	-	680	-

A typical procedure involved the preparation of a ~ 5 mg/mL stock solution by weighing an appropriate amount of the polymer (dried overnight in a dark dessicator at room temperature) accurate to 0.1 mg (Sartorius analytical balance, CP224S) and gravitometrically diluting with glass-distilled, HPLC-grade chloroform (Sigma-Aldrich, 99.9+%) in new glassware that had been cleaned three times with acetone and three times with spectroscopic-grade chloroform (Aldrich, 99.8%). Spreading solutions of various concentrations were prepared by dilution from this stock solution; solutions were prepared 24 h prior to use to allow for equilibration and used within 2 days for isotherm trials and within 7 days for dipping studies. Prepared solutions were sealed with Teflon and refrigerated in the dark. Solid polymer samples was stored in a sealed vial covered in aluminum foil at -20 °C. These precautions were necessary to minimize the degradation of the PEO block via oxidation.[30]

3.2.2. Dynamic Light Scattering

Dynamic light scattering (DLS) experiments were carried out on a Brookhaven Instruments photon correlation spectrometer equipped with a BI-200SM goniometer, a BI-9000AT digital autocorrelator, and a Melles Griot He-Ne Laser (632.8 nm) with

maximum power output of 75 mW. As all light scattering techniques are ultrasensitive to dust impurities, great care was taken to eliminate contamination by dust. 5 mg/mL solutions were filtered through two 0.45 μm pore diameter Teflon filters (Target) into a scintillation vial (Brookhaven, 12 mL) that was cleaned three times with acetone, and vortexed (VWR Scientific, MV1) three times with spectroscopic grade chloroform. Spectroscopic grade chloroform was added to this vial through two 0.20 μm pore diameter Teflon filters (Target) to a final concentration of 2.0 mg/mL for analysis. Five replicate measurements of the autocorrelation function were obtained at 90° obtained in a refractive index matching medium (decalyn) regulated (Polyscience) at 23 °C. As was done in Chapter 2, DLS was performed to confirm that PS-*b*-PEO did not exist as micellar aggregates in chloroform before deposition.

3.2.3. Surface Pressure – Area Isotherms of Langmuir Films

Surface pressure-area (π- A) isotherms were obtained using a KSV 3000 Langmuir trough (KSV Instruments Ltd.) secured inside a dust shield. The total trough surface area was 150 × 515 mm^2 and total trough volume was ~1 L. The trough area was robotically controlled by two hydrophobic paddles which compressed the spread film symmetrically and bilaterally at a rate of 10 mm/min. House-distilled, deionized water (Barnstead NANOpure Diamond, 18.2 mΩ·cm) was used as the subphase in all trials. Prior to each trial, the water surface was cleaned by aspirating off any debris such that the surface pressure remained < 0.20 mN/m over a full compression. The LB components were cleaned daily with absolute ethanol before replacing the deionized water subphase. Surface pressure measurements were made from a roughened platinum Wilhemly place

(perimeter of 39.240 mm) which was flamed prior to each trial to ensure cleanliness. PS-*b*-PEO solutions in chloroform were spread on the subphase from a gastight Hamilton syringe. Spreading solution volumes depended on the concentration of the spreading solution and ranged from 10 to 1000 μL, so that a constant mass of copolymer was deposited for each trial unless otherwise stated. The spreading solution was deposited dropwise (~ 2 μL drop volume) at regularly spaced locations on the trough. In all trials, a 15 min evaporation period between the last deposited drop of solution and the beginning of compression ensured complete solvent evaporation.

One aspect of the present isotherm investigations is that the volume of solution deposited must proportionately increase with decreasing concentration to maintain a constant mass of deposited copolymer. This introduces an increased risk of contaminating the surface with impurities that may contribute to the isotherm. To examine this possibility, three trials using 1000 μL of pure 99.9+% chloroform (the same volume as the 0.10 mg/mL trial) were carried out. For the resulting compression isotherms, the observed surface pressure did not exceed 0.4 mN/m over a full compression, indicating that impurities from the largest solvent volumes employed do not contribute significantly to the isotherms.

3.2.4. Langmuir-Blodgett

Langmuir films were prepared as described above (Section 3.2.3) on the KSV 3000, except the volume of the spreading solution was exactly half. This was necessary to optimize the transfer ratio (1.1 ± 0.2), and independent AFM analysis confirmed that the volume deposited had no discernable influence on the surface morphologies. All

other parameters were identical to that of the $\pi - A$ section up to the transfer point, where the desired π was maintained for 10 minutes, followed by an upward transfer of a submerged substrate. Glass substrates (VWR Scientific 18 x 18mm^2) were cleaned first with methanol, sonicated (Branson 3510) in spectroscopic-grade chloroform (99.8%, Aldrich) for 20 min, dried, and used immediately. All transferred thin films were dried vertically for a minimum of 12 h and imaged within a week.

3.2.5. Atomic Force Microscopy

All AFM imaging was conducted on a Veeco (ThermoMicroscopes Explorer) instrument equipped with a Veeco tip (NanoProbe-MLCT-EXMT-A) run in contact mode. Tip velocity was typically maintained at 10 μm/s, and the resolution of each image was held at 500 scans/image. The AFM tips have a radius of < 50 nm, resulting in a maximum systematic error in lateral dimensions of < 20 nm (calculated on the basis of geometrical considerations of the tip and surface features); this error is within the standard deviations of feature widths reported in Table 3.1. To ensure that the friction of the tip did not perturb the surface features, a 10 μm × 10 μm area was imaged several times followed by a 20 μm × 20 μm scan of the same region; there was no obvious agitation of the observed aggregate structures from tip contact during the repeated scans. The AFM probe was housed within a vibration-resistant case on a vibration isolation platform maintained at 80 psi (Newport). Each sample was imaged several times at different locations on the substrate to ensure reproducibility. In all cases, the imaging of LB films was performed far from the edge of the glass substrate to minimize any local effects caused by turbulent water flow at the boundary and meniscus effects during

transfer. In some cases, brightness, contrast, and contour levels of AFM images were adjusted to improve clarity for presentation, however, statistical analysis was conducted on unmodified images.

3.3. Results and Discussion

The present work concerning PS-*b*-PEO(18.9%) builds on trends observed for the more hydrophobic PS-*b*-PEO(11.4%),[26] and is organized in a similar fashion to our previous chapter. We first consider compression isotherms as a function of spreading concentration for PS-*b*-PEO(18.9%), and then discuss the spreading concentration dependence of isotherm hysteresis effects. This is followed by a section describing the morphology of self-assembled aggregates of PS-*b*-PEO(18.9%) as a function of spreading solution concentration, including a comparison with the previously-described PS-*b*-PEO(11.4%), which formed ring and chain morphologies at sufficiently low spreading concentrations.[26] We finish with a discussion combining the salient points of the various experiments, including a possible mechanism of formation for various surface morphologies of relatively hydrophobic PS-*b*-PEO, involving dewetting of an evaporating copolymer solution from the water surface.

3.3.1. Surface Pressure – Area Isotherms

Qualitatively, the isotherm behaviour of PS-*b*-PEO Langmuir films formed via spontaneous self-assembly at the air-water interface is well understood.[15-22,24-26,31-35] The epiphilic PEO blocks preferentially adsorb to the water surface at low surface densities; however, upon compression of the film, an increase in surface pressure is observed in the

surface pressure-area ($\pi - A$) isotherms as the area available to the PEO segments is significantly reduced. Above a critical surface density, an exothermic desorption of the PEO into the water subphase occurs.[18-20,31-33,36] When the PEO blocks are sufficiently large relative to the hydrophobic PS blocks (i.e. copolymer compositions greater than ~ 15 wt% PEO),[24] this compression-induced desorption is characterized by a plateau, or pseudoplateau, in the isotherm, suggesting a first-order phase transition between an expanded PEO pancake phase and a more compact brush phase of desorbed PEO blocks anchored to the surface by the insoluble PS blocks. This phase transition generally occurs at a π of ~ 10 mN/m, with further compression of the film resulting in a continued sharp increase in π, which has been generally attributed to overlap of the insoluble PS blocks or the desorbed PEO brush. With two distinct regions of increasing π resolved from the isotherms, it is possible to determine two characteristic limiting mean molecular areas (A_0) corresponding to the pancake phase ($A_{0,p}$) and the more compressed brush phase ($A_{0,b}$) as described previously by Goncalves da Silva.[19]

In our previous chapter,[26] the large surface area of the PS blocks relative to the PEO blocks for the copolymer PS-*b*-PEO(11.4%) (Table 3.1) hindered the pancake-to-brush phase transition described in the previous paragraph, such that a plateau region and two distinct limiting areas were not observed. However, the single A_0 obtained from spreading solutions between 0.10 and 2.0 mg/mL showed a distinct spreading concentration dependence for the π- A isotherms and resultant A_0. We found that A_0 determined for Langmuir films of PS-*b*-PEO(11.4%) increased significantly for spreading concentrations below a critical value ($\leq$ 0.25 mg/mL), while for higher spreading concentrations ($\geq$ 0.50 mg/mL) the resultant A_0 values were all within 10 % of the area

occupied by a collapsed PS globule, as determined from the empirical relationship established by Kumaki;[37] $A_{0,PS} = 0.04MW_{PS}$ Å^2, where MW_{PS} is the average molecular weight of the PS blocks. The increase in A_0 for spreading solutions $\leq$ 0.25 mg/mL was attributed to increased adsorption of PEO segments during spreading and aggregate formation, facilitated by a decrease in PS entanglements.[26]

To gain further insight into the effect of spreading solution concentration on the conformation of PS and PEO blocks at different surface densities, we extended our previous investigation to look at the more hydrophilic PS-*b*-PEO(18.9%) (Table 3.1), above the 15 wt%-PEO threshold where a distinct plateau is generally observed;[24] this sample permitted analysis of the effect of spreading solution concentration on both the pancake and brush regions of the isotherm. Representative isotherms of Langmuir films cast from 0.10 and 0.50 mg/mL solutions of PS-*b*-PEO(18.9%) are shown in Figure 3.1, highlighting the general features of the spreading solution concentration dependence on the isothermal film behaviour. From the figure, we see that the limiting area of the pancake phase ($A_{0,p}$, inset) is the same for spreading solutions of 0.10 and 0.50 mg/mL, whereas the limiting area of the brush phase ($A_{0,b}$, inset) is significantly higher for the lower concentration of spreading solution (0.10 mg/mL). The earlier onset of the brush region for the lower spreading concentration results in a pseudoplateau at π of ~ 10 mN/m, compared to the plateau observed for the higher spreading concentration. The height of the plateau or pseudoplateau is found to be independent of the spreading concentration.

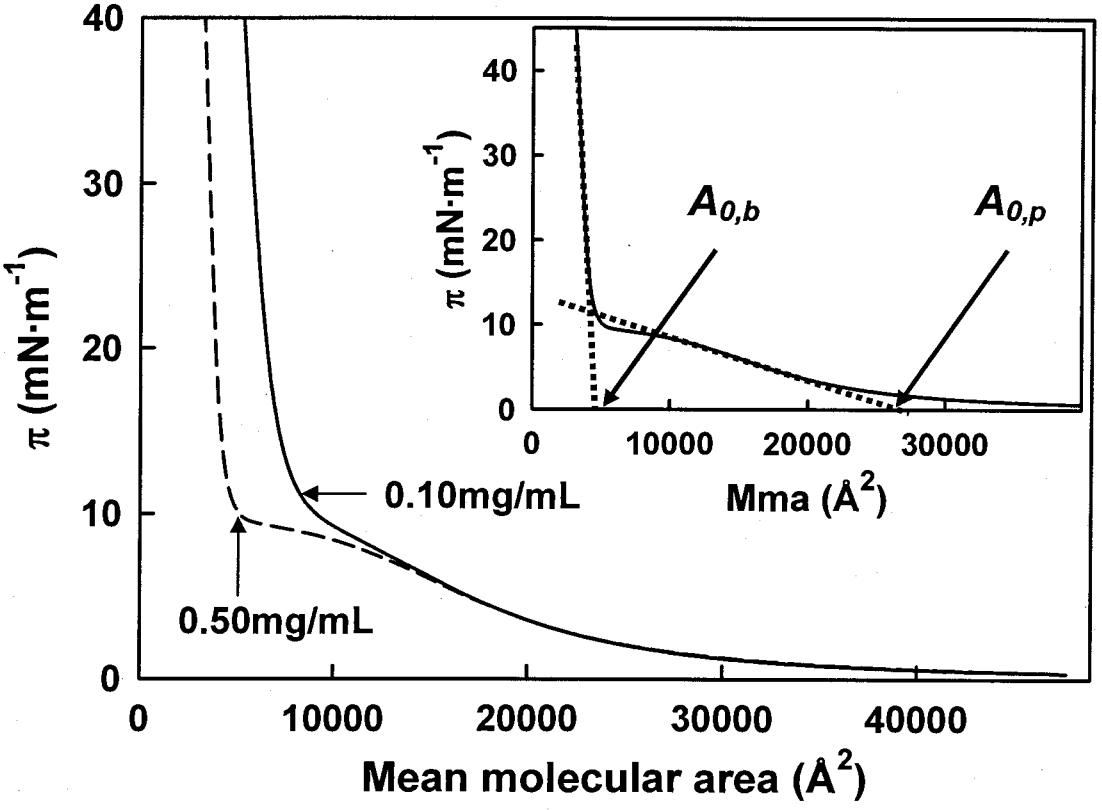

Figure 3.1. Representative π - A compression isotherms of PS-*b*-PEO(18.9%) spread from 0.50 and 0.10 mg/mL chloroform solutions at the air-water interface. Inset shows the extrapolation of the linear regions of the isotherm to $\pi = 0$ mN/m, used to obtain the limiting brush area ($A_{0,b}$) and limiting pancake area ($A_{0,p}$).

Figure 3.2a shows $A_{0,p}$ for PS-*b*-PEO(18.9%) plotted as a function of spreading solution concentration, clearly demonstrating that the limiting mean molecular area of the PEO pancake is independent of the spreading concentration. At low surface densities, a certain percentage of PEO blocks will extend radially from the periphery of the PS aggregates, adsorbed to the surface in the 2D pancake conformation; the constant mean molecular area of the PEO pancake for a range of spreading concentrations ($A_{0,p}$ of ~ 25000 Å^2) suggests that the average surface area occupied by these radial PEO blocks is unaffected by the concentration of spreading solution. This means that the number of pancaked PEO chains and their 2D conformation remain constant, or else the PEO conformation at the surface adjusts with any changes in the amount of adsorbed PEO, such that the average area per chain is constant. When we normalize the determined $A_{0,p}$ values with respect to the number of EO repeat units in the copolymer (Figure 3.2a), we obtain ~ 31 Å^2 per EO monomer over the range of spreading concentrations. From compression of PS-*b*-PEO monolayers, Goncalves da Silva[19] found $A_{0,p}$ to be between 27 and 31 Å^2, compared to $A_{0,p}$ between 28 and 30 Å^2 determined by Baker et al., with slightly higher $A_{0,p}$ determined for shorter PEO block lengths.[24] Our $A_{0,p}$ value of ~ 31 Å^2 is therefore consistent with what has been previously observed.

We also found that $A_{0,p}$ values determined for the PS-*b*-PEO(18.9%) copolymer are smaller than those determined for a "free" PEO homopolymer with molecular weight comparable to that of the PEO blocks (Figure 3.3). As with the PS-*b*-PEO(18.9%) copolymer, the PEO homopolymer showed no significant dependence of $A_{0,p}$ on spreading solution concentration. Various studies in the literature have reported a wide

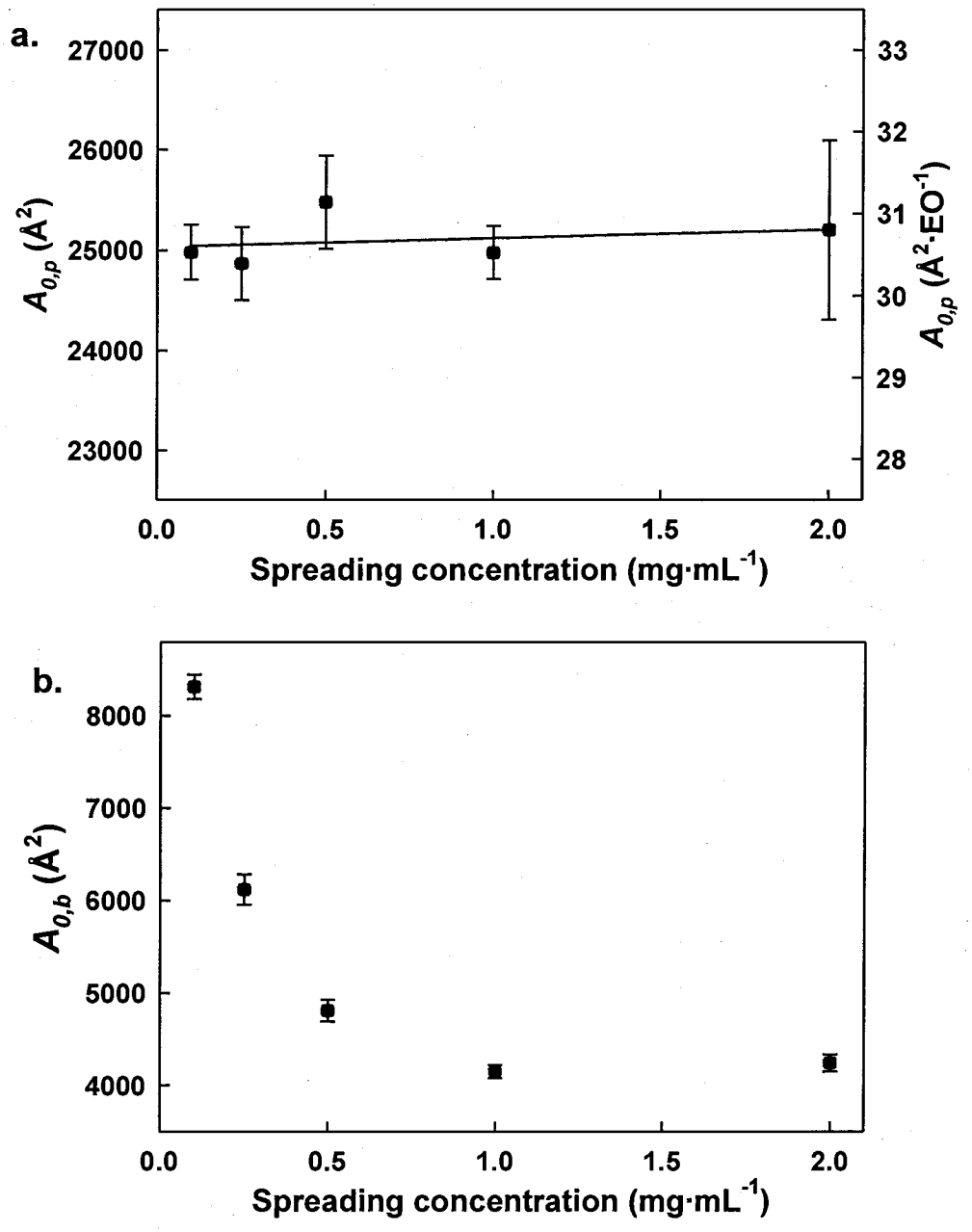

Figure 3.2. Limiting mean molecular areas of PS-*b*-PEO(18.9%) Langmuir films cast from given spreading concentration where (a) represents limiting pancake area ($A_{0,p}$) and (b) represents the limiting brush area ($A_{0,b}$). Error represents standard deviation of triplicate measurements

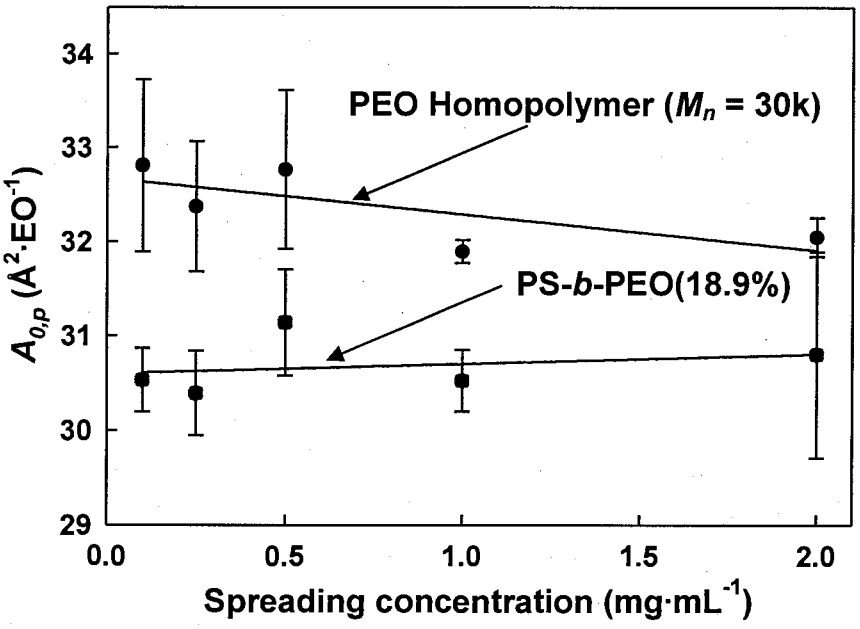

Figure 3.3. Limiting pancake areas of PS-*b*-PEO(18.9%) and a 30k PEO homopolymer deposited from given spreading concentrations and normalized to reflect the area per EO unit of the given Langmuir film. Error represents standard deviation of triplicate measurements

range of values for the area occupied per EO segment in PEO monolayers at the air-water interface, from 28 Å^2/EO,[28] for a 90k hydroxy terminated PEO homopolymer to ~ 40Å^2/EO[29] for a 252k homopolymer. The $A_{0,p}$ of our 30k PEO homopolymer was ~ 32Å^2/EO, closer to the value of the 90k sample determined by Shuler and Zisman,[28] reflecting an apparent molecular weight dependence on the area occupied per EO monomer. The somewhat lower $A_{0,p}$ values for the PS-*b*-PEO diblock compared to the corresponding PEO homopolymer (Figure 3.3) can be explained by a more compact pancake structure when PEO is tethered to the surface through a PS aggregate.[19] Another

factor is related to the possible presence of PEO underneath the PS aggregates in the diblock monolayers, as suggested by the model of Cox et al.;[16] repulsive PS-PEO interactions under the aggregates will result in a desorption of PEO monomers prior to compression, which should lower the average $A_{0,p}$ per monomer relative to the PEO homopolymer.

Despite constant $A_{0,p}$ values for different spreading concentrations, Figure 3.1 shows that there is a distinct concentration dependence on the onset of the brush region and corresponding $A_{0,b}$ values. Interestingly, the trend in $A_{0,b}$ with respect to spreading solution concentration determined for PS-*b*-PEO(18.9%) films (Figure 3.2b) shows a very similar trend to that reported previously for PS-*b*-PEO(11.4%).[26] Like A_0 determined for PS-*b*-PEO(11.4%), $A_{0,b}$ for the current sample is relatively constant for concentrations of the spreading solution $\geq$ 0.50 mg/mL, whereas below a critical spreading solution concentration ($\leq$ 0.25 mg/mL), $A_{0,b}$ increases significantly. In the previous chapter, it was suggested that the increase in A_0 was related to an increased surface adsorption of PEO monomers underneath the PS aggregates, facilitated by a decrease in PS entanglements;[26] a similar explanation is offered in the present case, as shown in the model presented in Figure 3.4. Spreading and evaporation of chloroform solutions of PS-*b*-PEO(18.9%) results in the formation of PS aggregates at the air-water interface, as in the case of PS-*b*-PEO(11.4%), although in the present case the larger PEO blocks result in a larger area occupied by PEO extending away from the aggregates in the pancake conformation, such that a pancake-to-brush transition is observed upon compression (Figure 3.1). In both PS-*b*-PEO(11.4%) and PS-*b*-PEO(18.9%) we suggest that a thin layer of PEO exists underneath the aggregates, as proposed by Cox et al;[16] unlike the pancake PEO extending

away from the aggregates, the conformation of PEO chains within this thin layer is dependent on the local PS density within the aggregates, which in turn depends on the extent of PS chain entanglements which restrict spreading of the copolymer during deposition and solvent evaporation. At higher spreading concentrations, the aggregates consist of a highly entangled dense PS brush, with the PEO chains underneath being significantly desorbed by strong repulsive PS-PEO interactions even before compression (Figure 3.4a). In contrast, at sufficiently low spreading concentrations, decreased PS entanglements allow for a less densely-packed PS brush structure within the aggregates and a consequential decrease in PS-PEO repulsion, so that the PEO underlayer consists of a significant amount of adsorbed PEO monomers (Figure 3.4b). Since the onset of the brush region corresponds to the overlap of the PS aggregates upon compression, the less densely-packed PS brushes obtained at lower spreading concentrations (Figure 3.4b) are reflected in the observed increase in the mean molecular area of the brush phase, $A_{0,b}$. As the area occupied by the PS aggregates increases with decreasing spreading concentration, the pancake-to-brush transition (Figure 3.4) of the external PEO chains becomes increasingly hindered by overlap of aggregates, as indicated by the observed decrease in the extent of the plateau region at lower spreading concentrations (Figure 3.1); the plateau is known to increase with PEO block length.[24] The less densely-packed aggregates obtained from spreading solutions of $\leq$ 0.25 mg/mL will increase the propensity for EO monomers in chains at the periphery of the aggregate to adsorb at the interface under the PS brush, effectively reducing the length of PEO chains radiating from the core that are accessible for the pancake-to-brush transition (Figure 3.4b); this results in the observed decrease in the plateau. We note that the critical spreading

concentration at which an increase in $A_{0,b}$ is observed ($\leq$ 0.25 mg/mL) is the same for the previous PS-*b*-PEO(11.4%) and current PS-*b*-PEO(18.9%) copolymers; this is consistent with increasing $A_{0,b}$ being related to decreasing PS chain entanglements, since the PS block lengths are similar in the two samples.[38] Clearly, the relative heights of the PS aggregates at different spreading concentrations is a critical aspect of the model presented in Figure 3.4, as will be discussed later in connection with AFM measurements LB films transferred from the air-water interface to glass.

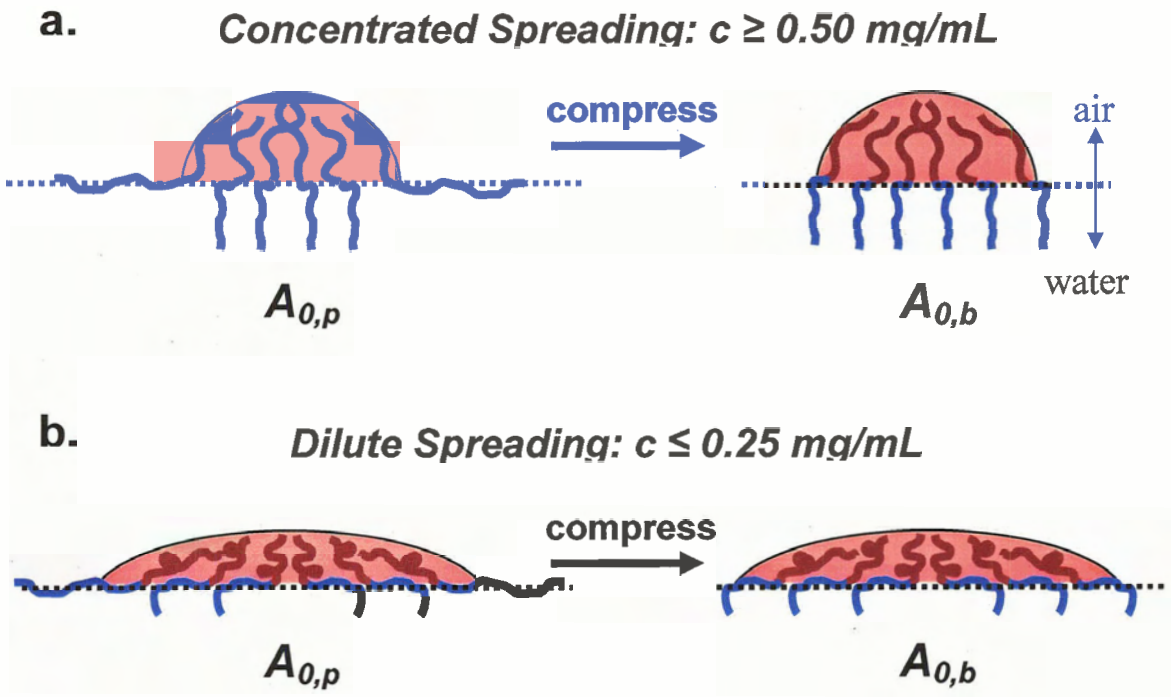

Figure 3.4. Schematic representation of the effect of spreading solution concentration on the relative locations of the PS and PEO blocks before (left) and after (right) compression, illustrating the pancake (*p*) – brush (*b*) phase transition. (a) More concentrated spreading solutions result in aggregates that have a greater extent of PEO desorbed under the PS aggregate with respect to dilute spreading solutions (b) where there is significant adsorption under the PS aggregate. Black dotted line indicates the location of the air-water interface

3.3.2. Hysteresis

The results discussed above pertain to the change in π with respect to the first continuous compression of a Langmuir film. A lack of superposition between a compression and subsequent expansion isotherm is termed hysteresis. Hysteresis effects can be monitored over several compression / expansion cycles, and have proved to be very informative in elucidating the dynamic behaviour of amphiphilic systems under variable stress at air-liquid [19-21,31,39-44] and liquid-liquid interfaces.[45]

It has been observed that PS-*b*-PEO copolymers at the air-water interface have compression isotherms that are significantly different from the subsequent expansion isotherms.[19,20,31] Goncalves da Silva et al.[19] have observed hysteresis in PS-*b*-PEO monolayers at both high and low π (brush and pancake regimes, respectively); through a series of compression / expansion isotherms on PS-*b*-PEO copolymers of variable PEO block length, the degree of hysteresis was shown to be dependent on the PEO block length and the temperature of the subphase. In that study, hysteresis in the brush regime, following compression of the monolayers to 35 mN/m, was attributed to cohesion and ordering of submerged helical PEO chains upon compression.[19] On the other hand, hysteresis in the pancake regime, following compression to just above 10 mN/m, was explained by a combination of three possible factors: i) PEO entanglement during the pancake-to-brush transition, ii) differences in the conformation of pancaked PEO following the first compression / expansion cycle, and iii) irreversible desorption of PEO homopolymer impurity.[19]

To our knowledge, an effect of spreading solution concentration on the hysteresis of PS-*b*-PEO monolayers has not been previously reported. We carried out a detailed

investigation of hysteresis effects for both PS-*b*-PEO(11.4%) and PS-b-PEO(18.9%) monolayers as a function of spreading solution concentration, and found remarkable spreading concentration dependences in both the brush and pancake regimes. Due to the presence of distinct pancake and brush phases from isotherms of PS-*b*-PEO(18.9%), hysteresis effects in both the pancake and brush regimes were quantified for that sample, whereas for PS-*b*-PEO(11.4%) the absence of a plateau in the isotherms meant that only the hysteresis of the brush regime could be determined.

The spreading concentration dependence on hysteresis in the brush regime (compression to π = 40 mN/m) for both PS-*b*-PEO(18.9%) and PS-*b*-PEO(11.4%) is demonstrated in Figure 3.5, which compares compression / expansion cycles for representative spreading concentrations of 0.10 mg/mL and 0.50 mg/mL. For both samples, the observed hysteresis is found to be dependent on the concentration of the spreading solution. This is illustrated by the minimum observed in the expansion isotherm for both samples cast from 0.10 mg/mL (Figure 3.5, insets), which was not observed when the same samples were cast from the higher spreading concentration (0.50 mg/mL). A similar minimum was previously observed in expansion isotherms obtained by Gonclaves da Silva et al. for PS-*b*-PEO monlayers expanded from 35 mN/m, and was found to be more pronounced for copolymer with shorter PEO blocks.[19] In agreement with the results of Goncalves da Silva, the minimum in the expansion isotherm of PS-*b*-PEO(11.4%) is much more pronounced (Figure 3.5b). These authors attributed the minimum to cohesion and local ordering between PEO chains in the brush conformation. In the present case, the unique concentration dependence of the minimum suggests that cohesion and organization of submerged PEO chains upon compression is favoured by

the less densely-packed PS aggregates obtained at lower spreading concentrations, where some of the PEO monomers under the aggregates are adsorbed to the water surface (Figure 3.4b). We note that in our model, the "dangling" submerged portion of PEO chains under the PS aggregates are shown to be shorter for lower spreading concentrations (Figure 3.4b) than for higher spreading concentrations (Figure 3.4a), and compression-induced cohesion favoured by this shorter PEO brush may be responsible for the spreading concentration dependence of the observed expansion minimum.

For the PS-*b*-PEO(18.9%) copolymer, hysteresis was quantified by calculating the difference $\Delta A_{0,b} = A_{0,b} - A'_{0,b}$, where $A'_{0,b}$ is the limiting brush area determined from the expansion isotherm following compression of the monolayer to π = 40 mN/m (Figure 3.5a). Similarly, hysteresis for the PS-*b*-PEO(11.4%) copolymer was calculated from $\Delta A_0 = A_0 - A'_0$, where A'_0 is the limiting area determined from the expansion isotherm following compression to π = 40 mN/m (Figure 3.5b). Interestingly, both ΔA_0 and $\Delta A_{0,b}$ determined from the first compression / expansion cycle of PS-*b*-PEO(11.4%) and PS-*b*-PEO(18.9%), respectively, showed a marked and similar dependence on the concentration of spreading solution (Figure 3.6). The observed trends in $\Delta A_{0,b}$ and ΔA_0 are found to match very well with the trends in $A_{0,b}$ (Figure 3.2a) and A_0 (Chapter 2),[26] with the observed hysteresis significantly increasing for monolayers cast from spreading solutions $\leq$ 0.25 mg/mL and remaining relatively constant for higher spreading concentrations ($\geq$ 0.50 mg/mL). The correspondence between increased hysteresis in the brush regime and increased mean molecular area of the brush phase again points to increased PEO cohesion upon compression of the less densely-packed aggregates obtained at spreading concentrations $\leq$ 0.25 mg/mL.

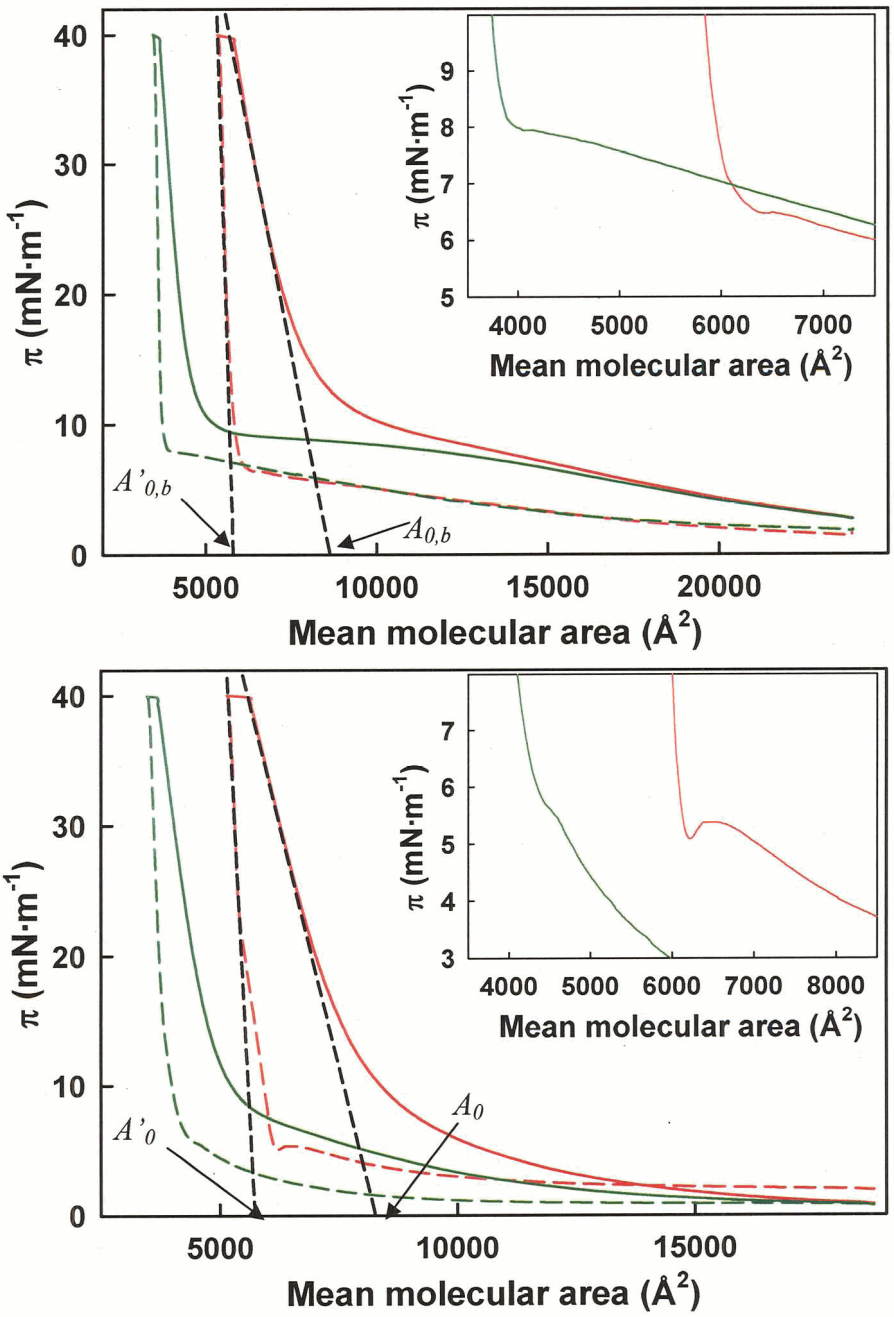

Figure 3.5. First compression (solid line) / expansion (dashed line) cycle of (a) PS-*b*-PEO(18.9%) and (b) PS-*b*-PEO(11.4%) Langmuir films deposited from 0.10 mg/mL (red) and 0.50 mg/mL (green) solutions. Extrapolated tangents show the limiting mean molecular area obtained on compression (A_0) and expansion (A'_0) used for the determination of the hysteresis. Inset represents a magnified view of the first expansion cycle of the respective Langmuir film highlighting the apparent minima observed for Langmuir films cast from 0.10 mg/mL spreading solutions.

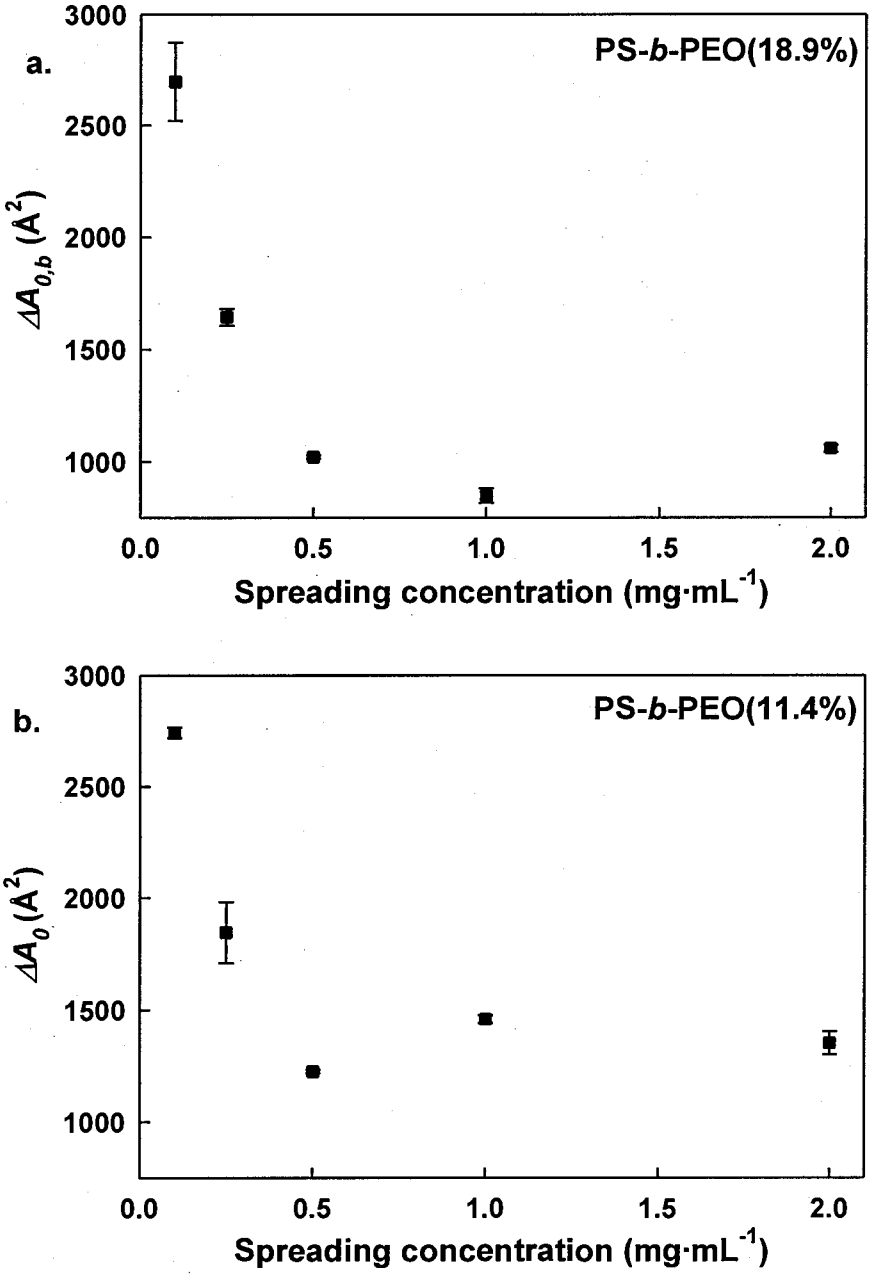

Figure 3.6. Isothermal hysteresis in the brush regime ($\Delta A_{0(,b)}$) of (a) PS-*b*-PEO(18.9%) and (b) PS-*b*-PEO(11.4%) Langmuir films deposited from given spreading concentration. $\Delta A_{0(,b)}$ was calculated as the difference in limiting mean molecular area obtained on expansion from compression to 40 mN/m (i.e., $\Delta A_{0(,b)} = A_{0(,b)} - A'_{0(,b)}$) as defined in Figure 3.6. Error bars represent the difference between duplicate measurements

Hysteresis in the pancake regime (compression to $\pi = 10$ mN/m, just above the plateau region) for PS-*b*-PEO(18.9%) was also found to show a clear concentration dependence, as shown by compression / expansion cycles for representative spreading concentrations of 0.25mg/mL and 0.50mg/mL (Figure 3.7). Similar to $\Delta A_{0,b}$, $\Delta A_{0,p}$ was calculated from compression / expansion cycles obtained for a range of spreading concentrations, and used quantify the spreading concentration dependence of hysteresis in the pancake regime (Figure 3.8). Interestingly, the concentration dependence of $\Delta A_{o,p}$ is the opposite to that of $\Delta A_{0,b}$, with the extent of hysteresis *decreasing* for monolayers cast from spreading solutions ≤ 0.25 mg/mL and remaining constant for higher spreading concentrations (≥ 0.50 mg/mL). We note that the decrease in hysteresis shown in Figure 3.8 corresponds to the decrease in the extent of the plateau region as the spreading concentration decreases (Figure 3.1), which is due to the pancake-to-brush transition being increasingly hindered by overlap of PS aggregates of increasing mean molecular area (Figure 3.4). Therefore, the observed decrease in hysteresis can be explained by a decrease in the number of chains that are able to undergo a pancake-to-brush transition upon compression as the spreading concentration decreases. These results appear to confirm that hysteresis at low π is at least partially due to PEO chain entanglements or conformational changes arising from the first-order phase transition.

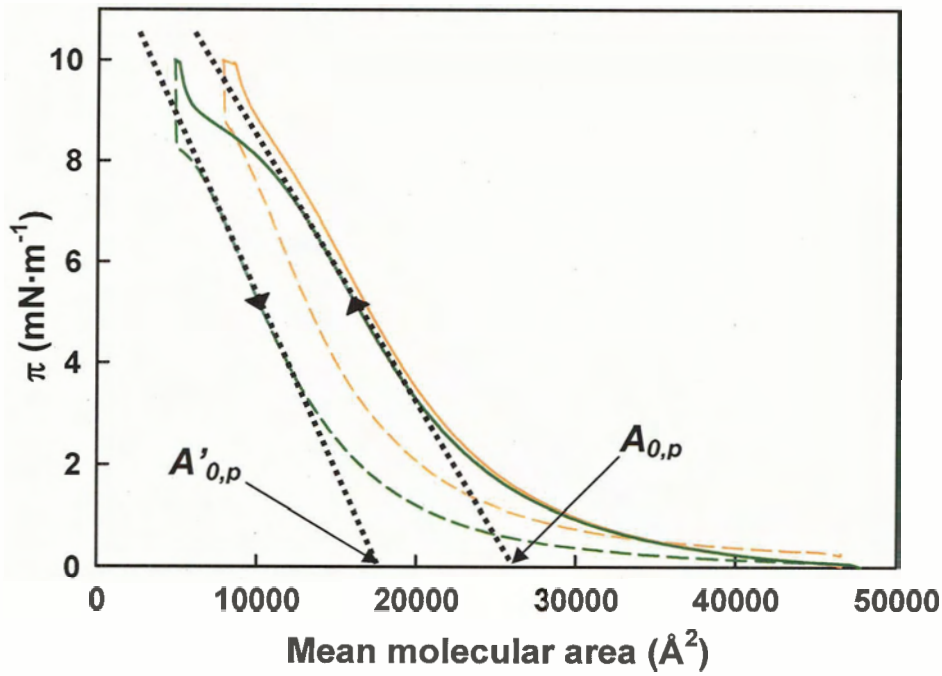

Figure 3.7. First compression (solid line) / expansion (dashed line) cycle to π = 10mN/m of a PS-*b*-PEO(18.9%) Langmuir film deposited from 0.25 mg/mL (orange) and 0.50 mg/mL (green) solutions. Extrapolated tangents show the limiting mean molecular areas in the pancake regime obtained on compression ($A_{0,p}$) and expansion ($A'_{0,p}$) used for the determination of the hysteresis.

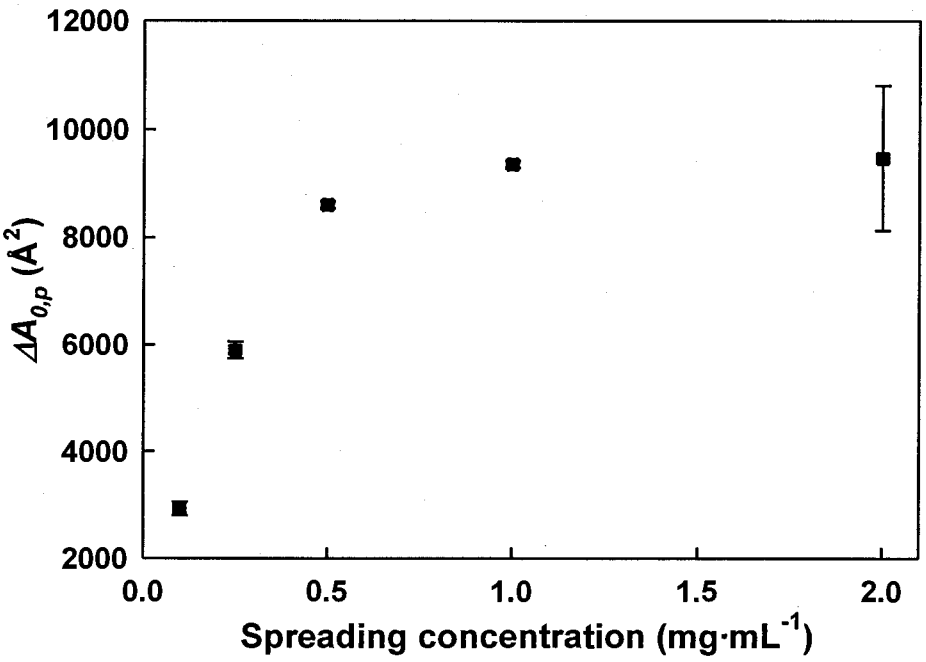

Figure 3.8. Isothermal hysteresis in the pancake regime ($\Delta A_{0,p}$) of PS-*b*-PEO(18.9%) Langmuir films deposited from given spreading concentration. $\Delta A_{0,p}$ was calculated as the difference in limiting mean molecular area obtained on expansion from compression to 10 mN/m (i.e., $\Delta A_{0,p} = A_{0,p} - A'_{0,p}$) as defined in Figure 3.7. Error bars represent the difference between duplicate measurements

Multiple compression / expansion cycles have been shown to provide some additional information pertaining to the dynamics of amphiphilic molecules at water surfaces.[19] Subsequent cycles performed faster than the relaxation time needed for the system to return to its state prior to the first compression can be reflected in a decrease in hysteresis with successive cycles. For hysteresis in the brush regime, Figure 3.9 demonstrates the general trend that $\Delta A_{0,b}$ and ΔA_0 decreases significantly from the first to the second cycle and remains relatively unchanged with subsequent cycles. This suggests that upon the first compression to $\pi = 40$ mN/m, the compression-induced cohesion and ordering between submerged PEO chains remains intact on the time scale of the subsequent compression / expansion cycles. We also note that the largest decreases in hysteresis between the first and second cycles are observed for 0.10 and 0.25 mg/mL in both PS-*b*-PEO copolymers, reflecting a greater extent of irreversible PEO cohesion from compression of the less densely-packed PS aggregates, as discussed previously. Irreversible cohesion of PEO chains following the first compression, especially for films deposited at spreading concentrations of 0.10 and 0.25 mg/mL, is also reflected in a much lower compressibility determined from subsequent compression isotherms (not shown). The increase in $\Delta A_{0,b}$ from the first to second cycle observed for PS-*b*-PEO(18.9%) cast from spreading solutions $\geq$ 0.50 mg/mL does not follow the general trend of decreasing hysteresis over multiple cycles; this interesting behaviour is entirely reproducible and observed for three different spreading solutions of PS-*b*-PEO(18.9%), although at present it is not understood.

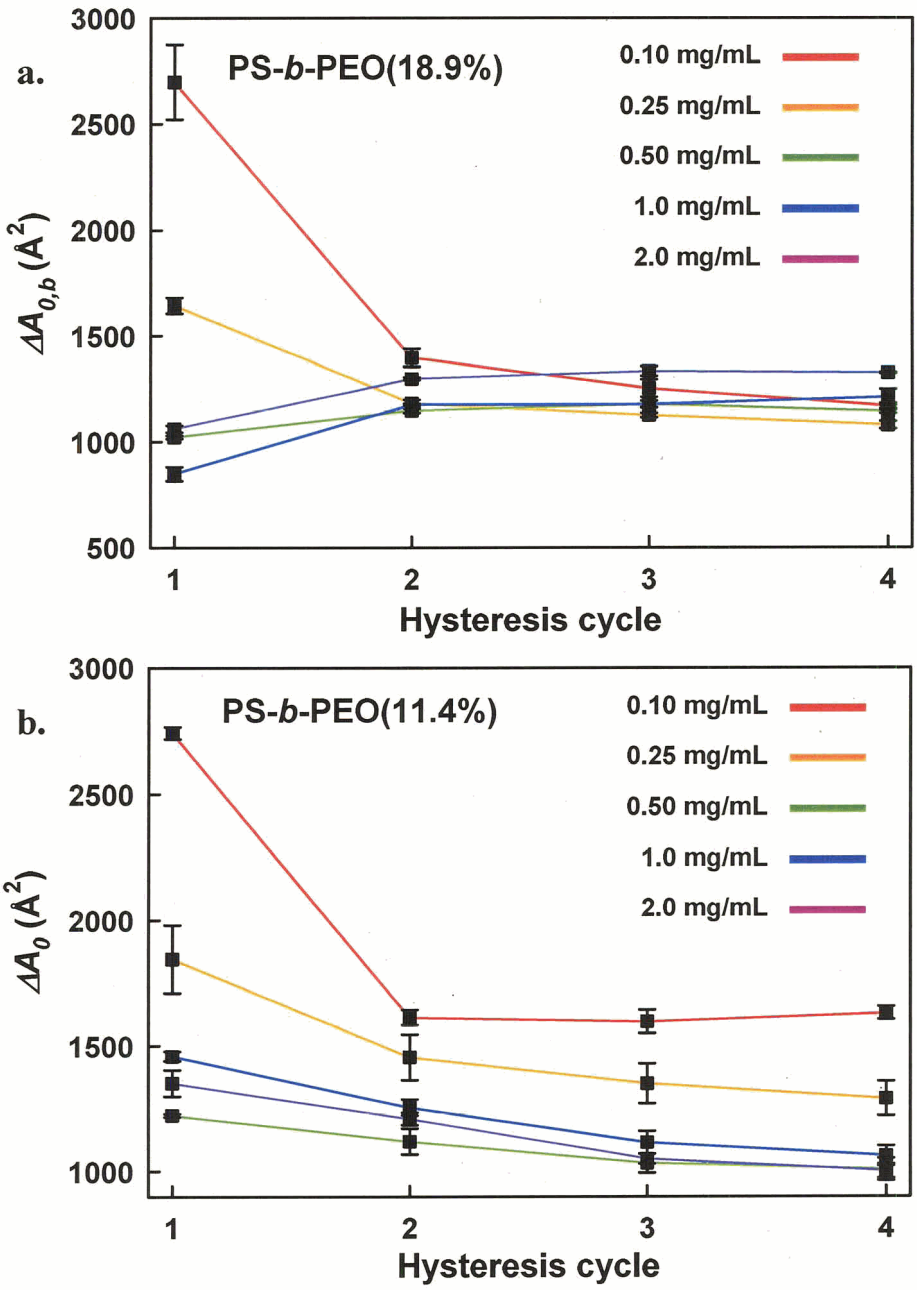

Figure 3.9. Isothermal hysteresis in the brush regime for (a) PS-*b*-PEO(18.9%) and (b) PS-*b*-PEO(11.4%) obtained from multiple compression / expansion cycles on the respective Langmuir films deposited from spreading solutions of 0.10mg/mL (red), 0.25mg/mL (orange), 0.50mg/mL (green), 1.0mg/mL (blue), and 2.0mg/mL (violet) determined as the difference in limiting mean molecular obtained on the given expansion ($A'_{0(,b)}$) from that obtained on given compression ($A_{0(,b)}$) to π = 10mN/m, (i.e. $\Delta A_{0(,b)} = A_{0(,b)} - A'_{0(,b)}$). Error bars represent the difference between duplicate measurements

We also performed multiple compression / expansion cycles in the pancake regime (Figure 3.10) (i.e. compressions to π = 10 mN/m) for a range of spreading solution concentrations. Consistent with literature reports and similar to hysteresis in the brush regime,[19] $\Delta A_{0,p}$ decreases after the first cycle for all spreading concentrations. Unlike ΔA_0 and $\Delta A_{0,b}$ for lower spreading concentrations, $\Delta A_{0,p}$ continues to decrease with each successive cycle for all spreading concentrations. This is explained by a cumulative increase in PEO chain entanglements with each successive compression / expansion cycle in the pancake regime, compared to the cohesive organization of PEO chains in the brush regime, which occurs mainly during the first compression to high pressure. Figure 3.10 shows that chain entanglement with each compression, resulting in a lowering of the observed hysteresis in the subsequent cycle, is greater for higher spreading concentrations. As an interesting consequence, we find that $\Delta A_{0,p}$ converges to ~2000 Å^2 after four compression / expansion cycles for all concentrations of the spreading solution, despite very different hysteresis effects in the first cycle. This suggests that after a sufficient number of cycles, a constant amount of surface-adsorbed PEO is eventually available for the first-order phase transition, irrespective of spreading concentration and the initial, uncompressed state of the monolayer. A decrease in surface-adsorbed PEO with successive compression / expansion cycles is also supported by an observed decrease in the extent of the compression isotherm plateau with repeated compression / expansion of PS-*b*-PEO(18.9%) monolayers deposited from the more concentrated spreading solutions (not shown).

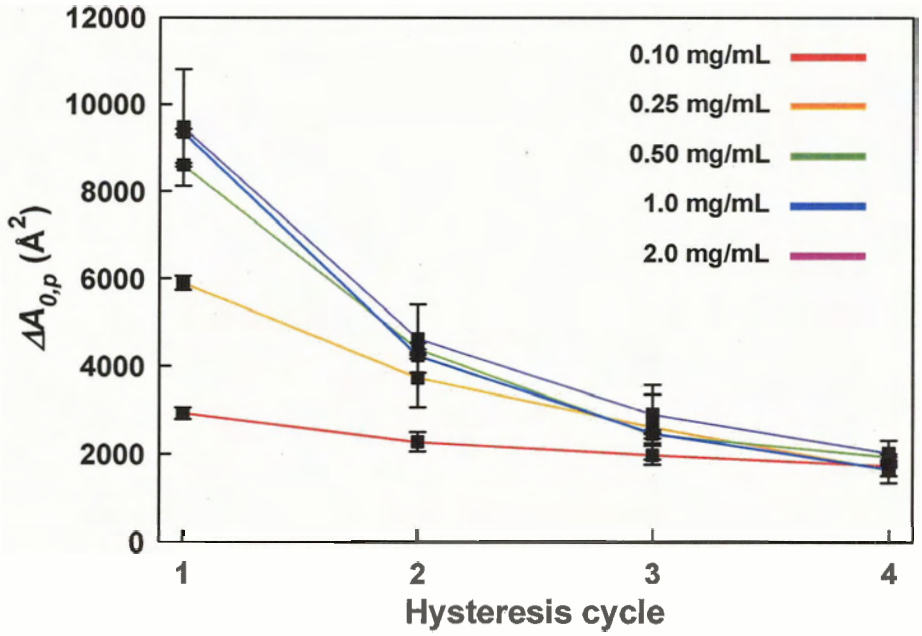

Figure 3.10. Isothermal hysteresis in the pancake regime for PS-*b*-PEO(18.9%) obtained from multiple compression / expansion cycles on the respective Langmuir films deposited from spreading solution of 0.10mg/mL (red), 0.25mg/mL (orange), 0.50mg/mL (green), 1.0mg/mL (blue), and 2.0mg/mL (violet) determined as the difference in limiting mean molecular obtained on the given expansion ($A'_{0,p}$) from that obtained on given compression ($A_{0,p}$) to π = 10mN/m, (i.e. $\Delta A_{0,p} = A_{0,p} - A'_{0,p}$). Error bars represent the difference between duplicate measurements

3.3.3. Atomic Force Microscopy

The compression isotherm and hysteresis data for PS-*b*-PEO(11.4%) and PS-*b*-PEO(18.9%) presented in the previous section and in the previous chapter strongly suggest that below a critical spreading concentration, the PS aggregates which form at the water surface become less densely-packed, with an increase in PEO adsorption in the PEO underlayer, as presented in the model in Figure 3.4. This is explained by a relaxation of PS chain entanglements, which at higher spreading concentrations restrict the thermodynamically-favourable spreading of the PS-*b*-PEO brush. In this section, as in the previous chapter for PS-*b*-PEO(11.4%), we use atomic force microscopy (AFM) to characterize the topology of the kinetically-"locked" structures of the more hydrophilic PS-b-PEO(18.9%) after transfer to a glass substrate, in order to determine how chain entanglements during spreading and solvent evaporation effect the heights and lateral morphology of the PS aggregates.

In the previous chapter, it was shown that lateral morphologies of PS-*b*-PEO(11.4%) were strongly affected by the spreading concentration. For comparison with the more hydrophilic PS-*b*-PEO(18.9%), the results obtained for PS-*b*-PEO(11.4%) are summarized in Figure 3.11, which shows primarily dots and spaghetti morphologies at spreading concentrations of 1.0 and 0.75 mg/mL, "budding" spaghetti at 0.50 mg/mL, and a predominance of unique rings and chains at 0.25 mg/mL. These morphology transformations were explained by different kinetic states "frozen in" by solvent evaporation, with structures existing closer to equilibrium as PS chain entanglements are decreased in the presence of solvent by lower spreading concentrations. Based on the observed structures in Figure 3.11, the formation of chains is believed to evolve from

initial spaghetti structures, which first develop dimples ("budding" spaghetti; inset, Figure 3.11c), and then holes along the length of the aggregates; in some cases, rings appear to break away from the chains. As well, it was observed that the chain and ring aggregates were statistically lower than the spaghetti and dots, supporting the isotherm data which indicates that PS chains in aggregates obtained below a critical spreading concentration are less densely-packed (Figure 3.4). Importantly, the appearance of rings and chains in the AFM images for spreading concentrations ≤ 0.25 mg/mL corresponded exactly to an increase in the mean molecular area by isotherm measurements. From the combination of AFM and isotherm data, it was concluded that the driving force for hole formation along the length of the spaghetti aggregates (forming chains), and for an overall lowering of the aggregate density, is a favourable increase in surface adsorption of PEO. Holes within chains should provide a region of zero local PS density within the aggregates in which PEO chains can become adsorbed; as well, an overall lowering of PS density within the brush structure should promote surface adsorption of some PEO monomers underneath the aggregates, as portrayed in Figure 3.4b.

The spreading concentration dependence of aggregate morphology for the more hydrophilic PS-*b*-PEO(18.9%) is shown in Figure 3.12, with a mixture of spaghetti, dots and small irregular aggregates (circled in Figure 3.12d) obtained from all spreading solutions (2.0, 1.0, 0.50, 0.25 mg/mL). In the present case, the spreading concentration dependence on morphology was less dramatic than for PS-*b*-PEO(11.4%), although it was found that spaghetti aggregates were observed more frequently when PS-*b*-PEO(18.9%) was cast from more concentrated solutions (e.g. 2.0 mg/mL, Figure 3.12a), with dots and the small irregular aggregates predominating in the dilute regime (e.g. 0.25

mg/mL, Figure 3.12d). Unlike PS-*b*-PEO(11.4%), no chain or ring structures were observed from PS-*b*-PEO(18.9%) for any of the spreading concentrations studied. The dimensions of the various surface features for PS-*b*-PEO(18.9%) were determined through AFM, and were compared to the dimensions of PS-*b*-PEO(11.4%) features described in the previous chapter (Table 3.2): we note that widths of dot and spaghetti features are similar for both samples (~160-180 nm), although the dots and spaghetti obtained from PS-*b*-PEO(18.9%) are somewhat taller than those formed from PS-*b*-PEO(11.4%). Importantly, the small irregular aggregates, which were most commonly observed for the lower spreading concentrations ($\leq$ 0.25 mg/mL), are significantly shorter than either the dots or spaghetti aggregates (Table 3.2), suggesting a less dense brush structure within these features. This observation of an increased number of lower aggregates correlates well with the increase in $A_{0,b}$ for spreading solutions $\leq$ 0.25 mg/mL (described previously). Unfortunately, it is extremely difficult to determine from AFM the average area fraction occupied by the aggregates under different spreading conditions, due to the non-uniform nature of these films and the mixture of morphologies observed; this calculation, of course, would allow the $A_{0,b}$ determined from the isotherm experiments to be verified. However, analysis of the occurrence and heights of the various features provides an indirect comparison between the AFM and isotherm data.

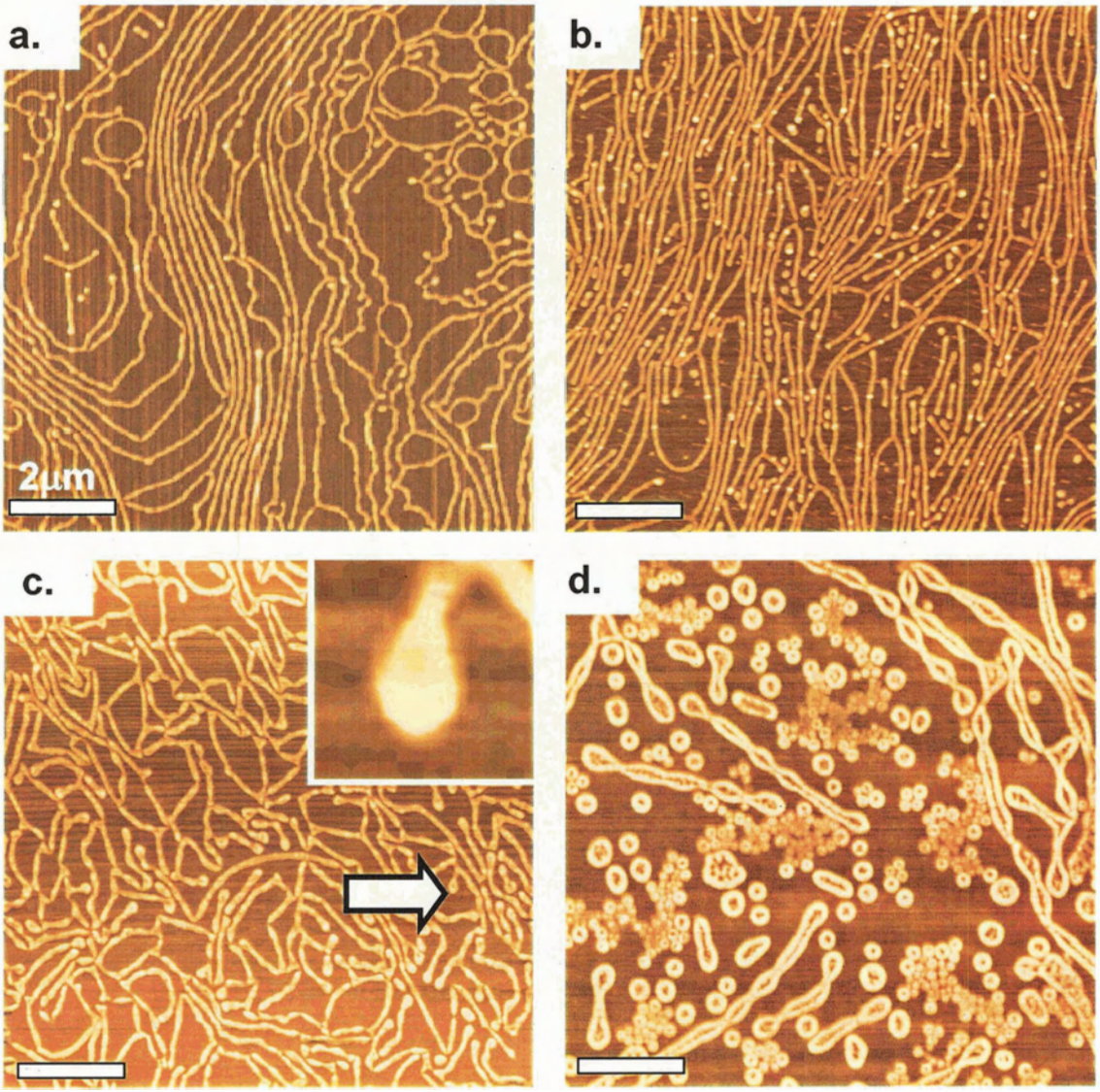

Figure 3.11. Representative AFM images of PS-*b*-PEO(11.4%) Langmuir films deposited from chloroform solutions at the air-water interface. All film transfers occurred via the Blodgett method at a constant π of 2.0 mN/m. Spreading solution concentrations were a) 1.0mg/mL, b) 0.75mg/mL, c) 0.50mg/mL, and d) 0.25mg/mL. Scale bar represents 2 μm. Inset in c) is a magnified version of a "budding spaghetti" highlighted by the arrow, inset edge length is 500 nm

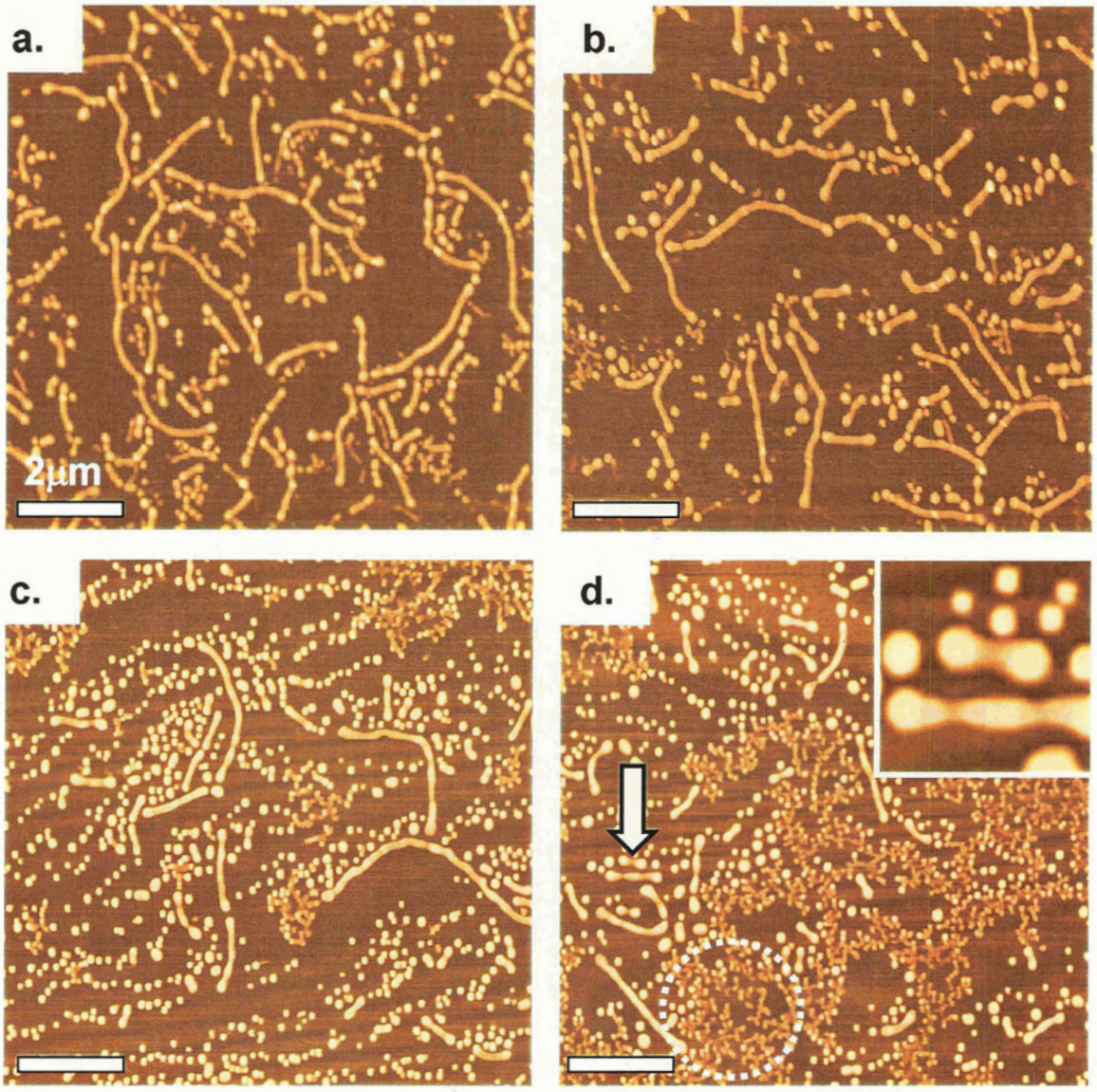

Figure 3.12. Representative AFM images of PS-*b*-PEO(18.9%) Langmuir films deposited from chloroform solutions at the air-water interface. All film transfers occurred via the Blodgett method at a constant π of 5.0mN/m. Spreading solution concentrations were a) 2.0mg/mL, b) 1.0mg/mL, c) 0.50mg/mL, and d) 0.25mg/mL. Scale bar represents 2μm. Inset in d) is a magnified version of a dots "pinching" from spaghetti aggregates highlighted by the arrow, inset edge length is 500nm. Circled region in d) highlights the smaller irregular aggregates described in the text.

Table 3.2. Mean dimensions of PS-*b*-PEO surface features observed through AFM

	PS-*b*-PEO(18.9%)			PS-*b*-PEO(11.4%)		
	dots	spaghetti	irreg. aggs.	dots	spaghetti	ring/chains
height (nm)	20 ± 2	15 ± 2	10 ± 3	16 ± 2	12 ± 2	10 ± 2
width (nm)	180 ± 40	170 ± 20	110 ± 20	170 ± 30	160 ± 20	170 ± 20
N	426	292	75	100	100	200

* error represents the standard deviation of n surface features
* there was no statistical concentration dependence on the dimensions of the given surface feature
* N represents number of individual surface features used in the statistical analysis

Similar to the situation described for PS-*b*-PEO(11.4%), the spreading concentration dependence of surface features in PS-*b*-PEO(18.9%) can be understood as a series of "frozen" kinetic states approaching closer to a lowest-energy state as chain entanglements are reduced in the presence of solvent. However, for the more hydrophilic sample, it appears that the transition from spaghetti to budding spaghetti to chains and rings does not occur, since chains and rings are not observed in any films of PS-*b*-PEO(18.9%), even for the lowest spreading concentrations. Rather, the predominant morphology transformation in this system appears to be the break-up of spaghetti into dots, as suggested both by the increase in the number of dots at the lowest spreading concentrations (Figure 3.12), and also AFM evidence of dots "pinching" from spaghetti aggregates for a spreading concentration of 0.25 mg/mL (Figure 3.12d, inset). This transition from spaghetti to dots will increase the contact line of the aggregates, allowing submerged PEO under the spaghetti structures to become adsorbed at the periphery of the forming dots; this does not appear to have a significant effect on the total area occupied by the pancake PEO surrounding the aggregates, however, since the observed critical pancake areas $A_{0,p}$ were unaffected by spreading concentration. Perhaps more important is the formation of the small irregular aggregates, which may result from further break-up

of dots; since these aggregates are significantly lower than dots, their formation appears to be driven by a lowering of brush density and a consequential increase in PEO adsorption underneath the aggregates, as supported by an increase in $A_{0,b}$ at lower spreading concentrations. One possibility is that these small irregular aggregates represent an attempt of the system to spread into a uniform monolayer of PS-*b*-PEO consisting of individual collapsed PS globules and adsorbed PEO chains, although this cannot be confirmed by the present data. We note that the pinching of dots from spaghetti structures as the solvent evaporates also appears to be operative in the PS-*b*-PEO(11.4%) sample, since an increase in the number of dots relative to spaghetti in that sample was also observed as the solvent concentration decreased. It can be speculated that in PS-*b*-PEO(11.4%), slower spreading than in PS-*b*-PEO(18.9%) due to the more hydrophobic character of the former results in longer and more numerous spaghetti aggregates in a late stage of solvent evaporation, where chain mobility is quite restricted; as a result, the system attempts to minimize its energy by the formation of chains from spaghetti, as previously described, a process which may require less lateral movement of chains than the pinching of dots from spaghetti.

3.3.4. Mechanism of Surface Pattern Formation

We have already shown how for two relatively hydrophobic PS-*b*-PEO monolayers, spaghetti aggregates will transform into either chains and rings or dots in order to maximize PEO adsorption, given sufficient mobility before "freezing in" by solvent evaporation. The result is an interesting spreading concentration dependence of the observed morphology, since higher degrees of chain entanglements result in slower

chain mobility and therefore earlier "snapshots" in the process of surface feature evolution. An interesting question that arises from the above discussion is the following: if dots, chains, and other morphologies evolve from spaghetti-like aggregates, how do the spaghetti form? They are clearly not equilibrium structures, since given the chance they will break down into more energetically favourable aggregates.[25,26]

An important clue to spaghetti formation, and therefore morphological genesis in these monolayers, comes from AFM images of LB films of the more hydrophobic diblock, PS-*b*-PEO(11.4%), obtained at a very high spreading concentration of 2.0 mg/mL (greater than the highest spreading concentration of 1.0 mg/mL reported in Figure 3.11). This more slowly spreading of the two copolymers, spread under conditions of extreme chain entanglements, provides a very early snapshot of the copolymer film after depositing from chloroform onto the surface of water. A typical region of this film is shown in the AFM images in Figure 3.13. In the low-magnification image (Figure 3.13a), a large number of long and interconnected spaghetti aggregates, in addition to a region in the lower right-hand side of the image which is best described as a cellular network (featured in the magnified image in Figure 3.13b). Though impossible to confirm from static images, this and other AFM images of the same film strongly suggest that the connectivity of the cellular networks break down to form long spaghetti structures from the network walls. The inset to Figure 3.13a shows a region where a portion of the network has broken away to form a large chain (on a much larger length scale than the chains observed for the same sample at low spreading concentrations), and beside the chain is a long spaghetti aggregate; a topographic line profile of the region (Figure 3.13c)

reveals that the heights and widths the "broken" network walls and the spaghetti are nearly identical.

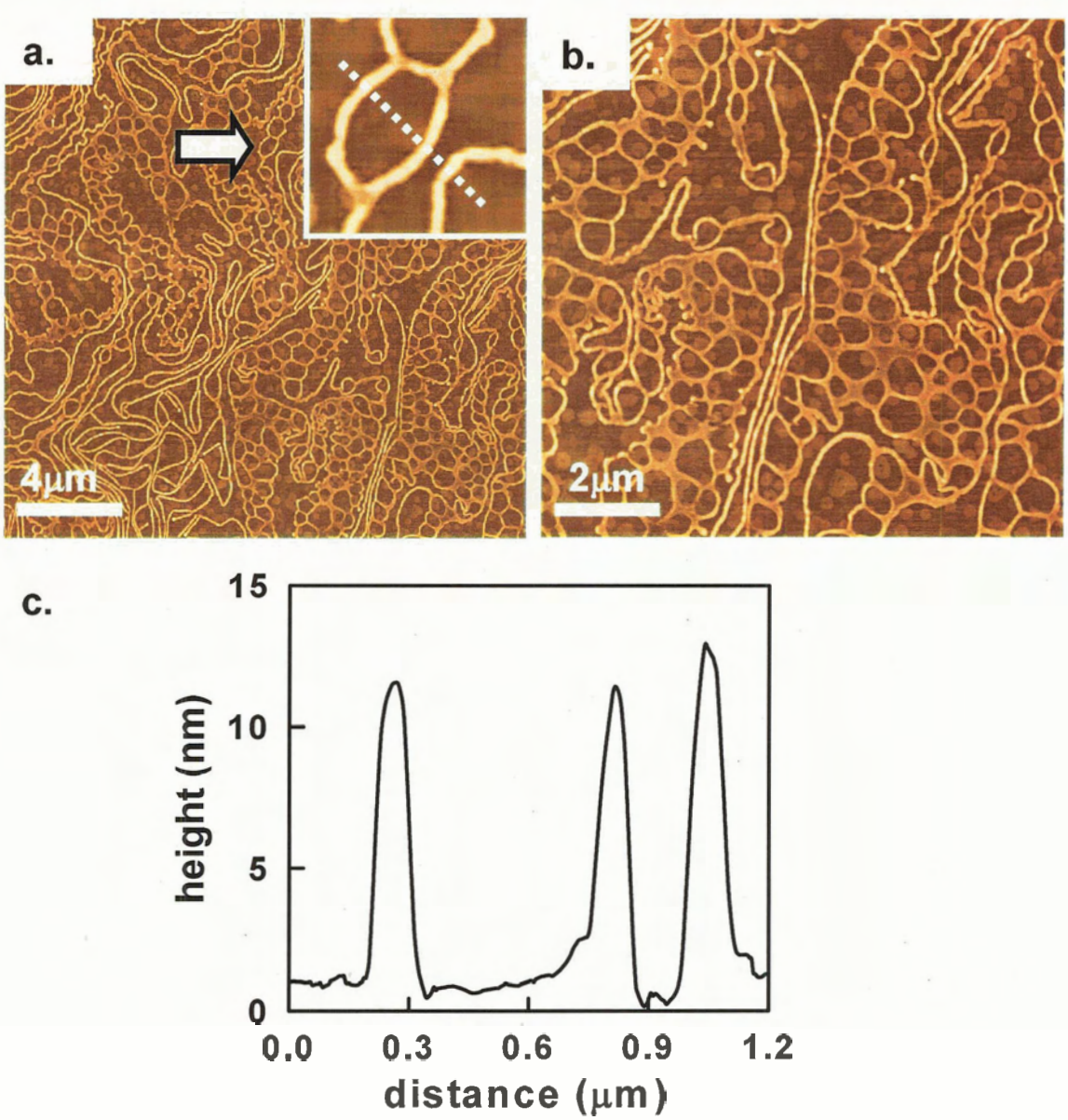

Figure 3.13. (a) Low magnification AFM image of a PS-*b*-PEO(11.4%) Langmuir film deposited from 2.0 mg/mL chloroform solutions at the air-water interface demonstrating the 'cellular' network described in the text. (b) is a magnified image of the lower right quadrant of (a) highlighting the 'cellular' pattern. (c) is a topological profile of the inset in (a). All film transfers occurred via the Blodgett method at a constant π of 2.0mN/m.

The two-dimensional network structures found in many regions of this film are strongly reminiscent of patterns formed from dewetting of ultrathin films of PS homopolymer from solid surfaces, either after dip-coating from an organic solvent[46] or in the molten state.[47,48] Considering the obvious similarities, it is reasonable to suggest that dewetting plays a formative role in the development of the various surface aggregates formed from these, and perhaps other, amphiphilic block copolymers at the air-water interface. We propose that morphology evolution in films of hydrophobic PS-*b*-PEO begins with a continuous and homogenous layer of chloroform and the hydrophobic diblock at the water surface (Figure 3.14a), stabilized by the positive spreading coefficient of chloroform on water. As chloroform evaporation occurs, the short-range interactions between the film and water become increasingly less attractive, and the film eventually dewets, with holes developing in the copolymer / chloroform film (Figure 3.14b, side view and c, top view). Hole formation in the unstable film can occur either through a nucleation process stemming from heterogeneities in the film[49] or through spontaneous film thickness fluctuations caused by capillary waves that amplify and propagate through the layer.[50] The resultant holes, surrounded by raised rims of transferred material, grow due to an interfacial tension gradient between the dewetting layer and the interface,[47,48] until contact with adjacent expanding holes results in a network of interconnected rims (Figure 3.14d). In Figure 3.13b, some regions of the network are shorter than structures highlighted in the inset, suggesting an earlier stage in the dewetting mechanism before sufficient material has accumulated in the expanding rim. In more typical dewetting processes involving homopolymers on solid surfaces, interconnected rims will next break down into droplets via Rayleigh instabilities.[51]

However, the present case is obviously complicated by favourable interactions between PEO blocks and the water surface, such that the cellular network (Figure 3.14e) first breaks into long spaghetti aggregates (Figure 3.14f), which then form either into dots, chains, and rings (in the case of PS-*b*-PEO(11.4%)), or dots (in the case of PS-*b*-PEO(18.9%)) (Figure 3.14g).

Finally, we point out that the above dewetting mechanism of pattern formation in hydrophobic PS-*b*-PEO monolayers can also explain the existence of the large continent structures previously observed in similar systems.[17,25] From the discussion above, it appears that continents are simply extended regions of the original continuous film, which become frozen by solvent evaporation before undergoing dewetting, or before being subsumed by an advancing rim. In fact, although we did not observe large continents from either of our samples at any of the studied spreading concentrations, the homogenous regions between the network rims in Figure 3.13b suggest smaller versions of the continents shown by Baker et al.,[25] which relatively low, flat aggregates surrounded by a raised rim.

We point out that a mechanism of surface aggregate formation involving the breakdown of an initial dewetting pattern emphasizes the fundamental differences between diblock copolymer amphiphile self-assembly in aqueous solutions (3D) and at the air-water interface (2D). Surveying the range of morphologies observed through 3D self-assembly of amphiphilic diblock copolymers (e.g. spheres, cylinders, vesicles, tubules), it is very tempting to compare them with the surface features described here, which appear to be "2D micelles" with an analogous set of morphologies (e.g. dots,

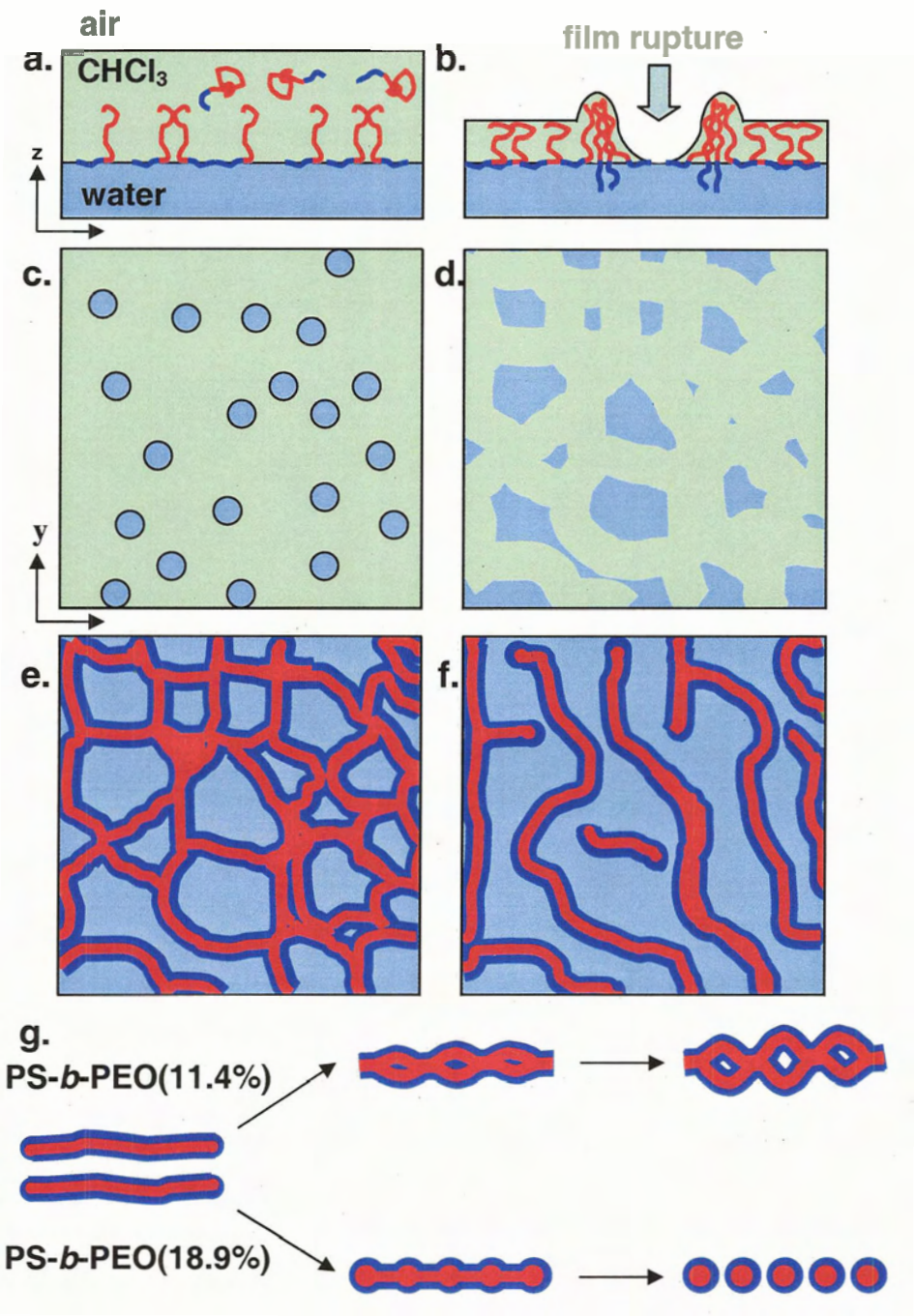

Figure 3.14. Pattern evolution in PS-*b*-PEO films spread at the air-water interface from chloroform solvent. A continuous film of PS-*b*-PEO in chloroform (a) dewets (b, side view, c, top view) at a critical film thickness. The holes expand resulting in a solvent swolen (d) cellular network (e) of contacted raised rims leading to spaghetti structures (f). Depending on the composition of the PS-*b*-PEO, the spaghetti breaks down into different morphologies (g).

spaghetti, rings, chains). However, the evidence suggests that this comparison is essentially flawed. As Devereaux et al. have pointed out previously, 3D block copolymer micelle morphologies represent, for the most part, thermodynamic free energy minima, while the 2D features described here and elsewhere appear to be kinetically-trapped states determined by the extent of chain entanglement before vitrification by solvent evaporation.[25] In fact, if all of the observed surface morphologies do evolve from an initial dewetting pattern, then the resemblance between (for example) spaghetti in 2D and cylinders in 3D is entirely coincidental—the former structure arising from the convergence of rims in a dewetting film, and the latter representing an optimization of curvature and chain stretching within the micelle core.[52] A critical point in this regard is that the large lateral dimensions of many 2D features compared to the PS chain dimensions,[25,26] and the necessary distribution of PS-PEO block junctions underneath these aggregates, suggests that PS chains in 2D "micelles" are stretched away from the air-water interface, perpendicular to the plane of the aggregate, unlike in 3D micelles, where core-forming chains are stretched from the aggregate periphery toward the centre, since the block junctions are localized at the walls of the core. This means that in 2D aggregates, the extent of PS chain stretching is essentially independent of the size and morphology of the lateral pattern: a fundamentally different situation than is found in micelle self-assembly in three dimensions.

3.4. Conclusions

In this chapter, we built on earlier results on spreading concentration dependence of aggregate morphology and isotherm behaviour for PS-*b*-PEO(11.4%) at the air-water interface. Here, we investigated the more hydrophilic PS-*b*-PEO(18.9%) copolymer, which presented an isotherm plateau indicative of a PEO pancake-to-brush transition, permitting analysis of the effect of spreading concentration on the two surface phases. For the brush phase, the limiting mean molecular area $A_{0,b}$ was found to increase below a critical spreading concentration ($\leq$ 0.25 mg/mL), similar to the trend in A_0 observed for PS-*b*-PEO(11.4%). However, for the PEO pancake phase, the limiting mean molecular area $A_{0,p}$ remained constant over the range of spreading concentrations, such that the plateau region became less extensive as the spreading concentration decreased. Based on these results, a simple model of PS and PEO chain conformations in aggregates from different spreading concentrations was developed, in which the packing density in the PS aggregates decreases, and PEO adsorption underneath the aggregates increases, as the concentration of spreading solution decreases. It was also suggested that the larger area occupied by the PS aggregates with decreasing spreading concentration results in increased hindrance to the pancake-to-brush phase transition of PEO chains extending from the periphery of the aggregates. $\pi - A$ isotherms were also obtained for multiple compression / expansion cycles, and the effect of spreading concentration on the observed hysteresis at different surface pressures appeared to support our model.

AFM results of surface aggregates of PS-*b*-PEO(18.9%) obtained at different spreading concentrations revealed a combination of spaghetti and dot features, with a greater predominance of dots as the spreading concentration decreased; no chain and ring

morphologies, observed previously for low spreading concentrations of PS-*b*-PEO(11.4%), were found for the more hydrophilic sample, suggesting that spaghetti aggregates evolve through different routes in the two samples, though attempting to optimize PEO adsorption in both cases. Finally, this chapter discussed AFM data of interesting patterns formed from PS-*b*-PEO(11.4%) at very high spreading concentrations, which we believe represent an early snapshot of morphology evolution at the air-water interface. From these images, it appears that the genesis of aggregate formation at the air-water interface involves dewetting of the evaporating copolymer solution from the water surface, with the expanding holes forming a 2D network of rims which then breaks down to form the various observed surface features.

3.4. References

(1) Whitesides, G. M.; Grzybowski, B. *Science* **2002,** *295*, 2418.

(2) Ozin, G. A. *Adv. Mater.* **1992,** *4*, 612.

(3) Heath, J. R.; Kuekes, P. J.; Snider, G. S.; Williams, R. S. *Science* **1998,** *280*, 1716.

(4) Zhu, J.; Eisenberg, A.; Lennox, R. B. *J. Am. Chem. Soc.* **1991,** *113*, 5583.

(5) Zhu, J.; Eisenberg, A.; Lennox, R. B. *Langmuir* **1991,** 7, 1579.

(6) Zhu, J.; Eisenberg, A.; Lennox, R. B. *Die Makromolecularle Chemie, Macromolecular Symposia* **1992,** 53, 211-220.

(7) Zhu, J.; Eisenberg, A.; Lennox, R. B. *J. Phys. Chem.* **1992,** *96*, 4727.

(8) Zhu, J.; Eisenberg, A.; Lennox, R. B. *Macromolecules* **1992,** *25*, 6547.

(9) Li, S.; Hanley, S.; Khan, I.; Varshney, S. K.; Eisenberg, A.; Lennox, R. B. *Langmuir* **1993,** *9*, 2243.

(10) Meszaros, M.; Eisenberg, A.; Lennox, R. B. *Faraday Discuss.* **1994,** *98*, 283.

(11) Li, Z.; Zhao, W.; Quinn, J.; Rafailovich, M. H.; Sokolov, J.; Lennox, R. B.; Eisenberg, A.; Wu, X. Z.; Kim, M. W.; Sinha, S. K.; Tolan, M. *Langmuir* **1995,** *11*, 4785.

(12) Li, S.; Clarke, C. J.; Lennox, R. B.; Eisenberg, A. *Colloid Surface, A.* **1998,** *133*, 191.

(13) Li, S.; Clarke, C. J.; Eisenberg, A.; Lennox, R. B. *Thin Solid Films* **1999,** *354*, 136.

(14) Cox, J.; Eisenberg, A.; Lennox, R. B. *Curr. Opin. Colloid In.* **1999,** *4*, 52.

(15) Gragson, D. E.; Jensen, J. M.; Baker, S. M. *Langmuir* **1999,** *15*, 6127.

(16) Cox, J. K.; Yu, K.; Eisenberg, A.; Lennox, R. B. *Phys. Chem. Chem. Phys.* **1999,** *1*, 4417.

(17) Cox, J. K.; Yu, K.; Constantine, B.; Eisenberg, A.; Lennox, R. B. *Langmuir* **1999,** *15*, 7714.

(18) Dewhurst, P. F.; Lovell, M. R.; Jones, J. L.; Richards, R. W.; Webster, J. R. P. *Macromolecules* **1998,** *31*, 7851.

(19) Goncalves da Silva, A. M.; Filipe, E. J. M.; d'Oliveira, J. M. R.; Martinho, J. M. G. *Langmuir* **1996,** *12*, 6547.

(20) Goncalves da Silva, A. M.; Simoes Gamboa, A. L.; Martinho, J. M. G. *Langmuir* **1998,** *14*, 5327.

(21) Faure, M. C.; Bassereau, P.; Carignano, M.; Szleifer, I.; Gallot, Y.; Andelman, D. *Eur. Phys. J., B.* **1998,** *3*, 365.

(22) Faure, M. C.; Bassereau, P.; Lee, L. T.; Menelle, A.; Lheveder, C. *Macromolecules* **1999,** *32*, 8538.

(23) Barentin, C.; Muller, P.; Joanny, J. F. *Macromolecules* **1998,** *31*, 2198.

(24) Baker, S. M.; Leach, K. A.; Devereaux, C. E.; Gragson, D. E. *Macromolecules* **2000,** *33*, 5432.

(25) Devereaux, C. A.; Baker, S. M. *Macromolecules* **2002,** *35*, 1921.

(26) Cheyne, R. B.; Moffitt, M. M. *Langmuir* **2005,** *21*, 5453.

(27) Alexander, S. *J. Phys.* **1977,** *38*, 983.

(28) Shuler, R. L.; Zisman, W. A. *J. Phys. Chem.* **1970,** *74*, 1523.

(29) Sauer, B. B.; Yu, H.; Yazdanian, M.; Zografi, G.; Kim, M. W. *Macromolecules* **1989,** *22*, 2332.

(30) Bailey, F. E.; Koleske, J. V., *Poly(ethylene oxide)*, Academic Press, 1976

(31) Bijsterbosch, H. D.; de Haan, V. O.; de Graaf, A. W.; Mellema, M.; Leermakers, F. A. M.; Cohen Stuart, M. A.; van Well, A. A. *Langmuir* **1995,** *11*, 4467.

(32) Charron, J. R.; Tilton, R. D. *Langmuir* **1997,** *13*, 5524.

(33) Sauer, B. B.; Yu, H.; Tien, C. F.; Hager, D. F. *Macromolecules* **1987,** *20*, 393.

(34) Rivillon, S.; Munoz, M. G.; Monroy, F.; Ortega, F.; Rubio, R. G. *Macromolecules* **2003,** *36*, 4068.

(35) Rother, G.; Findenegg, G. H. *Colloid Polym. Sci.* **1998,** *276*, 496.

(36) Xu, Z.; Holland, N. B.; Marchant, R. E. *Langmuir* **2001,** *17*, 377.

(37) Kumaki, J. *Macromolecules* **1988,** *21*, 749.

(38) Although the trends in A_0 were similar in the two PS-*b*-PEO samples, the absolute value of $A_{0,b}$ in the concentrated regieme was significantly decreased from Kumaki's empirical relation[37] (calculated to be 6000Å^2 for PS-b-PEO(18.9%)), which was obeyed by the more hydrophobic PS-*b*-PEO(11.4%). This deviation was likely due to the disproportionately taller PS-*b*-PEO(18.9%) structures observed via AFM as discussed in Section 3.3.3., as these would inherently have a decreased surface area at the interface.

(39) Xu, H.; Erhardt, R.; Abetz, V.; Muller, A. H. E.; Goedel, W. A. *Langmuir* **2001,** *17*, 6787.

(40) Seo, Y. I., J.-H.; Lee, J.-S.; Kim, J.-H. *Macromolecules* **2001,** *34*, 4842.

(41) Baskar, G.; Gaspar, L. J. M.; Mandal, A. B. *Langmuir* **2003,** *19*, 9051.

(42) Francis, R.; Taton, D.; Logan, J. L.; Masse, P.; Gnanou, Y.; Duran, R. S. *Macromolecules 36*, 8253.

(43) Beija, M.; Relogio, P.; Charreyre, M.-T.; Silva, A. M. G. d.; Brogueira, P.; Farinha, J. P. S.; Martinho, J. M. G.; lva, A. M.; Brogueira, P.; Farinha, J. P. S.; Martinho, J. M. G. *Langmuir* **2005,** *21*, 3940.

(44) Baekmark, T. R.; Elender, G.; Lasic, D. D.; Sackmann, E. *Langmuir* **1995,** *11*, 3975.

(45) Milling, A. J.; Hutchings, L. R.; Richards, R. W. *Langmuir* **2001,** *17*, 5305.

(46) Meyer, E.; Braun, H.-G. *Macromol. Mater. Eng.* **2000,** *276*, 44.

(47) Reiter, G. *Langmuir* **1993,** *9*, 1344.

(48) Reiter, G. *Phys. Rev. Lett.* **1992,** *68*, 75.

(49) Stange, T. G.; Evans, D. F.; Hendrickson, W. A. *Langmuir* **1997,** *13*, 4459.

(50) Brochard-Wyart, F.; Daillant, J. *Can. J. Phys.* **1990,** *68*, 1084.

(51) Rayleigh, L. *Proc. London Math Soc.* **1878,** *10*, 4.

(52) Zhang, L. E., A. *J. Am. Chem. Soc.* **1996,** *118*, 3168.

Chapter 4

Hierarchical Block Copolymer / CdS Quantum Dot Surface Features via Synergistic Self-Assembly at the Air-Water Interface

4.1. Introduction

Colloidal metal and semiconducting nanoparticles (NPs) have been recognized as promising building blocks for a new generation of photonic and electronic devices due, in part, to their unique and size-dependent properties arising from quantum confinement and surface effects.[1-9] Essential to the production of devices and materials with specific function will be the organization of NPs on solid substrates into ordered patterns with well-defined length scales. Both *top-down* (lithographic) and *bottom-up* (self-assembly) approaches have been utilized to achieve structural control in 1-, 2-, and 3-dimensions. The scientific allure of self-assembly goes beyond the elegance of the technique, as researchers continue to realize and exploit the molecular features that drive spontaneous routes to organization. To this end, a wealth of research has coupled self-assembly processes to the patterning of functional NP building blocks, in an effort to achieve hierarchical arrangements over multiple length scales.

A variety of equilibrium and non-equilibrium self-assembly techniques have been successful in patterning of NPs on surfaces. Passivated nanocrystals have been patterned into 2D circles and extended stripes via interparticle interactions at the air-water interface under equilibrium conditions,[10,11] and through non-equilibrium, drying mediated processes,[12-17] *inter alia*.[18]

Self-assembly strategies that combine control of NP organization with incorporation of NPs into a polymeric matrix offer additional possibilities for tuning the mechanical, optical, electronic, magnetic, and catalytic properties of new nanostructured composites. Along with the many attractive physical properties of the polymer component in such hybrid materials, self-assembling polymer systems offer unique

possibilities for mediating the assembly of NPs over many length scales.[19] A promising area of research focuses on block copolymer self-assembly, where the discrete properties of the polymer blocks provide a unique and tunable 'molecular handle' on self-assembly. Under specific conditions, microphase separation of the insoluble and covalently-connected blocks results in a wide range of ordered patterns depending on the block copolymer composition. Recently, these molecules have been recognized as potentially useful for directing the organization of NPs. The vast majority of examples employing block copolymers to direct the self-assembly of NPs have involved microphase separation in the solid state, whereby the preference of the NP to a particular polymer microdomain or interface promotes the autonomous organization of these particles. [20-23] In the resulting composites, the connectivity of the blocks limits the feature dimensions to the length of a polymer chains, on the order of tens of nanometers; as well, the patterns tend to be highly periodic. The need for NP / polymer assemblies with exceedingly small dimensions across two axies (one-dimensional, 1D) and one axis (two-dimensional, 2D), applicable to emerging classes of defect-tolerant systems,[24] and where mesoscopic length scales are possible for interactions with light, have presented a challenge to create materials that address these issues.

To meet these requirements, we[25] and others[26-29] have investigated the self-assembly of PS-*b*-PEO diblock copolymers at the air-water interface. The tendency for the hydrophobic PS block to aggregate upon deposition competes with the spreading of the epiphilic (surface-loving) PEO block, resulting in unique and stable structures that are kinetically trapped through the vitrification of the PS block upon solvent evaporation. Depending on the relative molecular weights of the blocks and the concentration of the

spreading solution, a wide range of surface morphologies are possible, including dots, spaghetti (wires), and planar 'continents.'[25-29] Recently, we have also shown that for the PS-*b*-PEO(11.4%) block copolymer described in Chapters 2 and 3, unique ring and chain morphologies could be obtained below a critical concentration of spreading solution. Compared to block copolymer self-assembly in the bulk, where localization of block junctions at domain interfaces limits characteristic feature sizes to polymer chain dimensions,[30] block copolymer self-assembly at the air-water interface allows access to polymer features with dimensions orders of magnitude larger than a polymer chain; this is attributed to the fact that the block junctions are localized at the air-water interface, such that features arise from the lateral organization of many chains arranged in a brush-like manner.

In order to exploit the self-assembly properties of PS-*b*-PEO diblock copolymers at the air-water interface in the organization of inorganic NPs, it was first necessary to create NPs with polymeric stabilizing chains amenable to preferential interactions with the aggregate-forming PS block. It has been shown by Moffitt et al.[31-33] that metal and semiconducting NPs can be synthesized via a template approach inside a micellized polystyrene-*block*-poly(acrylic acid) (PS-*b*-PAA) diblock copolymer, ultimately resulting in a polymer-stabilized NP that is soluble in organic media and a host of compatible polymers. An important class of inorganic NPs are the type II / VI semiconducting materials, due to their interesting size-dependent photoluminescence and nonlinear optical properties.[1, 9] In this study, we synthesized cadmium sulfide (CdS) NPs inside a PS-*b*-PAA block copolymer template, to yield hybrid colloidal particles (referred to hereafter as PS-CdS, Scheme 4.1) consisting of a CdS NP core surrounded by two layers

of the respective copolymer blocks: an ionically cross-linked, high-T_g poly(cadmium acrylate) layer at the NP surface provides kinetic stability for an outer brush layer of PS chains, which gives the CdS NPs solubility in various organic solvents and allows dispersion in polymer media. The PS brush of the PS-CdS allows preferential interactions with the PS block of PS-*b*-PEO, while being incompatible with both the water surface and the PEO block of the copolymer.

In an effort to obtain 1D and 2D hierarchical NP / polymer assemblies, chloroform solutions of PS-CdS blended with PS-*b*-PEO block copolymers in various proportions and to various concentrations were deposited dropwise at the air-water interface of a Langmuir trough. Evaporation of chloroform induced interfacial self-assembly of the blended components, after which the resulting features were compressed to the desired surface pressure (π) and transferred vertically to various substrates via the LB technique. The interfacial assembly was monitored through extensive atomic force microscopy (AFM) and transmission electron microscopy (TEM) studies of the LB films. Additionally, $\pi - A$ isotherms were accumulated for the composite assemblies, in an effort to obtain further insight into the surface structure of the aggregates.

4.2. Experimental

4.2.1. Synthesis of Block Copolymer-Stabilized Cadmium Sulfide Nanoparticles (PS-CdS)

As described in the introduction, block copolymer-stabilized CdS NPs (PS-CdS) were synthesized via a template approach starting from a diblock copolymer and the salient points for this procedure are outlined in Scheme 4.1. This section is dedicated to describing and identifying the pertinent reagents, reactions, conditions and products involved. The polystyrene-*block*-poly(*tert*-butylacrylate) (PS-*b*-PtBA) starting material was synthesized by anionic polymerization and was kindly supplied by Jo Wang; the interested reader is directed to his thesis[35] and other detailed sources for further information.[31,36-39]

4.2.1.1. Characterization of Polystyrene-block-Poly(tert-butylacrylate)

The polystyrene-*block*-poly(*tert*-butylacrylate) (PS-*b*-PtBA) obtained from Jo Wang was used as received. The characteristics of the polymer are defined in Table 4.1 where M_n is the number average molecular weight, M_w is the weight average molecular weight, P.I. is the polydispersity index and x_n is the number average degree of polymerization of the given block.

Table 4.1. Characteristics of PS-*b*-PtBA

	M_n ($g \cdot mol^{-1}$)	M_w ($g \cdot mol^{-1}$)	P.I.	$M_{n,PS}$ ($g \cdot mol^{-1}$)	$x_{n,PS}$	$M_{n,PtBA}$ ($g \cdot mol^{-1}$)	$x_{n,PtBA}$
PS-*b*-PtBA	14600	15200	1.04	1500	130	1500	20

*Molecular weights determined from GPC-LALS

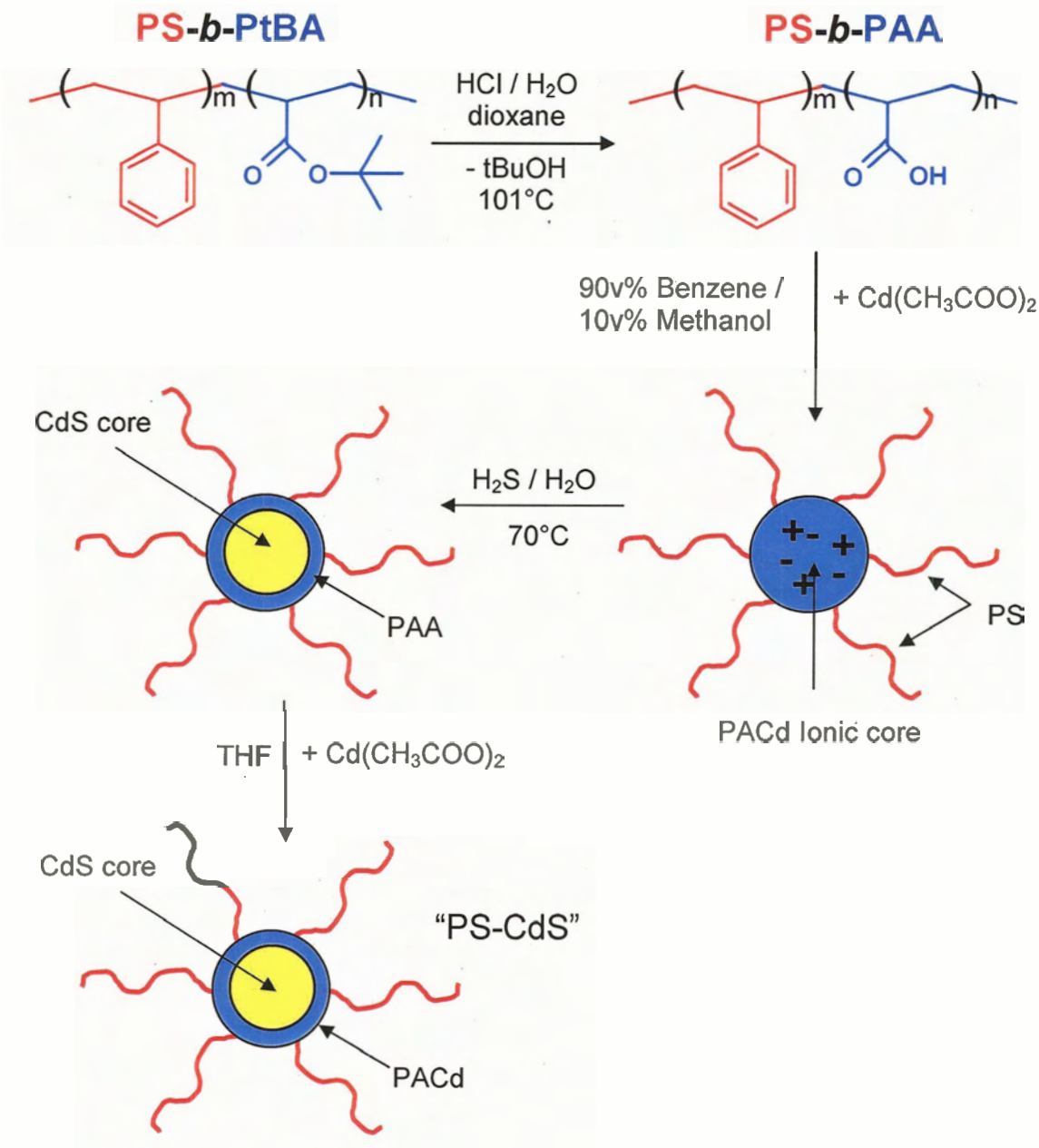

Scheme 4.1. Overview of the synthesis of PS-CdS from polystyrene-*block*-poly(*tert*-butylacrylate) (PS-*b*-PtBA)

4.2.1.2. Preparation of Polystyrene-block-Poly(acrylic acid)

It is well established that *para*-toluenesulfonic acid in toluene is an effective catalyst / solvent system in cleaving the *t*-butyl group from a PtBA block.[31] This reaction was attempted in the present study initially with a 1.5x mole excess of *para*-toluenesulfonic acid in toluene, relative to the acrylate content. An overnight reflux followed by precipitation in methanol did not yield the desired product as the classic disappearance of the strong and sharp singlet at 1730 cm^{-1} (Figure 4.1a) to a broad doublet centered around 1730 cm^{-1} was not observed. Subsequent attempts using up to a 10 x mole excess of catalyst relative to the acrylate content and refluxing for up to a week proved unsuccessful. It was reasoned (but not confirmed) that precipitation in methanol with the acid present caused a transesterification reaction between the PAA and methanol, resulting in a polymethacrylate (PMA) block. It has been speculated that the leaving group from the hydrolysis of PtBA by this method is 2-methyl propene,[40] thus replacing the *tert*-butyl group with a methyl would effectively eliminate this mechanism from contention, making subsequent hydrolysis attempts futile. As such, an aqueous acid-catalyzed process was employed utilizing concentrated HCl in 1,4 dioxane.[41] Assuming a transesterification reaction had occurred, the desired elimination of methanol would be facilitated through the nucleophilic attack of a water molecule on the electrophillic carbonyl group of the methyl ester, resulting in the desired PAA block.

The procedure consisted of making a 4 wt% solution of the diblock copolymer in 1,4-dioxane. A 10x mol excess (relative to the acrylate content) of HCl (37%, Aldrich) was added dropwise to the rapidly stirred solution. Refluxing the solution overnight at 101 °C yielded a clear, faintly brown solution which was condensed via rotary

evaporation and cooled to ~ 10°C. Precipitation into *iso*-propanol and drying for 2 days under an active vacuum maintained at 65°C produced a white powder. FTIR showed an obvious change in the sharp C=O ester stretch at 1730 cm^{-1}, observed in the FTIR of PS-*b*-PtBA (Figure 4.1a), to a relatively broad doublet in the same region (Figure 4.1b) suggesting a successful hydrolysis of the ester to PS-*b*-PAA. Additionally, the sharp peak at 1150cm^{-1}, associated with the C-O stretch of the *tert*-butyl group was all but eliminated (Figure 4.1b) providing further support in favour of a successful hydrolysis.

4.2.1.3. Preparation of Polystyrene-block-Poly(cadmium acrylate) Micelles

The dry PS-*b*-PAA was dissolved in a 90/10 (v/v) solution of benzene / methanol to make a 2 wt% polymer solution. Although this mixture is not a good solvent for PAA, the PAA composition was sufficiently low such that micellization did not occur. Addition of a 2x mol excess (relative to the acrylic acid content) of cadmium acetate ($Cd(CH_3COO)_2$, 98% Aldrich) in a minimum amount of methanol was added to induce micellization via removal of the labile proton on the poly(acrylic acid) block, resulting in an ionic poly(cadmium acrylate) (PACd) block. The charged block was thermodynamically unstable in the solvent and underwent aggregation to yield micelles with a PACd core and a soluble PS corona. After stirring overnight, the blue-tinged solution was concentrated and precipitated into methanol. Recovery of the white powder was achieved through vacuum filtration of the suspension. As any 'free' Cd^{2+} would interfere with ensuing chemistry, it was absolutely necessary to ensure that it was all removed before proceeding. To accomplish this, the white powder was washed with methanol until three consecutive tests of the supernatant were negative for Cd^{2+} (nine

washings in total). The supernatant was tested with Na_2S; if Cd^{2+} was present, the supernatant would turn yellow on addition due to the formation of CdS. The white powder was dried under active vacuum at 65°C overnight.

Neutralization of the PAA block to the ionic PACd block was monitored via FTIR (Figure 4.1c). The doublet centered at 1730 cm^{-1} completely disappeared, while a broad peak at ~1550 cm^{-1} became obvious, both indicative of neutralization. The extent of micellization was monitored via GPC (Viscotek Model 302, Section 4.2.2.1). It was observed that the PS-*b*-PACd showed two peaks by GPC-RI (refractive index detector): a broad, high-molecular weight peak (lower elution time) and a narrower, low-molecular weight peak. The high-molecular weight peak was attributed to the micelle fraction, which contributed 77 % of the total weight of the sample (Table 4.2); the low-molecular weight peak was attributed to single chains, perhaps PS homopolymer or an unmicellized diblock fraction. GPC-LALS (light scattering detector) showed that the broad, high-molecular weight peak also scattered disproportionately more light than the narrow, low-molecular weight peak, further suggesting that the former is due to aggregated copolymer, or micelles.

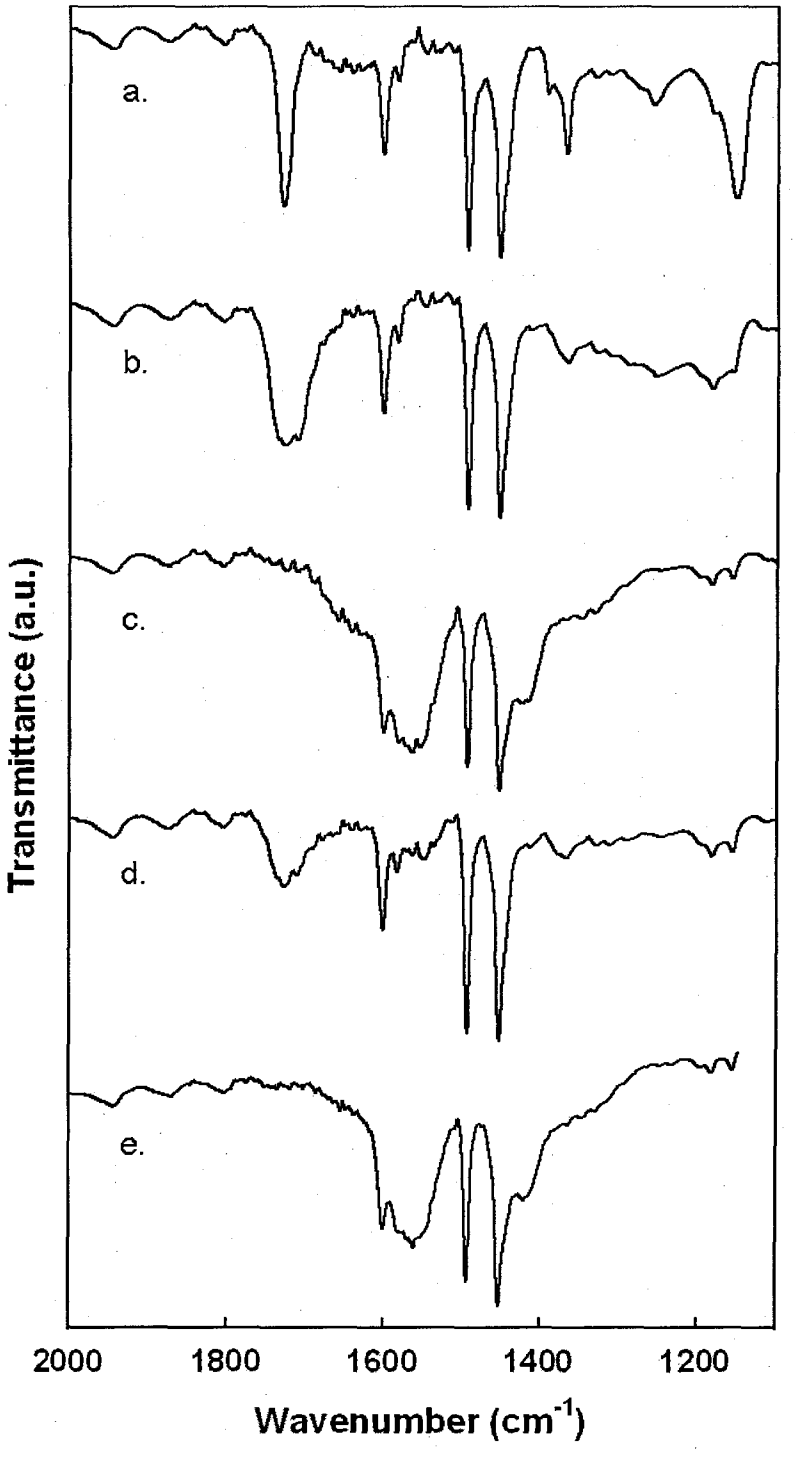

Figure 4.1. FTIR spectra of; (a) polystyrene-*block*-poly(*tert*-butyl acrylate) (PS-*b*-PtBA), (b) polystyrene-*block*-poly(acrylic acid) (PS-*b*-PAA), (c) polystyrene-*block*-poly(cadmium acrylate) (PS-*b*-PACd), (d) polystyrene-*block*-poly(acrylic acid (CdS)) (PS-*b*-PAA(CdS)) and (e) the final micelle, PS-CdS

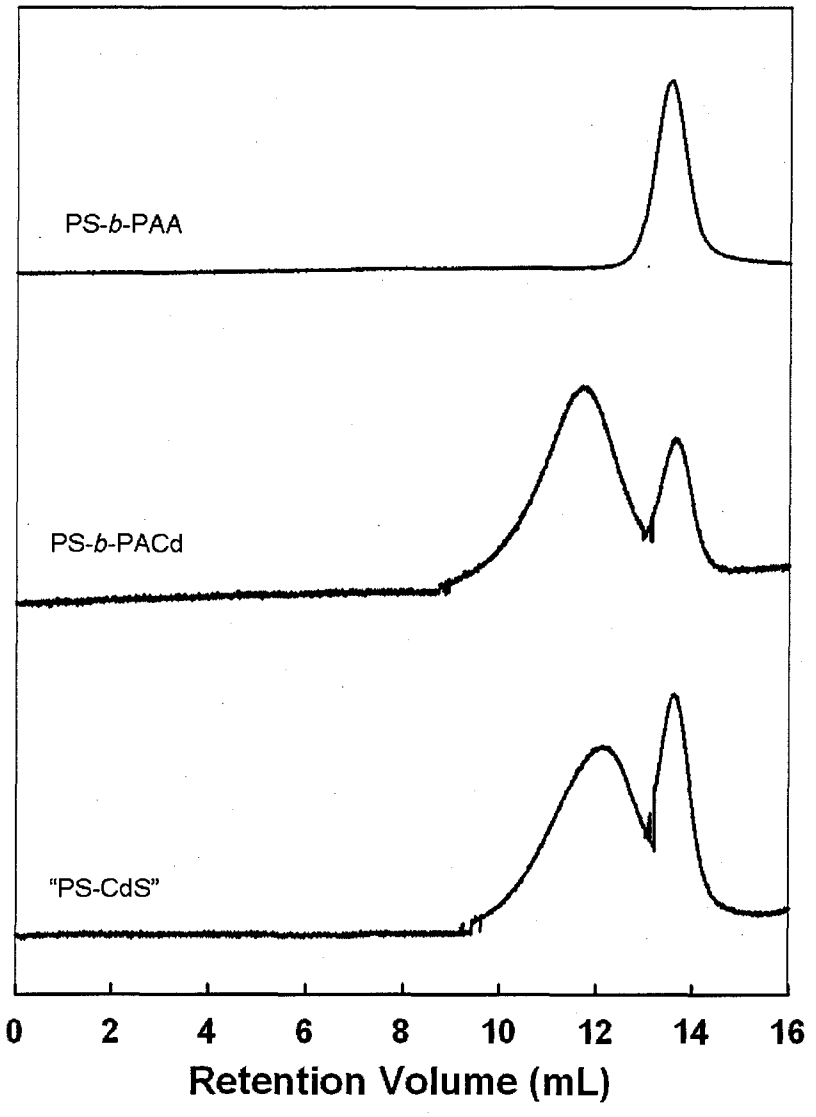

Figure 4.2. Gel permeation chromatograph of polystyrene-*block*-poly(acrylic acid) (PS-*b*-PAA), and the neutralized species polystyrene-*block*-poly(cadmium acrylate) (PS-*b*-PACd), and the final micelle PS-CdS in THF

Table 4.2. Molecular weights and relative weight contributions (f) of the micelle fraction obtained via GPC in THF

Sample	f	M_n (g·mol^{-1})	M_w (g·mol^{-1})	P.I.
PS-*b*-PACd	0.77	680000	861000	1.25
PS-CdS	0.68	620000	781000	1.26

*Molecular weights are determined using GPC-LALS

4.2.1.4. Preparation of Polystyrene-block-Poly(cadmium acrylate)-Stabilized Cadmium Sulfide Nanoparticles (PS-CdS)

The PS-*b*-PACd ionomer micelles were used as a nanoreactor in the synthesis of the CdS NPs. For the synthesis to be successful, it was first necessary to lower the T_g of the core in order to increase mobility of the PAA blocks. To achieve this, the PS-*b*-PACd micelles were exposed to a 100%-humidity environment by placing the polymer in a sealed beaker containing deionized water (diH_2O, 18.2 mΩ·cm) at 70 °C for 10 days. The 'wet' powder was then removed from the humidity chamber, sealed in a flask maintained at 70 °C and flushed with N_2 (bubbled first through diH_2O) for 30 minutes. H_2S was then introduced, bubbled through diH_2O and then into the sample chamber at a rate of ~ 1mL/min for 9 hours. The water molecules in the swollen core effectively acted as a plasticizing agent, permitting the PAA chains to move upon growth of the incipient CdS NP. Upon exposure, the white powder turned yellow indicating the formation of CdS NPs. The yellow powder was then flushed again with N_2 to remove residual H_2S, and subsequently dried under active vacuum maintained at 70 °C overnight. Reaction of the copolymer with H_2S was monitored via FTIR (Figure 4.1d) which showed the reappearance of the doublet at 1730 cm^{-1}, and disappearance of the broad 1550 cm^{-1} peak suggestive of a reprotonation of the anionic PACd block back to PAA.

At this point it has been proposed that the chemical structure at the CdS / polymer interface consists of HS^- / carboxylic acid hydrogen-bonding interactions,[9] which presumably stabilize the micelle structure. However, to further stabilize the micelle, it was necessary to reneutralize the PAA layer at the CdS surface, which increases the surface tension between the surface layer and the solvent, creates a high-T_g PACd surface

layer, and provides Cd^{2+} ionic cross-links within the surface layer. This was achieved by reneutralizing the micelles with $Cd(CH_3COO)_2$ (1.5x mol excess of Cd^{2+} relative to the acrylic acid content) to finally obtain PS-CdS (Scheme 4.1). By FTIR, PS-CdS showed the 1730 cm^{-1} peak shifting to ~1550 cm^{-1}, indicative of a successful neutralization (Figure 4.1e). The final PS-CdS sample was analyzed by GPC (Figure 4.2c), which showed two peaks: a PS-CdS micellar fraction and a single chain fraction as quantified in Table 4.2. The micellar weight fraction of PS-CdS was decreased relative to its PS-*b*-PACd predecessor ($f = 0.68$ compared to 0.77, respectively), which is likely due to loss of PS-*b*-PAA chains from the micelle after H_2S treatment. This is supported by the lower molecular weight of PS-CdS compared to PS-*b*-PACd in THF (Table 4.2).

4.2.2. Characterization of PS-CdS and Precursors

4.2.2.1. Gel Permeation Chromatography (GPC)

All GPC measurements were conducted on a Viscotek Model 302 liquid chromatography system equipped with refractive index (RI), low-angle light scattering (LALS, $\theta = 7°$), right-angle light scattering (RALS, $\theta = 90°$), and UV detectors. THF was used as the eluent at a flow rate of 1 mL/min and a column temperature of 35 °C. All polymer solutions were filtered through two 0.45 μm Teflon filters (Target) prior to injection. Two ViscoGEL HR High Resolution Columns (styrene-divinyl benzene columns) in series were used: G3000 HR 60 k GMHHR-M Mixed Bed 4 M columns.

M_w and M_n were determined from SEC data through an algorithm (Viscotek) which relies on LALS detection from a 670 nm diode laser source. This utilizes the

fundamental Zimm equation for light scattering from polymer solutions of concentration c and angle θ:

$$\frac{Kc}{\Delta R_\theta} = \frac{1}{M_w P(\theta)} + 2A_2 c \qquad \textbf{4.1}$$

where ΔR_θ, the excess Rayleigh scattering ratio is the ratio of scattered light from the solution compared to that of the pure solvent at given angle, K is a composite of optical and fundamental constants, $P(\theta)$ is the angle dependent particle scattering factor, and A_2 is the second virial coefficient. In the typical Zimm plot approach (described in detail in Section 4.3.1.1), M_w is analyzed by detecting scattered light at a series of angles, followed by extrapolation to $\theta = 0$, where $P(\theta) = 1$. The single, low angle ($\theta = 7°$) detected by the Viscotek system allows the approximation that $P(\theta) = 1$ yielding the simplified Zimm equation:

$$\frac{Kc}{\Delta R_{7°}} \approx \frac{1}{M_w} + 2A_2 c \qquad \textbf{4.2}$$

so that M_w can be calculated without multi-angle extrapolation.

4.2.2.2. Static Light Scattering (SLS)

Static light scattering (SLS) experiments were carried out on a Brookhaven Instruments multi-angle system equipped with a BI-200SM goniometer, a BI-9000AT digital autocorrelator, and a Melles Griot He-Ne Laser (632.8 nm) with maximum power

output of 75 mW. As dust particles are detrimental to any light scattering investigation, great care was taken to ensure that samples were prepared and remained dust-free. As such, all solutions were prepared in new scintillation vials (Brookhaven, 12mL) cleaned three times with acetone, and three times with spectroscopic grade chloroform (99.9+%, Aldrich) that was filtered through two 0.20 μm pore size Teflon filters (Target). A ~ 4 mg/mL solution of PS-CdS was prepared via addition of spectroscopic grade chloroform, which was filtered as described above and added directly solid PS-CdS. After stirring overnight, this solution was filtered through two 0.45 μm Teflon filters (Target) followed by dilution with filtered chloroform to a concentration of 0.10 mg/mL. Five solutions were prepared via serial dilution of this stock to a minimum concentration of 0.40 mg/mL SLS measurements were conducted in 5° increments from 35 - 155°, and 20 repeat measurements of scattered light intensity, averaged over one second, were taken at each angle and concentration. The reported M_w, R_g and A_2 were determined by plotting $Kc/\Delta R_\theta$ as a function of $\sin^2\theta$ to achieve a Zimm plot. All SLS measurements were performed at 23 °C.

4.2.2.3. Dynamic Light Scattering (DLS)

Dynamic light scattering (DLS) experiments were carried out on a Brookhaven Instruments photon correlation spectrometer equipped with a BI-200SM goniometer, a BI-9000AT digital autocorrelator, and a Melles Griot He-Ne Laser (632.8 nm) with maximum power output of 75 mW. As with SLS measurements, great care was taken to ensure that all samples were prepared and remained dust free. Spectroscopic grade chloroform was filtered through 0.20 μm Teflon filters (Target) in all cases. A 0.10

mg/mL solution was prepared by dilution of a ~ 4.0 mg/mL stock solution filtered through two 0.20 μm Teflon filters (Target), from which four other solutions were made via serial dilution to 0.04 mg/mL. For each concentration, an autocorreltation function was obtained in triplicate at each of six different angles of detection (55°, 70°, 90°, 105°, 120°, and 135°). For all measurements, the normalized time correlation function of the electric field was analyzed using a cumulant expansion:

$$|g(\tau)| = \exp[-\overline{\Gamma}\tau + (\mu_2 / 2!)\tau^2 + ...] \qquad \textbf{4.3}$$

where $\overline{\Gamma}$ is the mean relaxation rate and μ_2 is the second moment. All DLS measurements were performed at 23°C.

4.2.2.4. UV / Vis Absorption Spectroscopy

Due to the effect of size quantization described in Chapter 1, electronic features of the CdS NP core were used to determine the size of the CdS, as decreasing size shifts the absorption threshold to shorter wavelengths. We employed UV / vis absorption spectroscopy on a Varian Cary 50 UV / vis spectrometer to probe this electronic feature where the absorption edge has been correlated with CdS particle size through Henglein's empirical relationship.[1] The UV / vis absorption spectrum of a PS-CdS / chloroform solution in a 1.0 cm quartz cell was obtained against a chloroform baseline between 250 and 800 nm.

4.2.3. Surface Pressure – Area Isotherms of PS-CdS / PS-b-PEO Langmuir Films

Surface pressure-area (π - A) isotherms and LB thin films were obtained using a KSV 3000 Langmuir trough (KSV Instruments Ltd.) secured inside a dust shield. The total trough surface area was 150 × 515 mm^2 and total trough volume was ~1 L. The trough area was robotically controlled by two hydrophobic paddles, which compressed the spread film symmetrically, and bilaterally at a rate of 10 mm/min. House-distilled, deionized water (Barnstead NANOpure Diamond, 18.2 mΩ·cm) was used as the subphase in all trials. Prior to each trial, the water surface was cleaned by aspirating off any debris such that the surface pressure remained < 0.20 mN/m over a full compression. The LB components were cleaned daily with absolute ethanol before replacing the deionized water subphase. Surface pressure measurements were made from a roughened platinum Wilhemly place (perimeter of 39.240 mm), which was flamed prior to each trial to ensure cleanliness.

PS-CdS spreading solutions were prepared from a ~ 4 mg/mL stock solution initially filtered through two 0.45 μm pore diameter Teflon filters (Target) followed by addition of spectroscopic grade chloroform (99.9+%, Aldrich) to a concentration of 2.0 mg/mL. The 2.0 mg/mL was used as the stock solution for the preparation of all subsequent solutions. PS-*b*-PEO solid was dried overnight in a dark dessicator, weighed, and made into a 2.0 mg/mL stock solution, from which all other diluted solutions were made. For each PS-CdS and PS-*b*-PEO, five stocks were separately made at concentrations of 2.0, 1.0, 0.50, 0.25, and 0.10 mg/mL, again, accurate to 3 significant figures. Various blend solutions were then prepared by adding appropriate ratios at the given concentration into new, cleaned (3x with acetone, 3x with spec grade chloroform)

vials to give the desired PS-CdS weight fraction (f) at given cumulative concentration in mg/mL.

In a typical isotherm experiment, a cumulative mass of 0.10 mg was deposited dropwise from an appropriate volume of solution contained in a gas tight Hamilton microsyringe onto a clean air-water interface of the Langmuir trough. After an elapsed time of 15 minutes (to allow for solvent evaporation) the film was compressed to the limits of the Langmuir trough. Monitoring π as a function of available area A (now recorded as available trough area since the presence of two separate components made a mean molecular area axis meaningless) resulted in the $\pi - A$ isotherm as described in the previous chapters.

4.2.4. Langmuir-Blodgett Transfer of PS-CdS / PS-b-PEO Blends

The Langmuir films of the PS-CdS / PS-*b*-PEO blends were prepared in an analogous fashion to those described in Section 4.2.3, on the KSV 3000 LB trough equipped with a KSV dipper. To optimize the transfer ratio, 0.05 mg of material (half the mass used in the isothermal studies) was deposited at the air-water interface. Several dips and subsequent imaging confirmed that the structures were identical regardless of the mass deposited. The procedure consisted of deposition, followed by the requisite 15 minutes for solvent evaporation, subsequent compression at 10 mm/min to the desired π. This π was maintained for 10 minutes before an upward vertical transfer of the Langmuir film yielded the LB films on the appropriate substrate for either AFM or TEM studies. The substrates used for the AFM investigations were glass microscope slides (VWR Scientific, 18 x 18 mm) cleaned through sonication (20 min) in spectroscopic grade

chloroform (99.8%, Aldrich). TEM was not compatible with the glass substrates used in the AFM study, therefore a procedural modification was developed to account for this.

The TEM instrument (Hitachi H-700) requires a 3 mm microscopy grid with regions of low density material that are not strongly scattered by the incoming electron beam. To satisfy this requirement we affixed 300 mesh Cu grids (SPM Labs) to a glass substrate by first floating a thin film of Formvar (SPM Labs) over a deionized water subphase, transferring 3 – 5 Cu TEM grids (SPM; 300 mesh) to the floating Formvar layer and adhering the grid / Formvar film to a clean glass substrate (VWR 18 x 18mm) so that the Formvar was exposed to the air, and the grids were sandwiched between the Formvar and glass. After drying overnight under a dust shield, a thin layer of carbon was evaporated over the substrate to increase the film resilience to the TEM electron beam. A schematic representation of this substrate is provided in Figure 4.3a.

The thin Formvar film was prepared by vertically withdrawing a clean 3 x 1" microscope slide (Bio-Nuclear Diagnostics Inc.; cleaned with lens paper and methanol) from a 0.5-wt% Formvar solution in $CHCl_3$ (SPM Labs), and air-drying (~30 seconds). After scratching the edges with a razor blade, the film was removed by slowly dipping the glass in deionized water at ~ 45° where the surface tension of the water provided the impetus for the film transfer from glass to the water surface.

To increase reproducibility between AFM and TEM a procedure was invented which modified the LB dipping mechanism so that it could house both types of substrates at the same time. This was achieved by affixing a glass slide for AFM analysis plus a Formvar / Cu grid containing glass slide for TEM investigations held in tandem on a modified dipper head, as described in Figure 4.3b. The respective substrates were held to

the Blodgett dipper through clean binder clips affixed to a 3 x 1" microscope slide. The film transfer was completed in an analogous fashion to that of the pure PS-*b*-PEO films in that the submerged substrates were withdrawn at a rate of 1 mm/min yielding transfer ratios that were ~ 1.0.

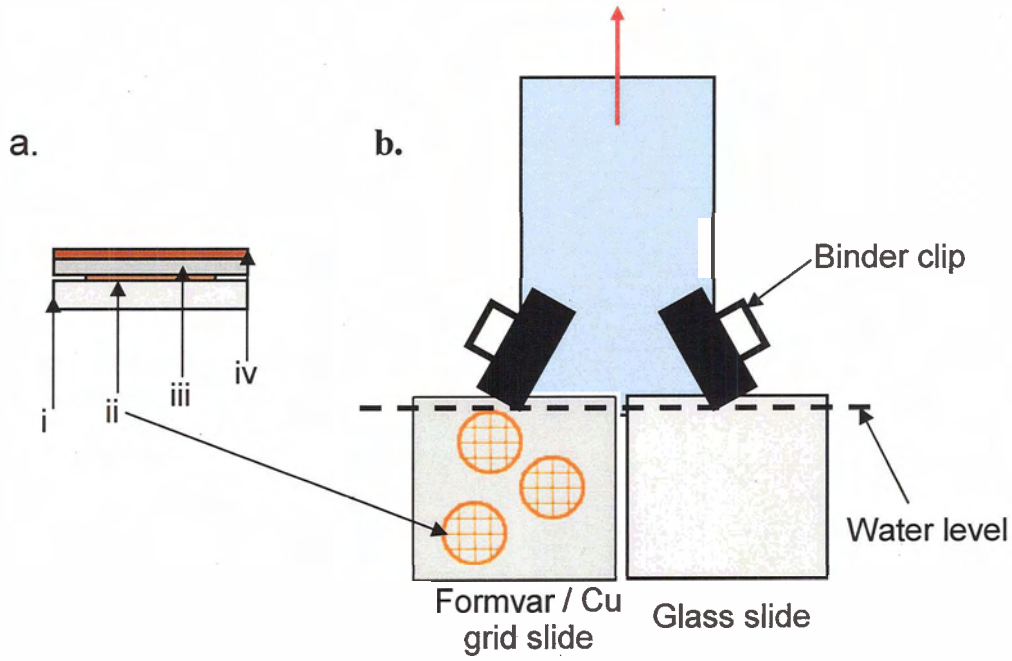

Figure 4.3. Substrates and modified dipper head used in the LB transfer of PS-CdS / PS-*b*-PEO blend films from the air-water interface. (a) Exposed surfaces of the Formvar coated Cu grids on the glass substrate before film transfer; i) glass substrate, ii) 300 mesh Cu TEM grid, iii) Formvar layer, and iv) evaporated carbon layer. (b) Schematic representation of tandem set-up of glass slide for AFM and Formvar coated Cu grids affixed to a glass slide for TEM. Red arrow indicates transfer direction from a previously submerged substrate.

4.2.5. Atomic Force Microscopy

The LB films on glass substrates described in Section 4.2.4 were imaged on a Veeco (ThermoMicroscopes Explorer) Instrument equipped with a Veeco tip (Nanoprobe-MLCT-EXMT-A) operating in contact mode. A typical image was 10 μm x 10 μm, and acquired at a tip scanning rate of ~ 10 μm/s. To minimize vibration induced abnormalities in the image, the AFM probe was housed on a vibration isolation platform maintained at 80 psi and covered with a vibration dampening shield in all cases. Each sample was imaged several times at different locations on the substrate to determine statistical reproducibility. Additionally, as each 10 μm x 10 μm AFM image only represents a minute fraction of the total interface, it was necessary to accumulate a significant number of images, ~ 1500 in total. The images presented were representative of a typical image at given spreading solution concentration and blend composition, and optimized in terms of presentability, where the brightness, contrast, and contour levels of AFM were adjusted. The images used for dimensional analysis were not optimized in the same way as this has a slight effect on the quantitative dimensions of the surface features, but not on the qualitative structures.

4.2.6. Transmission Electron Microscopy

TEM was performed on a Hitachi H-700 electron microscope, operating at an electron accelerating voltage of 75 kV. The PS-CdS / PS-*b*-PEO blend films transferred via the LB method (Section 4.2.4) onto the Formvar / Cu grids were used in the investigation. A total of ~ 300 TEM images from ~ 60 individual LB transfers were accumulated. Qualitatively, the structures observed under the electron beam were

representative of the AFM images, suggesting the LB transfer to the disparate TEM substrate had negligible influence on the morphologies or predominance of certain surface features.

4.3. Results and Discussion

4.3.1. Characterization of PS-CdS

4.3.1.1. Static Light Scattering of PS-CdS in $CHCl_3$

The GPC characterization of the PS-CdS micelles was performed in THF, as the Viscotek GPC employed in the present study was not run with chloroform. As chloroform was the solvent employed for spreading PS-CdS and PS-*b*-PEO onto the water surface, it was necessary to characterize the behaviour and colloidal structure of the PS-CdS in chloroform. Even though the Viscotek GPC system uses light scattering to determine molecular weight through the Zimm equation, the multi-angle function of the Brookhaven system permits more accurate extrapolation to zero angle and a more accurate M_w. Additionally, other parameters were not available from the single-angle analysis of the GPC, therefore requiring multi-angle analysis for their characterization.

To this end we employed SLS, which is an extremely powerful analytical tool that permits acquisition of several important parameters that define a polymer or colloid in a given solvent. In addition to M_w, the radius of gyration (R_g) is obtainable, which is a measure of the average distance from the centre of gravity of the scattering centre to the chain end, as well as the second virial coefficient (A_2) which defines the extent of attractive or repulsive interactions in the polymer / solvent system. To determine these parameters, multi-angle, multi-concentration SLS studies were performed and analyzed

through a Zimm plot.[42] It is known that when particles are sufficiently large with respect to the incident light ($d > \lambda/20$) they scatter light in accordance with the Zimm equation:

$$\frac{Kc}{\Delta R_\theta} = \frac{1}{P(\theta)M_w} + A_2 c + \ldots \qquad \textbf{4.4}$$

ΔR_θ is the excess Rayleigh ratio of the solution at a given scattering angle θ, and c is the concentration in g/L. The optical parameter K is an assembly of optical constants that is specific to the solution under study:

$$K = \frac{4\pi^2 n^2 (dn/dc)^2}{\lambda_o^4 N_A} \qquad \textbf{4.5}$$

where N_A is Avogadro's number, λ_0 is the wavelength of the laser, n refers to the refractive index of the solvent, and *dn/dc* is the refractive index increment and describes the change in refractive index of the solution as a function of solute concentration, and was taken to be 0.16 mL/g, the value of PS in chloroform. The angular attenuation by destructive interference arising from intraparticle scattering is measured by the particle scattering factor (or form factor), $P(\theta)$, which is the ratio of actual scattering intensity to scattering intensity in the absence of interference measured at the same angle θ.[43] In the limit of small θ, the form factor is related to the size of the scattering centre (independent of shape) through the relation:

$$\frac{1}{P(\theta)} = 1 + \frac{16\pi^2}{3\lambda^2} R_g{}^2 \cdot \sin^2(\theta/2) \qquad \textbf{4.6}$$

The results of the extrapolated Zimm plot for PS-CdS in $CHCl_3$ are given in Table 4.3. It becomes immediately apparent that the M_w is significantly (~ 8 times) larger than the M_w obtained via GPC in THF (Table 4.2). Additionally, the R_g is significantly larger than what would be expected for a PS block with $x_n = 130$ and a relatively small micelle. Considering the GPC has a separation step as the material runs through the column, supermicellar aggregates could be present in the 'unfractionated' $CHCl_3$ system used in the LS studies which would scatter a disproportionately large amount of light. As SLS is an average intensity acquisition mode, the presence of small amounts of large scatterers would result in a systematic error in both the M_w and R_g to high values. Some aggregation of some PS-CdS particles is quite possible when one considers the value of A_2 (Table 4.3). A positive value of A_2 is suggestive of repulsive interactions indicating good polymer / solvent compatibility. A negative A_2 indicates net attractive interactions between the chains resulting from poor compatibility between the polymer and solvent. When A_2 is zero, there exist no net attractive or repulsive interactions and the solvent is said to be a theta solvent, and the dimensions of the polymer are based exclusively on short-range interactions. The large standard deviation in our A_2 spans both the positive and negative regimes, thus it is possible that net interactions are somewhat attractive resulting in supermicellar aggregation and providing a possible explanation for the higher than expected values of M_w and R_g. It is also informative to consider the behaviour of PS homopolymer under similar solvent and temperature conditions, since PS-CdS is expected to behave thermodynamically like PS in solution. At 23 °C, chloroform is a good solvent for PS, and therefore would be expected to induce net repulsion between

chains. Based on this argument A_2 was expected to be positive, though comparison to SLS data on PS-CdS is difficult due to the large deviation.

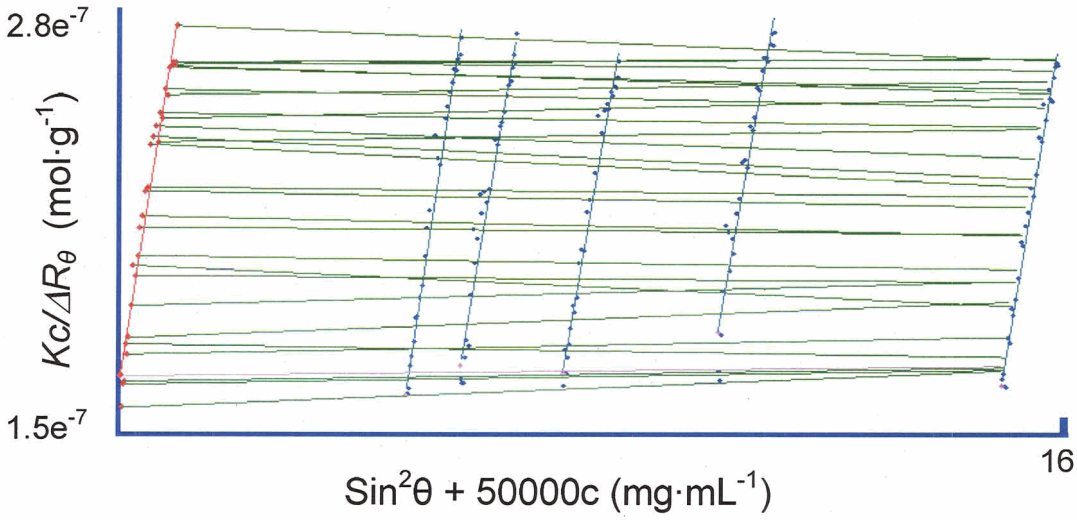

Figure 4.4. Zimm Plot of PS-CdS in $CHCl_3$. Red line indicates extrapolation to zero angle and pink line indicates extrapolation to zero concentration.

Table 4.3. Summary of SLS data obtained via a Zimm plot on PS-CdS in $CHCl_3$

Sample	Extrapolation to $\theta = 0°$		Extrapolation to $c = 0$	
	M_w (g·mol^{-1})	R_g (nm)	M_w (g·mol^{-1})	A_2 (cm^3·mol·g^{-2})
PS-CdS	(6.0 ± 0.1) x 10^6	51.0 ± 1.4	(6.1 ± 0.4) x 10^6	(5 ± 27) x 10^{-6}

4.3.1.2. Dynamic Light Scattering (DLS) of PS-CdS in $CHCl_3$

As SLS is an average intensity measurement, information relating to the Brownian motion of the particles in solution is lost. It is well known that molecules of diminished hydrodynamic volume have a tendency to move faster in solution with respect to larger molecules. This variance was undetectable with the SLS technique as the minute fluctuations in scattering intensity resulting from this motion were averaged out

over the data acquisition time (seconds). To obtain information on the distribution of sizes in the system we employed a LS technique that is run in the microsecond regime, and thus sensitive to the size-dependant motion of the particles in a given volume of solution.

Dynamic light scattering (DLS) measurements were conducted for all four concentrations of PS-CdS in chloroform, and the electric field correlation function was analyzed with the cumulant expansion as a function of delay time, τ. In the method of cumulants, the correlation function is expanded about a mean relaxation rate ($\overline{\Gamma}$) resulting in a polynomial expansion as a function of the delay time. For polydisperse, pointlike, isotropic particles without intermolecular interactions this expansion may be written as:[44]

$$|g(\tau)| = \exp[-\overline{\Gamma}\tau + (\mu_2 / 2!)\tau^2 + ...] \qquad \textbf{4.7}$$

In the analysis, μ_2 was obtained from the second moment, $\overline{\Gamma}$ was obtained from the first moment of the distribution relaxation rates and is related to the translational diffusion coefficient D_T through:

$$\overline{\Gamma} = D_T q^2 \qquad \textbf{4.8}$$

with the scattering vector q is defined as:

$$q = \frac{4\pi n}{\lambda}\sin\left(\frac{\theta}{2}\right) \qquad \textbf{4.9}$$

where n is the refractive index of the scattering liquid at the given wavelength of incident light, λ, and θ is the scattering angle. In order to correct for any possible interparticle interactions, D_T may be considered as a function of concentration:

$$D_T = D_0(1 + k_d c), \qquad \textbf{4.10}$$

yielding the diffusion coefficient at infinite dilution, D_0, which is obtained by extrapolation to zero concentration. The concentration coefficient, k_d is a measure of interparticle correlations[32,38] and the hydrodynamic radius, R_h, is a measure of the size of the particle and solvation layer(s), and is dependant on the motion of the particle in solution in the absence of interparticle effects (i.e., D_0) through the Stokes-Einstein equation:

$$R_h = \frac{kT}{6\pi\eta D_0} \qquad \textbf{4.11}$$

where k is the Boltzmann constant, T is the temperature, and η is the solvent viscosity.

This multi-angle, multi-concentration DLS study (Figure 4.5) yielded a diffusion coefficient at infinite dilution (D_0) via extrapolation to zero concentration as described in Table 4.4. Through the Stokes-Einstein equation, the radius of hydration (R_h) was obtained to be 13.6 nm (Table 4.4).

As k_d is a measure of interparticle correlations in a given solvent, a combination of thermodynamic (through A_2) and hydrodynamic interactions influence its value.[32,38] Positive values of k_d often denote repulsive interactions, whereas negative values are characteristic of attractive interactions. The slightly negative k_d obtained for PS-CdS in $CHCl_3$ (Table 4.4) suggests attractive interactions, providing further support for some aggregation of PS-CdS micelles in solution.

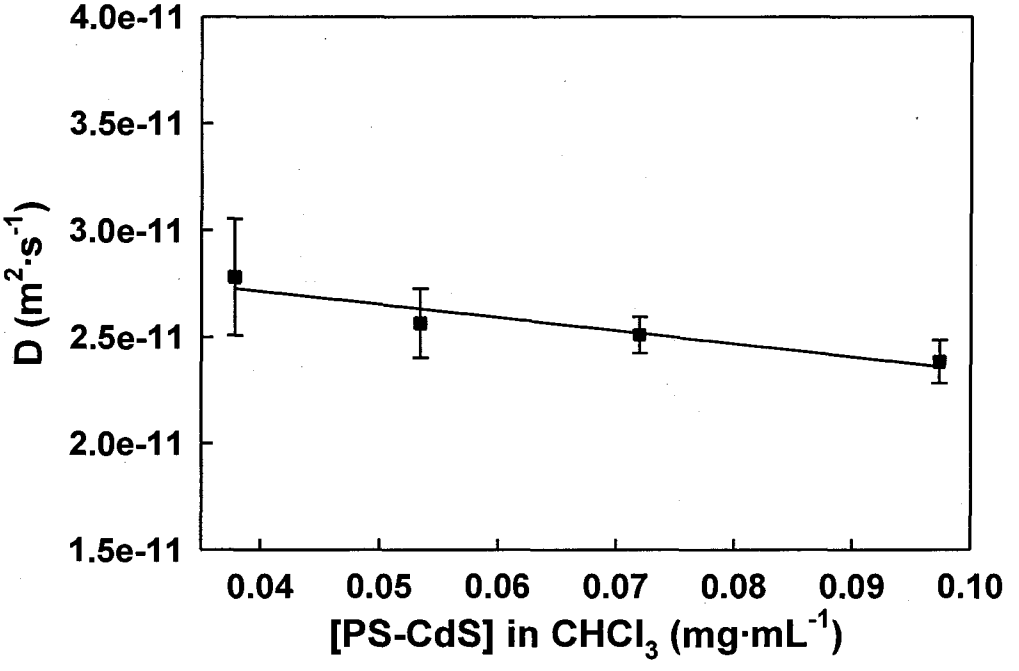

Figure 4.5. Concentration dependence of PS-CdS in $CHCl_3$ on the effective diffusion coefficient obtained via multi-angle dynamic light scattering. Error bars represent the standard deviation of triplicate measurements at each of the 6 angles at given concentration.

Table 4.4. Summary of DLS data obtained from multi-angle, multi-concentration cumulant expansion on PS-CdS in $CHCl_3$

	D_0 ($m^2 \cdot s^{-1}$)	R_h (nm)	μ_2/Γ^2	m ($m^5 \cdot g^{-1} \cdot s^{-1}$)	k_d ($cm^3 \cdot g^{-1}$)
PS-CdS	2.96×10^{-11}	13.6	0.21	-6.14×10^{-14}	-0.00207

The polydispersity of the sample can be elucidated from DLS several ways. The width of the decay rate distribution can be measured by the ratio of μ_2 to $\overline{\Gamma}^2$ which is obtained for each cumulant fit and therefore provides one measure of the size distribution.[45] If a sample is monodisperse, the width of the decay rate distribution would be negligible and the ratio $\mu_2 / \overline{\Gamma}^2$ would be zero. The ratio $\mu_2 / \overline{\Gamma}^2$ was averaged over the 18 cumulant fits obtained at the highest concentration studied, and found to be 0.21 indicating a significant size distribution. Cumulant analysis can not elucidate if more than one population of particle sizes was present in the solution, since a single distribution is assumed in this method.

To access the question of multiple populations, it was necessary to apply a more sophisticated program to analyze the autocorrelation functions obtained from PS-CdS solutions. Provencher's[46] CONTIN method not only gives the polydispersity of the entire sample, but can also detect multiple distributions of particle sizes. As a detailed description of the CONTIN method is well beyond the scope of this work, the interested reader is directed to other sources.[46,47] In essence, CONTIN is a statistical program that minimizes χ^2 to obtain a weighted function describing the distribution of relaxation rates in the sample,[48] yielding a distribution of diffusion coefficients and therefore a size distribution, without assuming a single distribution or a particular distribution shape.

The CONTIN distribution was obtained for each DLS profile. As it is not meaningful to combine individual CONTIN distributions, a single representative profile is provided as Figure 4.6. What is shown in this figure is the presence of two, or possibly three, populations of particles, with the larger populations (80 nm, 500 nm) showing average sizes significantly larger than the overall average value calculated from the

cumulant method (D_h = 27 nm), which assumed a single distribution. This confirms that aggregates were present in solution, with the more intense, smaller population centered at ~ 25 nm attributed to individual dispersed PS-CdS particles. The presence of larger aggregates sheds light on the significant polydispersity implied by the $\mu_2 / \overline{\Gamma}^2$ from the cumulant fits and the large M_w provided by the SLS measurements

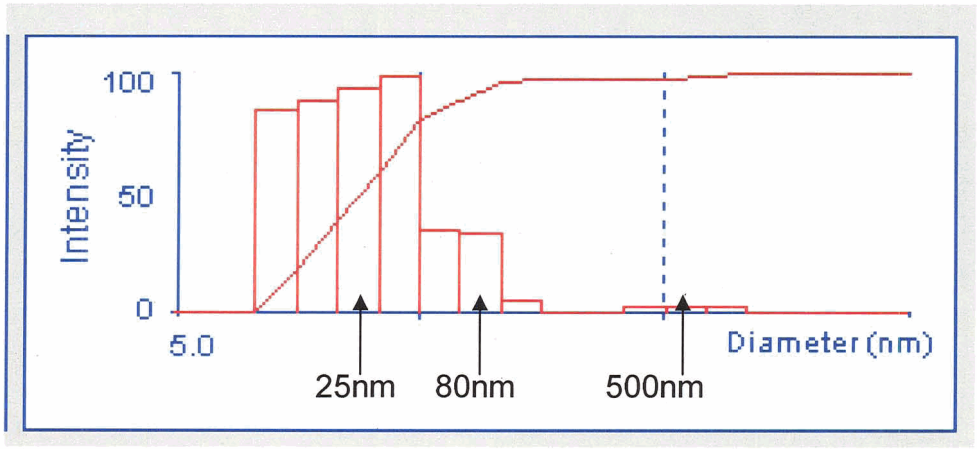

Figure 4.6. Representative CONTIN analysis of PS-CdS obtained at 0.1 mg/mL and a 75° angle of detection. Listed diameters given for the selected 'bin' was taken from the CONTIN data.

It is well known that the ratio R_g / R_h from a combination of SLS and DLS experiments gives useful information on the structure of colloidal systems.[49] For hard spheres, this ratio has a value of 0.775, whereas for starlike systems (Figure 1.2), R_g / R_h is ~ 1.10,[33] due to the relative increase in distance between the chain ends and the centre of mass of the particle with respect to the hydrodynamic radius. What was observed for PS-CdS in chloroform was a R_g / R_h of ~ 3.7, significantly higher than what was expected for either hard sphere, or star-like systems. R_g / R_h values in significant excess of ~ 1.10

are indicative of either anisotropic systems, for example cylindrical structures, or aggregates. In the present case we believe the presence of supermicellar aggregates (shown by CONTIN) caused the significant increase in R_g / R_h.

Since the ultimate destination of the PS-CdS is deposition at the air-water interface with PS-*b*-PEO, the presence of a small fraction of supermicellar aggregates was not expected to detrimentally influence our results. It is possible that supermicellar aggregates of PS-CdS will macroscopically phase separate at the interface rather than undergoing self-assembly with PS-*b*-PEO, but this is impossible to confirm

4.3.1.3. UV / Vis Absorption Spectroscopy

Recognizing that the effect of size quantization in the CdS may be employed to access the radius of the NP, we used UV / vis absorbance spectroscopy to study a solution of PS-CdS in chloroform. The UV / vis absorption spectrum (Figure 4.7) showed an absorption edge (λ_e) at 467 nm which correlated with a CdS core diameter ($2R_{CdS}$) of 4.1 nm through Henglein's empirical relationship[1] The size quantization effect for a CdS NP sample with a narrow size distribution shows a well defined absorbance maxima resulting from the excitonic transition in the semiconductor (For example Figure 1.3).[1] Though it was possible to extrapolate the absorption edge for the present sample, this well defined maximum was not observed. This is indicative of a relatively polydisperse NP size distribution, where the various sizes of NPs in the sample contribute to the overall electronic fingerprint of the sample resulting in a distribution of exciton states and a broad maximum. The absorption edge would reflect the larger NPs as they are less blue-shifted due by the quantum confinement effect.

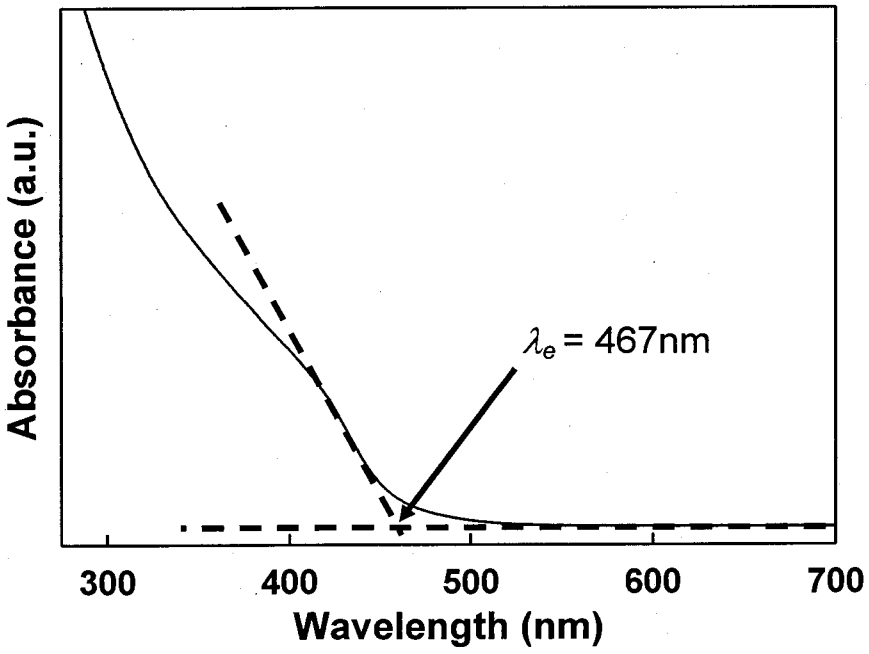

Figure 4.7. UV / Vis Absorbance spectrum of PS-CdS in $CHCl_3$ highlighting the absorbance edge (λ_e) of the CdS NP

4.3.1.4. Transmission Electron Microscopy (TEM)

To directly observe the size distribution of the CdS NPs, we turned to transmission electron microscopy (TEM). As described in Chapter 1, the polymer component of PS-CdS is relatively transparent to the accelerated electrons while the CdS cores are not, therefore providing good contrast and a discernable means to measure their size (Figure 4.8, inset). A considerable problem of using TEM to characterize polymer-coated NPs occurs in the preparation of the films to be imaged. Commonly, polymer films with thickness much greater than that of a monolayer are prepared and imaged by mechanically sectioning these thick films.[50] These sections are typically greater than a

monolayer in thickness, such that accurate resolution of individual cores is frustrated by overlapping of NPs in different focal planes. A tangential bonus of the present study was that we formed monolayers of these species in LB films which could be resolved with the TEM, although the resolution of the Hitachi H-700 was ~1 nm,[51] approaching the CdS core size. By direct observation of over 250 CdS cores taken from 5 LB films, the CdS NPs were found to have a mean diameter of 3.6 nm (standard deviation of 1.3 nm), shown in Figure 4.8. The relatively broad size distribution directly observed through TEM supports our claim that the lack of well-defined features in the UV/vis resulted from a relatively polydisperse sample of CdS NPs.

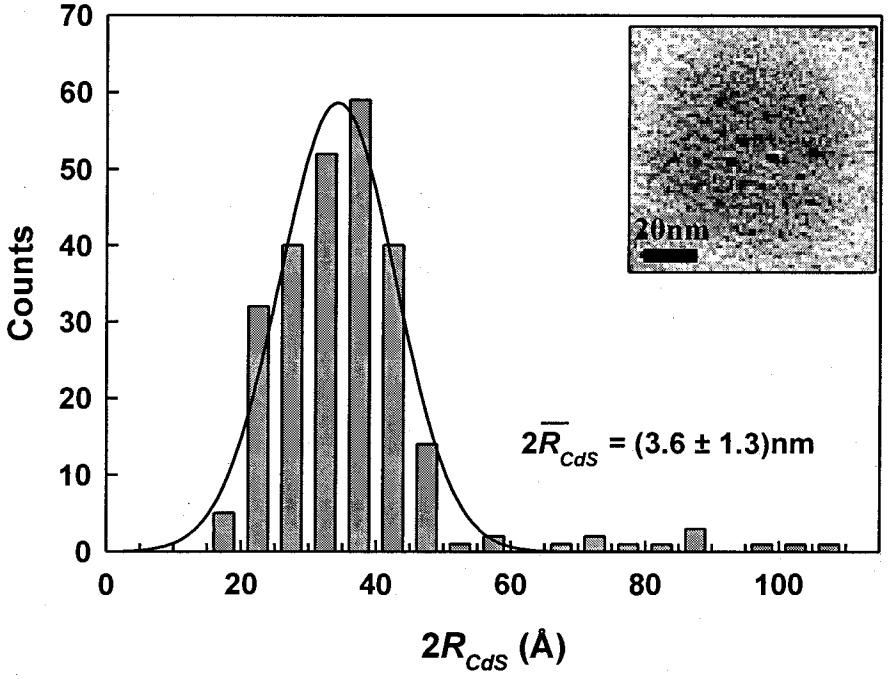

Figure 4.8. Diameter of CdS NPs directly observed via transmission electron microscopy (TEM). Inset is a typical TEM image of a PS-CdS structure after deposition at the air-water interface. Black dots are CdS NPs, and the grey areas are PS.

TEM evidence suggested that individual NPs were formed in each PS-*b*-PACd micelle core; however, to confirm this assumption we considered the molecular weight of the original PS-*b*-PACd micelle obtained through GPC-LALS and calculated the theoretical radius of the CdS NP to be formed. This calculation is strictly confirmatory, as various preparatory steps may change the aggregation number of the ionic core, however these are unlikely to significantly change the results. The aggregation number of PS-*b*-PACd diblock copolymers in the micelle was ~ 50 in THF (calculated from Table 4.2), suggesting ~ 1000 carboxylate groups in the micelle core ($x_{n,PAA}$ = 20). Considering a divalent Cd^{2+}, ~ 500 Cd^{2+} ions would reside within the ionomer core, yielding ~ 500 CdS groups upon exposure to H_2S. Assuming the bulk density of CdS (4.8 $g \cdot cm^{-3}$),[52] the average CdS core diameter ($2R_{CdS}$) would be ~ 3.6 nm, in good agreement with the UV / vis data and TEM evidence and suggesting a single CdS NP within the block copolymer stabilizing layer.

Based on UV / vis and TEM evidence on the CdS core, and GPC and LS measurements on the hybrid particle, it is possible to elucidate the structure of the PS-CdS, as described in Figure 4.9. The NP CdS radius was found to be ~ 2nm, and the average hydrodynamic size of a single PS-CdS was ~ 14 nm. As the thickness of the brush in given solvent is the difference between the hydrodynamic radius and the core, it was found to be ~ 12 nm thick. As such, the PS-CdS material is represented in Figure 4.9, revealing the various components of the structure.

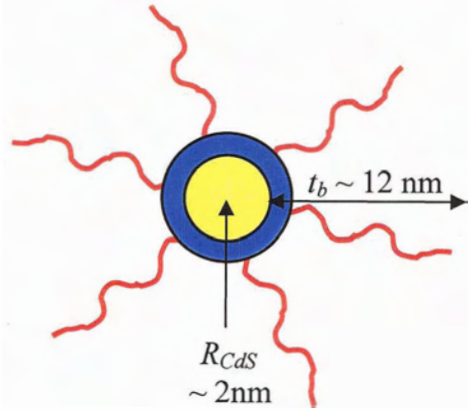

Figure 4.9. Cartoon representation of PS-CdS indicating the approximate dimensions of the components. Red = PS, blue = PAA and yellow is the CdS NP core. t_b represents the extension of the polymer brush in $CHCl_3$ (obtained from DLS data) from the CdS core (obtained from UV / vis and TEM).

4.3.2. Synergistic Self-Assembly of PS-CdS / PS-b-PEO Blends at the Air-Water Interface

Chapters 2 and 3 were dedicated to understanding the spontaneous self-assembly of pure PS-*b*-PEO diblock copolymers at the air-water interface. It was shown that by careful selection of the deposition conditions, i.e., concentration of the spreading solution, control was achieved over the predominance of certain surface features. In this chapter, we hope to take advantage of the interesting pattern-forming properties of pure PS-*b*-PEO at the air-water interface, in order to direct the assembly of PS-CdS particles within a polymeric matrix. To this end, we blended various quantities of PS-CdS with either of the two PS-*b*-PEO diblock copolymers described in the previous chapters. Deposition of the various blends from a chloroform solution at the air-water interface resulted in spontaneous self-assembly which was studied through AFM and $\pi - A$ isotherms.

The "PS-like" nature of PS-CdS results in athermal interactions between the NP building blocks and the PS blocks of PS-*b*-PEO (Flory-Huggins parameter $\chi = 0$), such that PS-CdS should interact preferentially with the PS component of the copolymer as the solvent evaporates, resulting in NP incorporation into the elevated PS aggregates at the interface (Scheme 4.2). As with the pure PS-*b*-PEO, we varied the spreading concentration to attempt control over morphology. Additionally, control over the PS-CdS weight fraction (f) in the blend provided a second adjustable variable that was used to achieve control over the morphology of the hybrid surface features.

Identifying the PS-CdS / PS-*b*-PEO surface features formed through a single self-assembly event at the air-water was a major focus of this thesis. AFM and TEM were combined to survey the morphologies, as the two disparate techniques are complimentary to one another. AFM was employed to identify mesoscopic features by accessing the topology of the LB film, whereas TEM was used to access the nanoscopic features, namely the location of the CdS NPs within the polymer matrix. A combination of experimental evidence points to synergistic self-assembly between the PS-CdS and PS-*b*-PEO components, resulting in hybrid features that are fundamentally different from those obtained from self-assembly of the individual "pure" components.

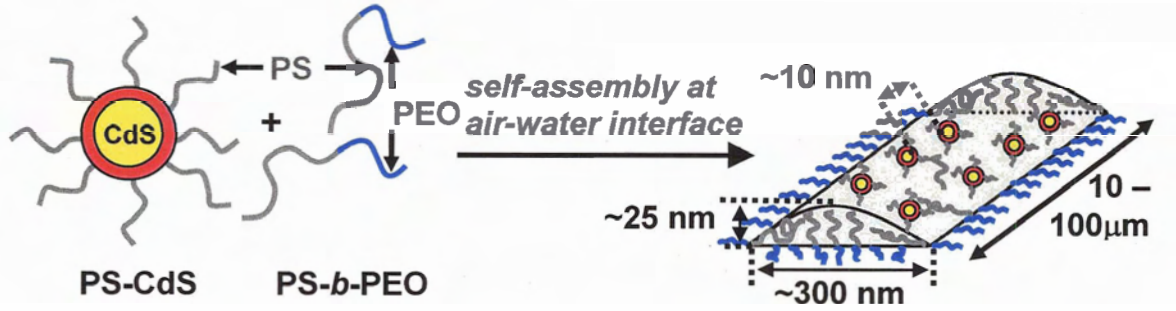

Scheme 4.2. Spontaneous self-assembly of PS-CdS / PS-*b*-PEO blends deposited at the air-water interface

4.3.2.1. Overview of the Surface Morphologies

When PS-CdS was deposited from $CHCl_3$ at the air-water interface without blending with amphiphilic PS-*b*-PEO, the result was a polydisperse population of circular islands with diameters between ca. 0.1 to 2 μm and heights up to 100 nm; the height, polydispersity, and circular morphology of these aggregates is attributed to the "PS-like" nature of PS-CdS, and the driving force for these hydrophobic particles to minimize unfavourable contacts with the water surface. In general, the diameter and heights of the surface features were greater when deposited from more concentrated solution. Figure 4.10 is a representative image of a PS-CdS LB film exemplifying the polydisperse nature of the circular structures. TEM evidence (inset) proved the existence of the CdS NPs within the elevated "PS-like" material at the interface.

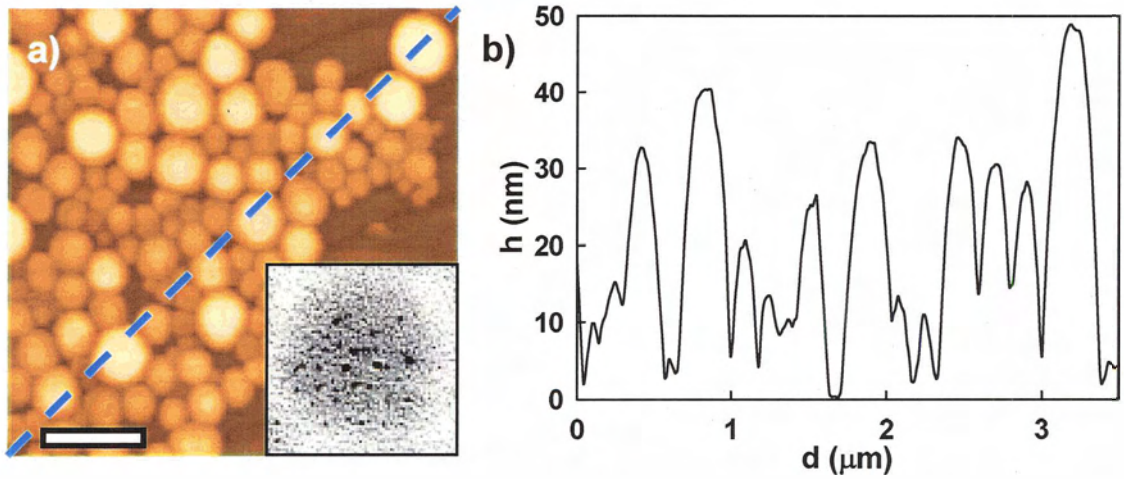

Figure 4.10. Representative image of a PS-CdS film spread from a 1.0 mg/mL $CHCl_3$ spreading solution deposited at the air-water interface and transferred via the LB method at 5 mN/m. (a, colour) is the AFM image of the LB film with the inset (black and white) showing a TEM image of an identical LB film. AFM scale bar represents 1 μm, TEM edge length is 100 nm. The height profile of (a) along the blue dashed line is given in (b).

Interestingly, interfacial self-assembly of the blended components yielded a range of unique features that were not found from deposition of either pure PS-CdS or pure PS-*b*-PEO solutions, suggesting synergistic, spontaneous organization of the amphiphilic copolymer and hydrophobic PS-CdS components. AFM and TEM images of representative structures formed from 1:3 blends of PS-*b*-PEO(11.4%) and PS-CdS (PS-CdS weight fraction, $f = 0.75$) at different spreading solution concentrations are shown in Figure 4.11. Unlike PS-CdS alone, these blends formed 1D (lateral aspect ratios >> 1) and pseudo-1D assemblies, including branched nanowires (Figure 4.11a and c) and extremely long aggregates which we term nanocables (Figure 4.11b and d). The widths of these nanowires and nanocables (300 ± 50 nm) are remarkably uniform for structures of various lengths, although the feature lengths are polydisperse, ranging from 2 - 20 μm for branched nanowires and up to 100 μm for nanocables. We note that the widths of

nanowires and nanocables from self-assembly of PS-CdS / PS-*b*-PEO blends are a factor of ~2 greater than the widths of spaghetti aggregates formed from PS-b-PEO(11.4%) alone (~160nm), suggesting incorporation of PS-CdS into the polymer features. In addition, the mean height of the 1D assemblies in Figure 4.11 is 21 ± 2 nm as determined by AFM, higher than pure PS-*b*-PEO(11.4%) spaghetti aggregates (~12 nm) and fairly close the hydrodynamic diameter of PS-CdS measured by dynamic light scattering in chloroform (27 nm). These data are consistent with a monolayer of PS-CdS NPs stabilized at the air-water interface within a laterally patterned PS-*b*-PEO brush structure, as depicted in Scheme 4.2.

Confirmation of NP organization within the polymeric surface features observed through AFM was provided by TEM (Figure 4.11c and d), which clearly shows that CdS NPs are uniformly dispersed along the branched nanowires and nanocables, with average interparticle spacings of ~ 10 nm. The lateral packing of NPs within the 1D superstructures is therefore quite dense; assuming an NP monolayer, each micron length of nanowire or nanocable is estimated to contain ~ 10^3 NPs. This combination of AFM and TEM imaging highlights the unique structural hierarchy of these NP / polymer composite features, which combine NP organization on a combination of vastly disparate length scales via a single self-assembly step (Scheme 4.2). Compared to block copolymer-directed NP self-assembly in the bulk,[23] where localization of block junctions at domain interfaces limits characteristic feature sizes to the dimensions of the polymer chains, we have demonstrated that the current strategy of interfacial self-assembly allows access to NP / polymer features with dimensions orders of magnitude larger than a polymer chain, since copolymer junctions are localized at the air-water interface, such

that features arise from the lateral organization of many chains arranged in a brush-like manner.

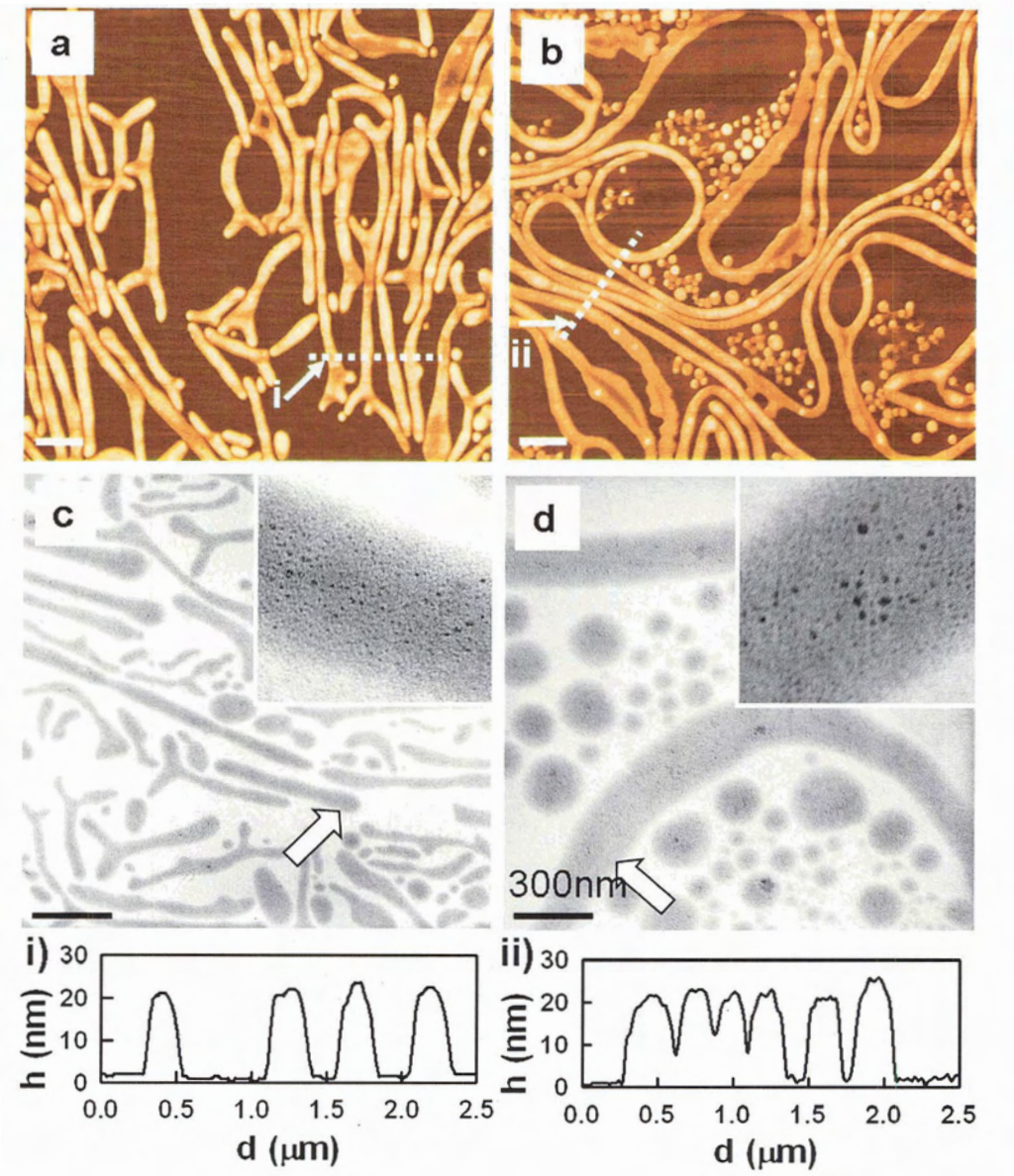

Figure 4.11. Representative AFM (a, b) and TEM (c, d) images of PS-CdS / PS-b-PEO(11.4%) hierarchical assemblies formed via deposition at the air-water interface. Spreading solution concentrations and PS-CdS weight fractions of the blends, f were: a, c) 2.0 mg/mL, f = 0.75; and b, d) 1.0 mg/mL, f = 0.75, respectively. Film transfer occurred at 2.0 mN/m and all scale bars represent 1 μm unless otherwise indicated. Insets are magnified versions of indicated regions of TEM images (arrows) with edge lengths of (c) 500 nm and (d) 250 nm.

4.3.2.2. Morphological Control Via Deposition Conditions

In previous chapters, it was established that varying the concentration of the PS-*b*-PEO spreading solution affords control over the predominance of certain surface features.[25,27] That same thinking was applied to the PS-CdS / PS-*b*-PEO blends in an effort to tune the resultant structures. In addition to this, we also varied the PS-CdS weight fraction f between 0 and 1, to attempt further control over morphology. Interestingly, the two PS-*b*-PEO samples showed very similar trends with respect to the predominant morphology at a given concentration and blend composition. Certain surface features were more predominant than others and as such were classified, and statistical analysis was performed on their dimensions. Two major surface features were classified: uniformly thick 1D and branched features (For example; Figures 4.12c and 4.12e) and non-uniformly thick 1D features with periodically-spaced nodules along the long axis (For example; Figure 4.12a).

By varying the composition of deposited PS-CdS / PS-*b*-PEO blends for a given spreading solution concentration, we were able to tune the morphologies of the resulting NP / polymer assemblies (Figure 4.12). Although mixtures of features are generally observed for a given set of conditions, some clear trends are easily discernable. At the lowest PS-CdS weight fraction (f = 0.25), the 1D structures with nodules were the predominant surface feature (Figure 4.12a). Conversely at the highest micelle weight fraction (f = 0.75), there was no evidence of any nodules, and the 1D structures were uniformly thick for both PS-*b*-PEO copolymers (Figure 4.12e). An additional feature at this composition was the formation of nanorings incorporated into long nanocables (highlighted in Figure 4.14), which was a prominent morphology for PS-CdS / PS-*b*-

PEO(18.9%) blends at high spreading solution concentrations and f = 0.75, and rarely observed under other deposition conditions. The radius of these rings was generally < 2μm and had wall dimensions commensurate with the nanocables. The intermediate composition (f = 0.50) showed morphologies with characteristics between those of the f = 0.25 and f = 0.75 blends, as some nodules were noted, especially in the case of the PS-CdS / PS-*b*-PEO(11.4%) blend, with a large number of highly branched structures in the case of PS-CdS / PS-*b*-PEO(18.9%) (Figure 4.12e).

By varying the concentration of the blend spreading solution, additional morphological control was achieved (Figures 4.13 and 4.14), independent of the blend composition. In the concentrated regime, much longer aggregates with proportionately more branch points were noted, whereas in the dilute regime there was an increased in the predominance of dot-like structures and smaller irregular aggregates. These trends are revealed in the representative AFM images of PS-CdS / PS-*b*-PEO(11.4%) and PS-CdS / PS-*b*-PEO(18.9%) LB films described in Figures 4.13 and 4.14, which illustrate the effect of spreading concentration and blend composition on the morphologies. What is clearly shown is the predominance of less extended, more 'dot-like' aggregates in the dilute regime. This trend in morphology as a function of concentration may have implications on the mechanism to which the patterns form, or break down, which will be addressed in Section 4.3.2.5.

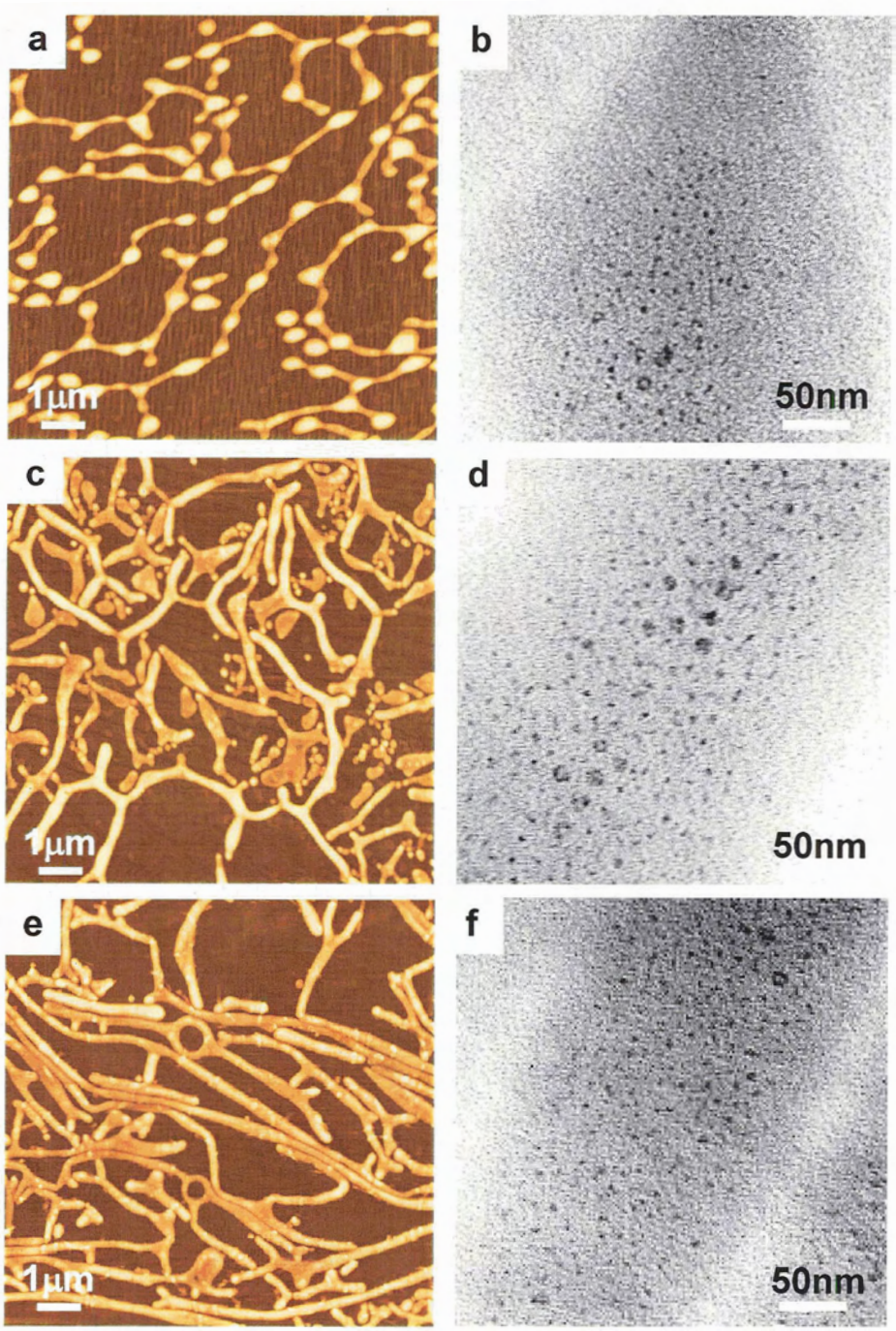

Figure 4.12. Representative AFM (a,c,e) and TEM (b,d,f) images of PS-CdS / PS-*b*-PEO(18.9%) LB films formed via deposition at the air-water interface from a 2.0mg/mL spreading solution and transfer at 5 mN/m. Micelle weight fractions were (a,b) 0.25; (c,d) 0.50; and (e,f) 0.75. TEM images are magnified versions of (b) a nodule showing local density of CdS NPs in the nodule, and (d,f) nanocables showing uniform distribution of NPs throughout the 1D structure.

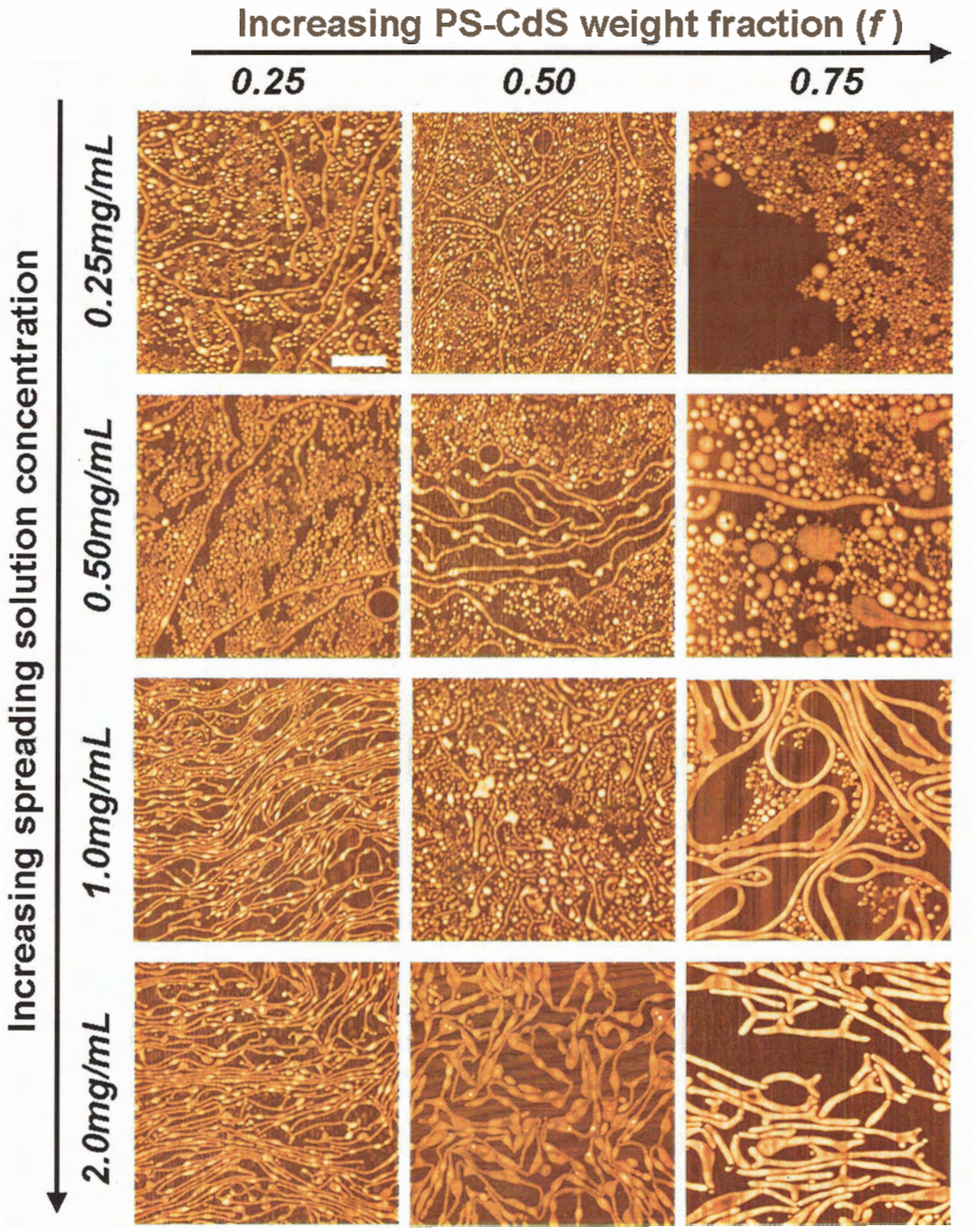

Figure 4.13. Representative AFM images of PS-CdS / PS-*b*-PEO(11.4%) LB films transferred at 2.0 mN/m. Scale bar represents 2 μm, and is consistent for all images. Mean dimensions for typical surface features from each concentration / composition are provided in Table 4.5.

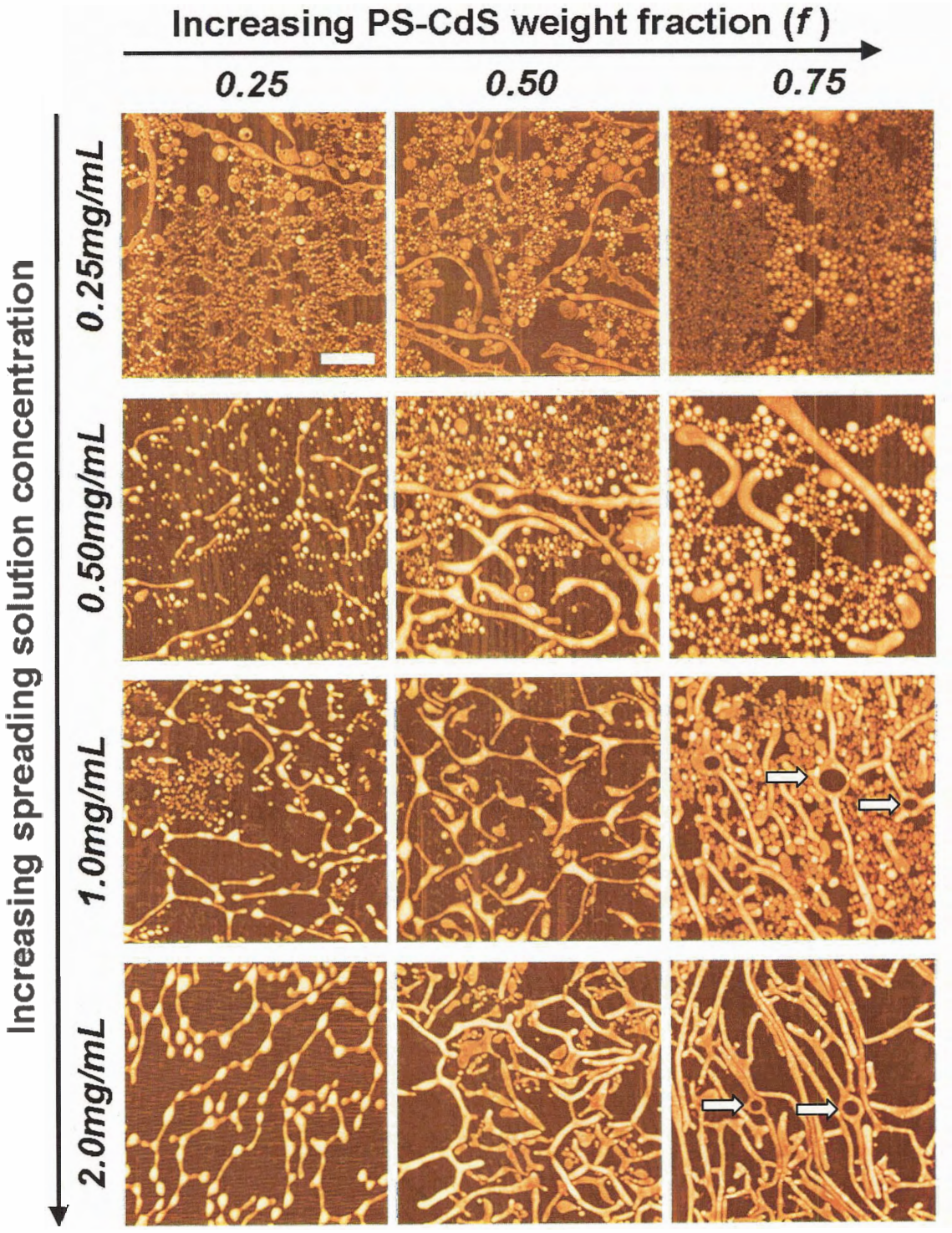

Figure 4.14. Representative AFM images of PS-CdS / PS-*b*-PEO(18.9%) LB films transferred at 5.0 mN/m. Scale bar represents 2 μm, and is consistent for all images. Mean dimensions for typical surface features from each concentration / composition are provided in Table 4.6. Arrows highlight nanorings described in the text.

Table 4.5. Mean dimensions of the surface aggregates obtained via spontaneous self-assembly of PS-CdS / PS-*b*-PEO(11.4%) at the air-water interface and observed through AFM on LB films. *h* represents the height and *w* the width of the given surface feature

Spread conc. (mg/mL)	*f*	thick wire		nodule		connector	
		h (nm)	*w* (nm)	*h* (nm)	*w* (nm)	*h* (nm)	*w* (nm)
0.25	0.25	-	-	19 ± 3	280 ± 50	11 ± 2	170 ± 30
	0.50	-	-	19 ± 4	290 ± 40	11 ± 1	150 ± 30
	0.75	-	-	-	-	-	-
0.50	0.25	-	-	19 ± 4	320 ± 40	11 ± 2	170 ± 30
	0.50	-	-	20 ± 3	340 ± 40	11 ± 1	180 ± 30
	0.75	20 ± 2	420 ± 50	-	-	-	-
1.0	0.25	-	-	18 ± 2	240 ± 50	12 ± 2	140 ± 20
	0.50	20 ± 2	300 ± 40	19 ± 3	290 ± 50	10 ± 2	160 ± 20
	0.75	21 ± 2	280 ± 50	-	-	-	-
2.0	0.25	-	-	20 ± 3	260 ± 60	12 ± 1	150 ± 20
	0.50	19 ± 4	320 ± 60	-	-	-	-
	0.75	21 ± 2	320 ± 40	-	-	-	-

*Error represents the standard deviation of at least 25 surface features

Table 4.6. Mean dimensions of the surface aggregates obtained via spontaneous self-assembly of PS-CdS / PS-*b*-PEO(18.9%) at the air-water interface and observed through AFM on LB films. *h* represents the height and *w* the width of the given surface feature

Spread conc. (mg/mL)	*f*	thick wire		nodule		connector	
		h (nm)	*w* (nm)	*h* (nm)	*w* (nm)	*h* (nm)	*w* (nm)
0.50	0.25	-	-	27 ± 3	360 ± 40	15 ± 2	180 ± 30
	0.50	24 ± 3	430 ± 80	-	-	-	-
	0.75	28 ± 3	560 ± 90	-	-	-	-
1	0.25	-	-	26 ± 2	320 ± 40	16 ± 2	170 ± 20
	0.50	28 ± 5	380 ± 110	-	-	-	-
	0.75	29 ± 5	370 ± 80	-	-	-	-
2	0.25	-	-	26 ± 4	310 ± 60	15 ± 2	180 ± 30
	0.50	24 ± 5	310 ± 40	-	-	-	-
	0.75	27 ± 3	320 ± 30	-	-	-	-

*Error represents the standard deviation of at least 25 surface features

**There were not enough surface features at 0.25mg/mL to determine their mean dimensions

4.3.2.3. Mechanical Stability of PS-CdS / PS-b-PEO Surface Features

Our technique for patterning inorganic NPs within a polymer matrix should offer a general self-assembly method for composite structures with potential applications in photonics, electronics, and sensing. Along with providing a dielectric medium for the photoluminescent CdS NPs, which itself could eventually be tuned for future photonic applications, the PS matrix imparts significant mechanical resilience, with the assemblies being kinetically "locked" by the glassy nature of PS at room temperature following evaporation of chloroform. This stability is a significant achievement over much of the previous work on 1D NP assembly at the air-water interface where wire-like organizations of NPs were unstable on compression and expansion.[11] Our NP / polymer composites were found to be quite stable to changes in the LB surface pressure. For example, several PS-CdS / PS-*b*-PEO(18.9%) (f = 0.75, concentration = 2.0mg/mL) Langmuir films were transferred at π = 2.0, 5.0, 10 and 20 mN/m, and the observed morphologies had no discernable dependence on the transfer pressure. Even the distances in the inter-aggregate spacings showed no significant differences, a point which is related to the steepness of the $\pi - A$ isotherm considered in Section 4.3.2.4. To further study the mechanical resilience to stress, multiple compression / expansion cycles were performed on PS-CdS / PS-*b*-PEO Langmuir films. Figure 4.15 shows the result of 4 repeated compression / expansion cycles, where in each cycle the Langmuir film was compressed to π = 20 mN/m, equilibrated for 10 minutes and subsequently expanded back to 0 mN/m. LB transfer at π = 5.0 mN/m after the fourth cycle yielded surface aggregates that were very similar to those deposited after a first compression, suggesting the effect of mechanical stresses from multiple cycles was minimal. One marked

difference noted from AFM images obtained after just one compression to $\pi = 5.0$ mN/m was that some of the aggregates were 'puckered' in places, where the 1D structure seemed to fold up on itself, and a few fracture points were noted as highlighted in Figure 4.15. These features are what would be expected of a thin glassy polymer ($T < T_g$) under appreciable stress. This anisotropic stress from the compressing paddles caused the polymer to either fold or crack, depending on the local geometry in an effort to relieve the stress. Although folds and cracks were not isolated, the average surface features suffered neither of these failures, suggesting significant structural integrity

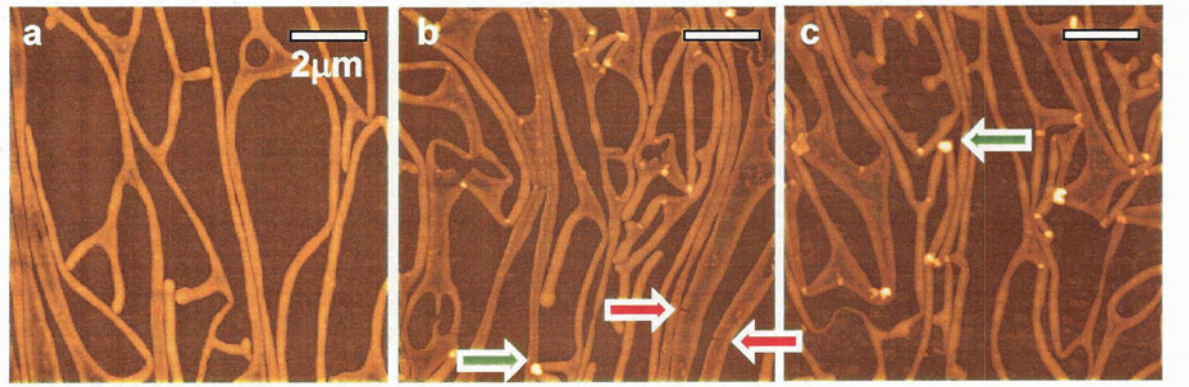

Figure 4.15. AFM images of PS-CdS / PS-*b*-PEO(18.9%) ($f = 0.75$, concentration = 2.0 mg/mL) blend before (a) and after (b and c) four consecutive compression (to 20 mN/m) and expansion (to 0 mN/m) cycles and subsequent LB transfer at 5.0 mN/m. Green arrows highlight puckered regions, and red arrows highlight fractures

A further indication of the resilience of these hierarchical structures came from a classic obstacle encountered in many TEM investigations. As it was necessary to prepare relatively thin Formvar substrates to achieve high-quality TEM images, this caused them to be inherently unstable when exposed to the stresses of the TEM chamber. High vacuum and electron beam heating commonly caused the Formvar substrate to rupture, carrying whatever was on it with it and ruining that section of the grid. Interestingly, these rupture events seemed to occur less frequently on samples that had significantly long 1D aggregates. In the TEM image on Figure 4.16, a PS-CdS / PS-*b*-PEO aggregate has been heated above its T_g by the electron beam; a tear developed in the Formvar substrate exerted a tensile stress on the nanocable. The nanocable is seen to undergo obvious extension without rupture, a property attributable to the viscoelastic nature of the heated PS matrix.

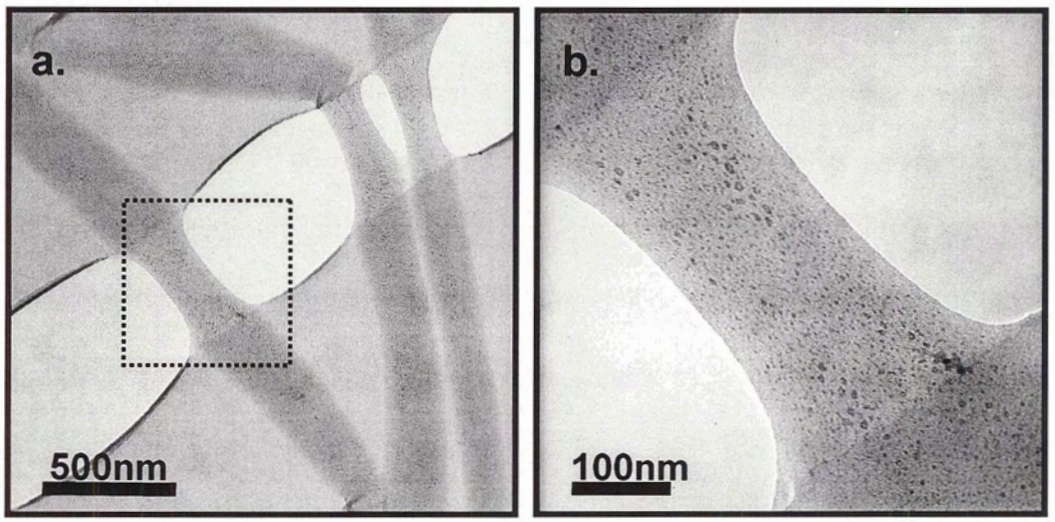

Figure 4.16. TEM image of (a) PS-CdS / PS-*b*-PEO(18.9%) (f = 0.75, deposition concentration = 2.0 mg/mL) demonstrating the mechanical stability of the nanocable aggregates; which are elongated without failure when subjected to a tensile stress from the torn Formvar substrate. (b) is a magnified version of a, about the dotted square.

4.3.2.4. Surface Pressure – Area Isotherms

Previous chapters have shown that $\pi - A$ isotherms reveal pertinent information which complement the microscopy data for pure PS-*b*-PEO diblock copolymers. The same approach was taken for PS-CdS / PS-*b*-PEO blends at the air-water interface. As each of the five spreading solution concentrations had five blend compositions, and replicate trials were necessary to establish the reproducibility of the procedure, data acquisition was a significant undertaking, but proved to be quite useful.

Representative isotherms and the respective limiting areas (A_0's) for PS-CdS / PS-*b*-PEO(11.4%) (Figure 4.17a) and PS-CdS / PS-*b*-PEO(18.9%) (Figure 4.18a) blends reveal some interesting trends. For both blend types, the addition of an increasing weight fraction (*f*) of the "PS-like" PS-CdS caused the isotherms to increasingly resemble pure PS homopolymer;[53,54] the onset to the brush regime occurred at lower and lower π values and became increasingly steep, reflective of the inelastic nature of glassy PS; for the PS-CdS / PS-b-PEO(18.9%) blends, where a plateau region was observed in the isotherm of the pure copolymer, the increasing addition of PS-CdS to the surface aggregates resulted in the PEO phase transition becoming more and more hindered (Figure 4.18a). The steep increase in π upon compression for high loadings of PS-CdS explains why no noticeable difference in the inter-aggregate spacing of a $f = 0.75$ blend was observed by AFM for different transfer pressures (as noted in a previous section); the inelastic nature of the film in this regime resulted in a significant increase in π with minimal decrease in trough area.

The increasing contribution of the PS domain to the $\pi - A$ isotherm also made analysis of the PEO pancake regime as a function of PS-CdS addition impossible, since the plateau region became increasingly obscured as more PS-CdS was added to the

blends. To access this regime it would be necessary to employ a significantly more hydrophilic PS-*b*-PEO diblock in the blend, where the PEO phase transition would be clearly discernable over a range of added PS-CdS. The relatively long PEO block would, however, have consequences on the novel self-assembly properties observed in these more hydrophobic systems, resulting in a decreased tendency for the system to form interesting 1D structures – a chemical Catch-22.

The limiting area of the blends A_0 was determined as shown in Figures 4.17a and 4.18a for various blend compositions. If the limiting area of one component was independent of the amount of the other component, we would expect a linear relationship between A_0 and the blend composition, as depicted as the dashed line in the inset of Figures 4.17a and 4.18a. What was actually observed for every spreading concentration was a non-linear relationship (Figures 4.17b and 4.18b), where the A_0 values for the blends were significantly higher than the hypothetical linear plot. Along with the AFM data discussed above, this non-linearity suggests that the self-assembly of PS-CdS / PS-*b*-PEO blends was synergistic, in that the presence of one component appeared to influence the conformation and surface area of the other. However, as discussed below and in previous chapters, the surface conformation of PS-*b*-PEO may also be affected by its spreading concentration, due to chain entanglement effects, independent of possible interactions with PS-CdS; this effect must also be taken into account when interpreting the trends in A_0.

Interestingly, for all blends and at all spreading concentrations, A_0 showed an initial increase to $f = 0.25$ and then a nonlinear decrease as the PS-CdS content was further increased (Figures 4.17b and 4.18b). The initial increase in A_0 was found to be

more significant, and the overall A_0 values were found to be higher, when blend solutions were cast in the dilute regime (i.e $\leq$ 0.25mg/mL). We attribute the observed maxima in A_0 to two competing effects of increasing the PS-CdS content in the blend solutions: first, there is a "dilution effect", where an increase in the PS-CdS content at constant overall concentration will result in dilution of the copolymer in solution; this can effect an overall increase in the mean molecular area of the PS-*b*-PEO at the water surface, as established in the preceding chapters. Next, we have seen that an increase PS-CdS content will also make the blends more "PS-like", affecting a decrease in the limiting area. The competition between these effects results in the observed maxima: this explains why the maxima are most prominent at lower spreading concentrations, since the dilution effect is most important below a critical concentration of PS-*b*-PEO, where a decrease in chain entanglements can effect a conformational change at the surface.

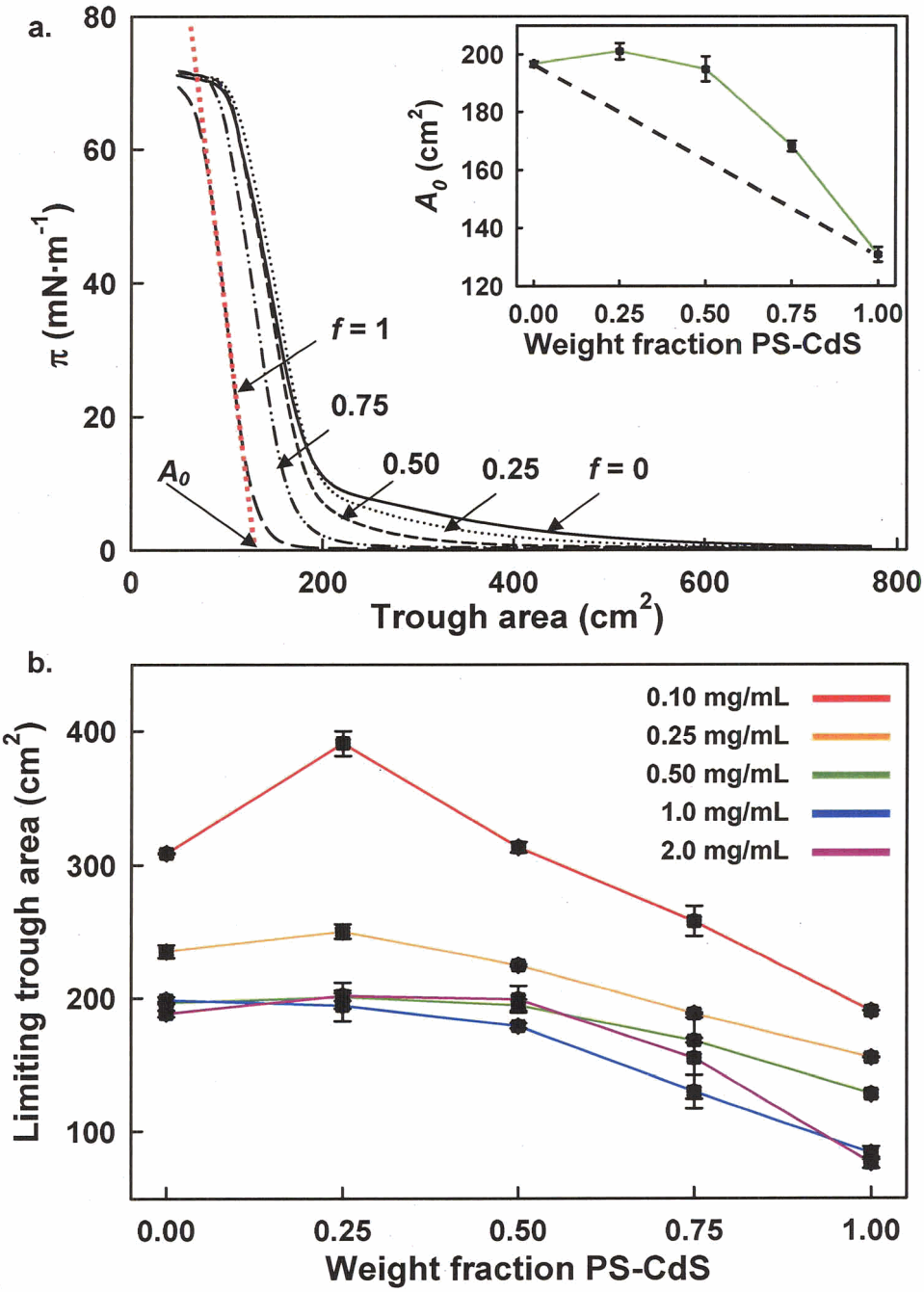

Figure 4.17. Langmuir isotherms of PS-CdS / PS-*b*-PEO(11.4%) blends at the air-water interface. (a.) Representative isotherm of 0.50mg/mL blends of variable PS-CdS weight fraction (f), extrapolated red line reveals the limiting mean trough area (A_0) at $f = 1.0$ for example. Inset describes the hypothetical linear for an independent assembly mechanism described in the text. (b) gives the A_0 at given spreading solution concentration indicated in the figure. Error bars represent the difference between duplicate measurements

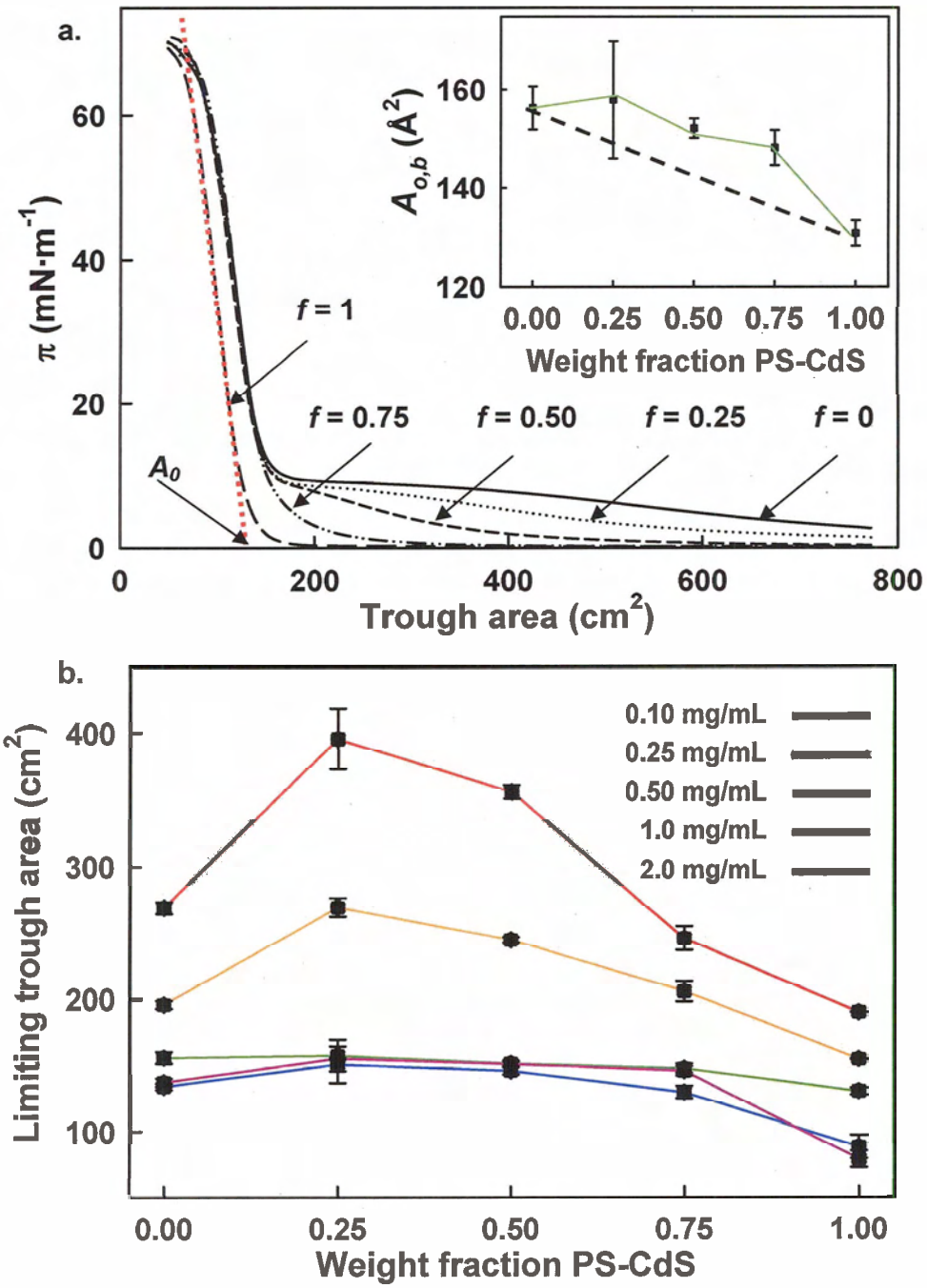

Figure 4.18. Langmuir isotherms of PS-CdS / PS-*b*-PEO(18.9%) blends at the air-water interface. (a.) Representative isotherm of 0.50mg/mL blends of variable PS-CdS weight fraction (f), extrapolated red line reveals the limiting mean trough area (A_0) at $f = 1.0$ for example. Inset describes the hypothetical linear for an independent assembly mechanism described in the text. (b) gives the A_0 at given spreading solution concentration indicated in the figure. Error bars represent the difference between duplicate measurements

4.3.2.5. Mechanism of Pattern Formation

As was the case for the pure PS-*b*-PEO diblock copolymer, the various low-dimensional PS-CdS / PS-*b*-PEO features are seen to represent a range of kinetically-trapped states, where structure evolution and ultimate "freezing" of the system are both the result of solvent evaporation. The PS-CdS / PS-*b*-PEO blends have an additional level of complexity from that of the pure diblock in that two distinct components are involved in self-assembly. Nevertheless, we here build on some of the interesting trends that were introduced in Section 4.3.2.2, and further develop the dewetting mechanism in an attempt to explain the spontaneous formation of these low-dimensional surface features.

The dewetting mechanism as described in Chapter 3 proceeds from initial hole formation in a homogenous and continuous film of chloroform and the polymer components at the surface of water, with accumulation of mass in the rim of the expanding hole and eventual contacting with other growing holes to form a cellular-like matrix. In pure PS-*b*-PEO, these networks were found to break down into long spaghetti aggregates, driven by an increase in PEO adsorption, which subsequently underwent morphology transformations into dots or rings and chains, depending on the extent of chain entanglements (Chapters 2 and 3). Several images of PS-CdS / PS-*b*-PEO blend films also showed a polygonal matrix pattern for the most concentrated spreading solutions, suggesting a early "snapshot" of the initial dewetting step; similar dewetting patterns were not observed at lower concentrations, since the morphologies will evolve more rapidly from the initial stages with decreasing chain entanglements. For example, Figure 4.19b shows a polygonal pattern formed from a PS-CdS / PS-*b*-PEO(18.9%) blend

deposited from a 2.0 mg/mL spreading solution that is unequivocally similar to dewetting of melt PS from a solid substrate (Figure 4.19a).

In the case of PS-CdS / PS-b-PEO blends, it is proposed that the $CHCl_3$-swollen walls of the initial polygonal network contain a homogenous mixture of PS-CdS and PS-b-PEO: these networks will then break into branched and 1D composite features containing NPs, similar to the evolution of spaghetti described for pure copolymer in the previous chapter. When the concentration of PS-CdS in the composite features is relatively low (e.g. $f = 0.25$), it appears that further solvent evaporation induces phase separation between the PS-CdS and the PS brush of the PS-*b*-PEO component, resulting in the formation of nodules where the PS-CdS becomes localized (For example, Figure 4.12a); this phase separation is an entropy-driven process, similar to the autophobic phase separation of colloidal PS brushes from a PS homopolymer, and is attributed to a loss in conformational entropy with interpenetration of the PS-CdS and PS-*b*-PEO brushes. It is likely that the same driving force for phase separation exists at higher PS-CdS content (e.g. $f = 0.75$), except the high concentration of PS-CdS in the solvent-swollen composite features results in restricted lateral mobility of the NPs; for this reason, nodule formation cannot occur before the structures are locked in by vitrification, resulting in the various 1D composite features containing a uniform distribution of CdS NPs.(For example, Figure 4.11b)

The general trend observed for the dependence of feature morphologies on the concentration of spreading solution in the PS-CdS / PS-b-PEO systems is an increase in the amount of dots and polydisperse island structures, and a consequential decrease in the amount of branched and 1D features (Figures 4.13 and 4.14), as the spreading

concentration decreases. The presence of polydisperse islands at lower spreading concentrations suggests a separate phase of PS-CdS, indicating that the two components will undergo phase separation on larger length scales, beyond the formation of trapped nodules, as the extent of chain entanglements is decreased. This further emphasizes the kinetic nature of the observed composite features, while illustrating the opportunities for tuning self-assembled hybrid structures through kinetic control.

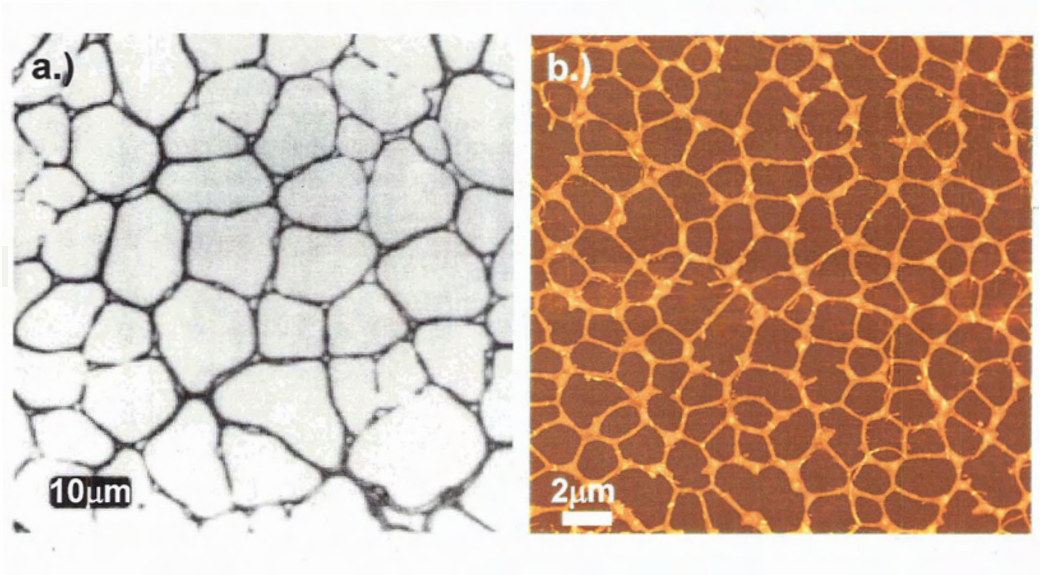

Figure 4.19. Polygon patterns formed from a) a 10 nm thick PS film (Mw = 660 kg/mol) on a silanized silicon wafer before Rayleigh instabilities lead to the formation of droplets imaged through TEM[55] and b) a LB film of PS-CdS / PS-*b*-PEO(18.9%) (f = 0.50) cast from a concentrated (2.0mg/mL) spreading solution at the air-water interface and transferred at π = 5.0 mN/m.

Finally, we proposed that dewetting can also explain the formation of the novel morphology of hybrid nanorings incorporated into hybrid nanocables, which was an interesting and predominant surface feature for the PS-CdS / PS-*b*-PEO(18.9%) ($f = 0.75$; concentration = 2.0 and 1.0 mg/mL) blend. It was noted that several of the images obtained for this sample contained small planar aggregates along the length of a nanocable, in addition to the nanoring/nanocable features, where an elevated rim was present at the edge of a relatively flat surface, similar to a continent as described by Devereaux and Baker.[27] It appears that these flat surfaces tend to rupture in a secondary dewetting process, followed by the radial growth of a hole. Depending on the abundance of solvent, and the rate of evaporation, the expanding rims will freeze in at various stages in their development from a relatively flat continent. Figure 4.20 provides a pictorial representation of this secondary dewetting process resulting in nanorings of various radii and at various stages of their development. The trend in Figure 4.20i $\rightarrow$ iii provides evidence for this morphological evolution where (i) is vitrified at a relatively early stage in the eventual development of a mature nanoring (iii). The topology profiles show that the height of rings formed after the initial rupture (i. ~15 nm) are significantly reduced from the height of a mature nanoring (iii. 25-30 nm), indicative of a dewetting-like rupture and growth mechanism, where hole growth adds material (height) to the rim as it matures.

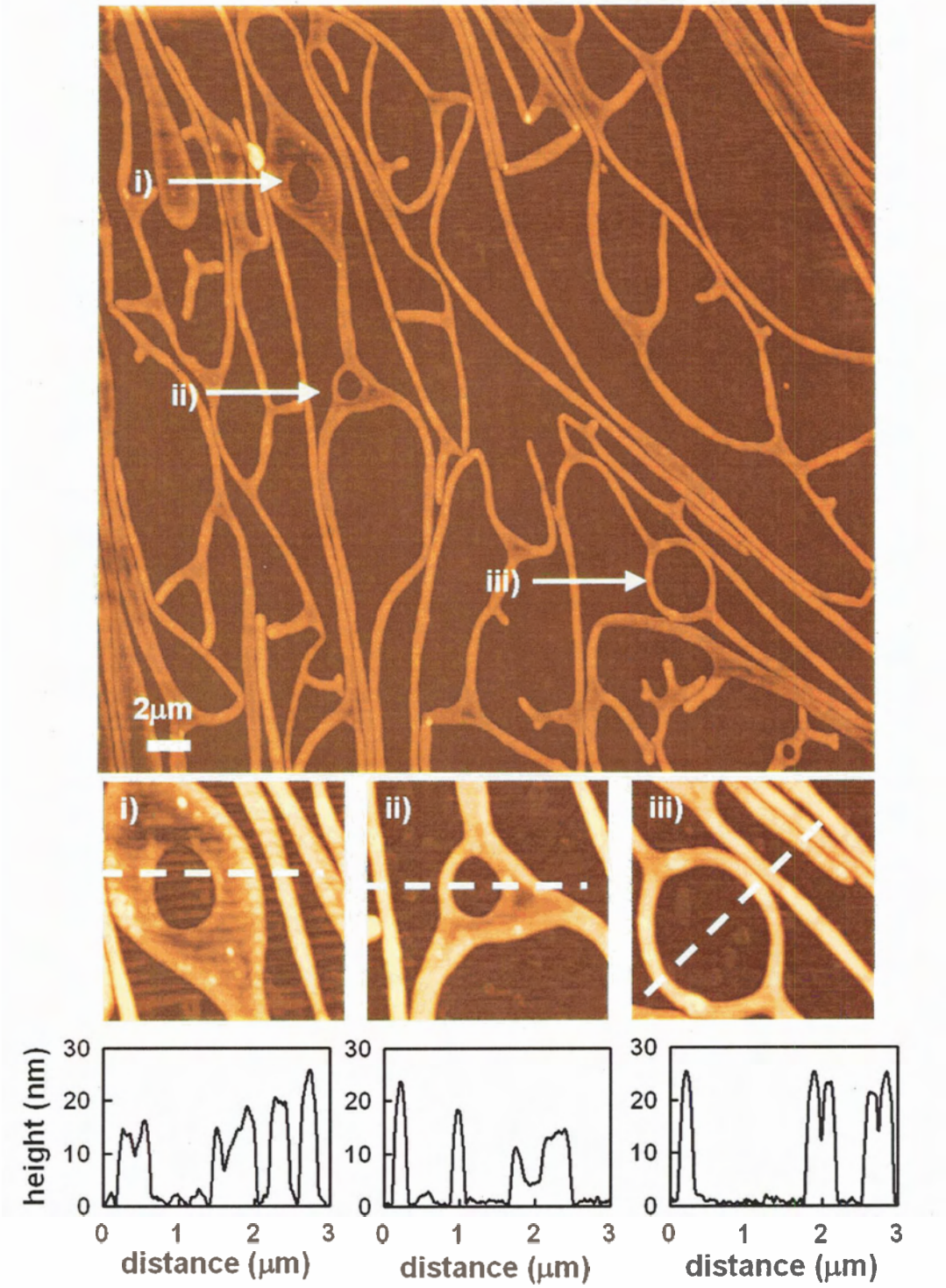

Figure 4.20. AFM image of a PS-CdS / PS-*b*-PEO(18.9%) ($f = 0.75$) LB film deposited from a 2.0 mg/mL $CHCl_3$ solution at the air-water interface and transferred at 5.0 mN/m, highlighting the formation and evolution of nanorings. Arrows indicate the respective magnified images and height profiles (i → iii) described in the text.

4.4. Conclusions

We have demonstrated a novel method of patterning polymer-stabilized CdS NPs into hierarchical structures through synergistic self-assembly with PS-*b*-PEO diblock copolymers at the air-water interface. CdS NPs were successfully patterned into uniformly thick 1D nanowires and nanocables with an even distribution of NPs throughout the structure, and also into 1D nanowires and nanocables with NP-containing nodules evenly spaced along the long axis. Additionally, pseudo-1D hybrid structures were formed including branched nanowires and nanorings. These mesoscopic features were observed via AFM of the LB films formed at the interface. TEM evidence complimented the AFM topology, revealing the nanoscopic organization of the CdS NPs throughout the polymer matrix.

We were able to demonstrate control over morphology by simply varying the deposition conditions at which the PS-CdS / PS-*b*-PEO blends were deposited at the air-water interface. Increasing the weight fraction of the PS-CdS yielded uniformly thick 1D and branched structures with a fairly even distribution of NPs throughout the structure. Conversely, at low micelle weight fractions, structures containing nodules of localized CdS NP density were the more predominant surface feature. Additional morphological tunability was afforded through control of the spreading solution concentration. At increased spreading concentrations, the aggregates were found to be longer than were observed in the dilute regime, where an increased predominance of dot-like structures and polydisperse circular islands were found. Our AFM data also suggested that the mechanism of formation for these interesting hybrid assemblies begins with dewetting of the evaporating polymer solution from the air-water interface.

To further study the Langmuir films, we conducted a detailed investigation of $\pi - A$ isotherms of the PS-CdS / PS-*b*-PEO blends under all deposition conditions. At all deposition concentrations, an unusual maximum was found in plots of the limiting area vs. PS-CdS weight fraction in the blend. This was explained by a competition between two effects as more PS-CdS is added: dilution of the PS-*b*-PEO on one hand, which will promote PEO adsorption and increase the limiting area, and increasing the PS-like behaviour of the blend on the other, which will lower the limiting area.

4.5. References

(1) Henglein, A. *Chem. Rev.* **1989,** *89*, 1861.

(2) Steigerwald, M. L.; Brus, L. E. *Acc. Chem. Res.* **1990,** *23*, 183.

(3) Weller, H. *Angew. Chem., Int. Ed. Engl.* **1993,** *32*, 41.

(4) Alivisatos, A. P. *Science* **1996,** *271*, 933.

(5) Collier, C. P.; Vossmeyer, T.; Heath, J. R. *Annu. Rev. Phys. Chem.* **1998,** *49*, 371.

(6) Murray, C. B.; Kagan, C. R.; Bawendi, M. G. *Annu. Rev. Mater. Sci.* **2000,** *30*, 545.

(7) El-Sayed, M. A. *Acc. Chem. Res.* **2001,** *34*, 257.

(8) Sapra, S.; Nanda, J.; Sarma, D. D. *In Proc. of the Plenary 90th Session of Indian Science Congress: Bangalore* **2003**, 3.4.

(9) Wang, C.-W.; Moffitt, M. G. *Langmuir* **2004,** *20*, 11784.

(10) Chung, S.-W.; Markovich, G.; Heath, J. R. *J. Phys. Chem. B.* **1998,** *102*, 6685.

(11) Sear, R. P.; Chung, S.-W.; Markovich, G.; Gelbart, W. M.; Heath, J. R. *Phys. Rev. E.* **1999,** *59*, 6255.

(12) Ge, G.; Brus, L. *J. Phys. Chem., B.* **2000,** *104*, 9573.

(13) Rabani, E.; Reichman, D. R.; Geissler, P. L.; Brus, L. E. *Nature* **2003,** *426*, 271.

(14) Martin, C. P.; Blunt, M. O.; Moriarty, P. *Nano Lett.* **2004,** *4*, 2389.

(15) Shah, P. S.; Jr., M. B. S.; Stowell, C. A.; Lim, K. T.; Johnston, K. P.; Korgel, B. A. *Adv. Mater.* **2003,** *15*, 971.

(16) Shah, P. S.; Novick, B. J.; Hwang, H. S.; Lim, K. T.; Carbonell, R. G.; Johnston, K. P.; Korgel, B. A. *Nano Lett.* **2003,** *3*, 1671.

(17) Böker, A.; Lin, Y.; Chiapperini, K.; Horowitz, R.; Thompson, M.; Carreon, V.; Xu, T.; Abetz, C.; Skaff, H.; Dinsmore, A. D.; Emrick, T.; Russell, T. P. *Nature Mater.* **2004,** *3*, 302.

(18) Tang, Z.; Kotov, N. A. *Adv. Mater.* **2005,** *17*, 951.

(19) Shenhar, R.; Norsten, T. B.; Rotello, V. M. *Adv. Mater.* **2005,** *17*, 657.

(20) Lopes, W. A.; Jaeger, H. M. *Nature* **2001,** *414*, 735.

(21) Bockstaller, M. R. L., Y.; Margel, S.; Thomas, E. L. *J. Am. Chem. Soc.* **2003,** *125*, 5276.

(22) Chiu, J. J. K., B. J.; Kramer, E. J.; Pine, D. J. *J. Am. Chem. Soc.* **2005,** *127*, 5036.

(23) Lin, Y.; Böker, A.; He, J.; Sill, K.; Xiang, H.; Abetz, C.; Li, X.; Wang, J.; Emrick, T.; Long, S.; Wang, Q.; Balazs, A.; Russell, T. P. *Nature* **2005,** *434*, 55.

(24) Heath, J. R.; Kuekes, P. J.; Snider, G. S.; Williams, R. S. *Science* **1998,** *280*, 1716.

(25) Cheyne, R. B.; Moffitt, M. M. *Langmuir* **2005,** *21*, 5453.

(26) Baker, S. M.; Leach, K. A.; Devereaux, C. E.; Gragson, D. E. *Macromolecules* **2000,** *33*, 5432.

(27) Devereaux, C. A.; Baker, S. M. *Macromolecules* **2002,** *35*, 1921.

(28) Cox, J. K.; Yu, K.; Constantine, B.; Eisenberg, A.; Lennox, R. B. *Langmuir* **1999,** 15, 7714.

(29) Cox, J. K.; Yu, K.; Eisenberg, A.; Lennox, R. B. *Phys. Chem. Chem. Phys* **1999,** *1*, 4417.

(30) Green, P. F.; Limary, R. *Adv. Colloid Interface Sci.* **2001,** *94*, 53.

(31) Moffitt, M.; Vali, H.; Eisenberg, A. *Chem. Mater.* **1998,** *10*, 1021.

(32) Moffitt, M.; Eisenberg, A. *Macromolecules* **1997,** *30*, 4363.

(33) Moffitt, M. Ph. D. thesis (McGill University) **1997.**

(34) Moffitt, M.; McMahon, L.; Pessel, V.; Eisenberg, A. *Chem. Mater.* **1995,** *7*, 1185.

(35) Wang, C.-W. M.Sc. thesis (University of Victoria) **2005.**

(36) Gauthier, S.; Duchesne, D.; Eisenberg, A. *Macromolecules* **1987,** *20*, 753.

(37) Desjardins, A.; Eisenberg, A. *Macromolecules* **1991,** *24*, 5779.

(38) Desjardins, A.; Ven, T. G. M. V. d.; Eisenberg, A. *Macromolecules* **1992,** *25*, 2412.

(39) Zhong, X. F.; Varshney, S. K.; Eisenberg, A. *Macromolecules* **1992,** *25*, 7160.

(40) Personal Communication; Eisenberg Research Group (McGill University) **2004.**

(41) Yang, D.; Li, L.; Wang, C. *Mater. Chem. Phys.* **2004,** *87*, 114.

(42) Zimm, B. H. *J. Chem. Phys.* **1948,** *16*, 1099.

(43) Cowie, J. M. G., *Polymers: Chemistry and Physics of Modern Materials*. 2nd Edition ed., Nelson Thornes, 1991.

(44) Zhang, L.; Barlow, R. J.; Eisenberg, A. *Macromolecules* **1995,** *28*, 6055.

(45) *Brookhaven Instruments Instruction Manual for BI-9000AT Digital Autocorrelator*, Brookhaven Instrument Corporation, 2003

(46) Provencher, S. W. *Comput. Phys. Commun.* **1982,** *27*, 213.

(47) Brown, W., *Monographs on the Physics and Chemistry of Materials*, Oxford Science Publications, 1996

(48) Hellweg, T.; Brulet, A.; Sottmannc, T. *Phys. Chem. Chem. Phys.* **2000,** *2*, 5168.

(49) Burchard, W. *Adv. Polym. Sci.* **1983,** *48*, 1.

(50) Wang, C.-W.; Moffitt, M. *Chem. Mater.* **2005**.

(51) Gowen, B., Personal Communication. December **2004**.

(52) *CRC Handbook of Chemistry and Physics, 77th Ed.*, ed. Lide, D. R.; CRC Press Ltd., 1996.

(53) Kumaki, J. *Macromolecules* **1986,** *19*, 2258.

(54) Kumaki, J. *Macromolecules* **1988,** *21*, 749.

(55) Reiter, G. *Langmuir* **1993,** *9*, 1344.

Chapter 5

Conclusions, Contributions to Original Knowledge and Suggestions for Future Work

5.1. Conclusions and Contributions to Original Knowledge

This section provides a summary of the notable findings discussed in the thesis emphasizing contributions to original knowledge. The organization of Section 5.1 mirrors that of the thesis and is accordingly divided into two sub-sections. Section 5.1.1 summarizes Chapters 2 and 3, and thus describes the relevant aspects of the spontaneous self-assembly and interfacial behaviour of two PS-*b*-PEO diblock copolymers. Section 5.1.2 reviews the novel, nonlithographic technique developed to pattern polymer stabilized CdS NPs into low-dimensional, hierarchical structures via synergistic self-assembly with PS-*b*-PEO at the air-water interface.

5.1.1. PS-b-PEO Self-Assembly and Behaviour at the Air-Water Interface

Chapter 2 introduced the interfacial behaviour and self-assembly of a relatively hydrophobic PS-*b*-PEO (11.4 wt% PEO) diblock copolymer at the air-water interface. Langmuir films produced via deposition from chloroform solutions at the interface were transferred to glass substrates via the Langmuir-Blodgett (LB) technique and imaged using atomic force microscopy (AFM). Monolayers prepared under identical conditions were also characterized at the air-water interface via Langmuir compression isotherms. The effects of spreading solution concentration on surface features, compressibility, and limiting mean molecular area were determined, revealing several interesting trends that had not previously been reported for PS-*b*-PEO diblock copolymers at the air-water interface. Spreading solutions $\geq$ 0.50 mg/mL resulted almost exclusively in dot and spaghetti morphologies, with no observed continent features, which have been commonly found in more hydrophobic systems.[1,2] For lower spreading solutions, $\leq$ 0.25 mg/mL, we

observed a large predominance of two new surface morphologies, nanoscale rings and chains.[3]

To further probe the surface structure and interfacial behaviour of the aggregates, we conducted the first study on the influence of spreading concentration on surface pressure (π) - area (A) isotherms. It was shown that the isotherms also exhibited a unique dependence on the spreading solution concentration, with limiting mean molecular areas (A_0) and isothermal compressibilities (C_m) of PS-*b*-PEO monolayers increasing below a critical concentration of spreading solution. A_0 was shown to increase below a critical spreading solution concentration ($\leq$ 0.25 mg/mL) suggesting a greater contribution from the PEO blocks in this regime. These results suggest that PS chain entanglement prior to solvent evaporation plays an important kinetic role in the extent of PEO adsorption at the air-water interface and in the morphologies of the resulting self-assembled surface aggregates.

Recognizing the novelty of our findings reported in Chapter 2, we decided to further investigate this spreading solution concentration effect on the surface structure and interfacial behaviour of an additional PS-*b*-PEO diblock copolymer. It is known that when the weight fraction of the PEO block is > 15%,[4] the first-order pancake – brush phase transition is discernable in the $\pi - A$ isotherm as a plateau or pseudoplateau at $\pi \sim$ 10 mN/m, where the PEO blocks become detached from the interface and desorb into the subphase. The presence of two distinct phases permits independent resolution of both the pancake and brush conformations of the aggregates, data that was unattainable from isotherms of the more hydrophobic PS-*b*-PEO copolymer investigated in Chapter 2. By studying a PS-*b*-PEO diblock copolymer that was above this critical threshold of PEO

content,[4] we were able to investigate and compare the spreading solution concentration dependence on both the pancake and brush conformations, a major focus of Chapter 3.

The 18.9wt%-PEO sample studied in Chapter 3 demonstrated the same concentration dependence in the brush regime, where the limiting brush area ($A_{0,b}$) increased significantly below a critical spreading solution concentration ($\leq$ 0.25 mg/mL). Interestingly, the A_0 in the pancake regime ($A_{0,p}$) was shown to be unaffected by the spreading concentration, despite the corresponding increase in $A_{0,b}$. Multiple compression / expansion isotherms were employed to further probe the effect of spreading solution concentration on PS-*b*-PEO surface structure. Hysteresis in the brush regime was studied for both PS-*b*-PEO(18.9%) ($\Delta A_{0,b}$) and for PS-*b*-PEO(11.4%) (ΔA_0), whereas hysteresis in the pancake regime was only studied for PS-*b*-PEO(18.9%) ($\Delta A_{0,p}$), since no pancake phase was observed from the isotherms of PS-*b*-PEO(11.4%). This novel investigation revealed that $\Delta A_{0,,b}$ followed the same trend as $A_{0,b}$, increasing below a critical spreading solution concentration ($\leq$ 0.25 mg/mL). Conversely $\Delta A_{0,p}$ showed the opposite effect, decreasing below a critical spreading concentration ($\leq$ 0.25 mg/mL). The combination of compression isotherm and compression / expansion hysteresis data provided suggested that PS-*b*-PEO aggregates cast from spreading solutions $\leq$ 0.25 mg/mL were less densely-packed, leading to increased PEO adsorption underneath the vitrified PS matrix.

A major contribution of the present work pertained to the mechanism driving the formation of the 1D and pseudo-1D structures in amphiphilic block copolymer monolayers at the air-water interface, a phenomenon that has been poorly understood. These structures are often described as two-dimensional (2D) block copolymer micelles,

and yet the analogy with three-dimensional (3D) block copolymer micelles is a poor one, since the various morphologies observed in 3D are clearly thermodynamic in nature, whereas we have shown that the morphologies observed in 2D represent kinetically trapped states. By re-examining surface features observed in PS-*b*-PEO(11.4%) Langmuir films, in the context of the isotherm data described in Chapters 2 and 3, we were able to suggest that dewetting of polymer solutions at the air-water interface may, in fact, be the genesis behind the formation of these unique surface structures. We proposed that morphology evolution in films of hydrophobic PS-*b*-PEO begins with a continuous and homogenous layer of chloroform and the hydrophobic diblock at the water surface, stabilized by the positive spreading coefficient of chloroform on water. As chloroform evaporation occurs, the short-range interactions between the film and water become increasingly less attractive, and the film eventually dewets, with holes developing in the copolymer / chloroform film. The resultant holes, surrounded by raised rims of transferred material, grow until contact with adjacent expanding holes results in a network of interconnected rims which may further break down into less interconnected spaghetti structures, and then into dots (in the case of PS-*b*-PEO(18.9%)) or dots, chains, and rings (in the case of PS-*b*-PEO(11.4%)).

5.1.2. Hierarchical Polymer / Nanoparticle Surface Features via Synergistic Self-Assembly at the Air-Water Interface

The pattern-forming properties of the PS-*b*-PEO diblock copolymers described in Chapters 2 and 3 were exploited in the nonlithographic patterning of polymer-stabilized CdS nanoparticles (PS-CdS), the theme of Chapter 4. This novel approach was

accomplished by blending various quantities of PS-CdS with either of the PS-*b*-PEO copolymers and subsequent deposition at the air-water interface. Interestingly, interfacial self-assembly of the blended components yielded a range of unique features that were not found from deposition of either pure PS-CdS or pure PS-*b*-PEO solutions, suggesting synergistic, spontaneous organization of the amphiphilic copolymer and hydrophobic PS-CdS components. As with the pure PS-*b*-PEO LB films, PS-CdS / PS-*b*-PEO blend films showed multiple morphologies at a given deposition, however some clear trends were easily discernable. The mesoscopic surface features probed by AFM exhibited a high predominance of uniformly thick nanowires and nanocables at increased micelle weight fraction (f), and non-uniform nanowires and nanocables with nodules along the length of the features at reduced f. The morphologies were again tunable through deposition concentration where a greater number of 1D and branched structures (nanowires and nanocables) were observed at increased spreading concentrations, compared to the dilute regime, where more dots and polydisperse circular islands were observed. The uniformly thick 1D features, along with the nodules of nonuniform features, were all significantly taller and thicker than structures obtained from the respective pure PS-*b*-PEO, suggesting PS-CdS incorporation into these domains. This was confirmed through TEM, which showed a uniform distribution of the CdS NPs throughout the extended nanowires and nanocables, and localized NP density in the nodules of the nonuniform structures. This complimentary combination of AFM and TEM microscopy studies highlighted the organization on multiple length scales (i.e. structural hierarchy) obtained from a single self-assembly event at the air-water interface.

A detailed investigation of the $\pi - A$ isotherms of PS-CdS / PS-*b*-PEO blends revealed some interesting trends, and provided further support in favour of a synergistic assembly mechanism. It was observed that the limiting area in the brush regime did not follow a linear relationship as a function of f, suggesting that the presence of one component influenced the surface conformation of the other, as one would expect from the obvious synergistic nature of the self-assembly confirmed by AFM.

As with Chapter 3, Chapter 4 also looked at the driving force and mechanism of self-assembly at the interface. Similar to the pure copolymer case, interfacial dewetting of the evaporating polymer blend solution was suggested to be central to the formation of the hierarchical NP/polymer surface features. This conclusion was highlighted by AFM images bearing a striking similarity to classical dewetting features, where cellular-like networks were observed in films obtained at high spreading solution concentrations.

5.2. Suggestions for Future Work

As with Section 5.1, this section is divided into two subsections focusing on the two central aspects of the thesis. Section 5.2.1 discusses suggestions for future research on the self-assembly, interfacial structure and behaviour of amphiphilic diblock copolymers, the topics of Chapters 2 and 3. Section 5.2.2 suggests some future considerations into the formation and properties of the hybrid NP / polymer aggregates described in Chapter 4.

5.2.1. Suggested Research on Diblock Copolymer Self-Assembly and Behaviour at the Air-Water Interface

The work described in Chapters 2 and 3 focused on the self-assembly and interfacial behaviour of two PS-*b*-PEO diblock copolymers. Through a combination of $\pi - A$ isotherm and AFM studies, we developed a model that was consistent with the results of the respective experiments, concerning the position and conformation of the PS and PEO blocks within the surface aggregates as a function of spreading solution concentration. The essential feature of our model was that aggregates formed from concentrated spreading solutions contained a significant amount of desorbed PEO underneath the PS aggregate. As this work comprised the first study on the influence of spreading solution concentration on $\pi - A$ isotherms, it would be interesting to see if similar, or different, trends are found for PS-*b*-PEO diblock copolymers of variable molecular weights and relative block lengths. Additionally, a study into this spreading concentration effect on other types of non-ionic amphiphilic diblock copolymers (for example polystyrene-*block*-poly(alkyl acrylates)[5-7] would be of fundamental interest.

An interesting study that could verify our proposed model would be neutron reflectometry measurements of PS-*b*-PEO Langmuir films at the air-water interface cast from variable spreading concentrations. Neutron reflectometry has proven to be quite useful in structural investigations of amphiphilic diblock copolymers at the air-water interface. In this experiment, differences in the neutron scattering profiles of hydrogen versus deuterium nuclei are responsible for contrast, as such it is necessary to either have a deuterated subphase, or deuterated PEO block. It is known that use of a deuterated subphase provides favourable contrast,[8] therefore this method would be suggested. In

this experiment, the incipient neutron beam grazes the air-deuterated water interface at low angles and is reflected or scattered to an extent depending on the distribution of undeuterated PEO centres at the interface and in the subphase, therefore allowing a profile of polymer segment density as a function of depth to be determined with Angstrom resolution.[9] The majority of studies that employed neutron reflectometry for structural determination of PS-*b*-PEO monolayers were used to elucidate details concerning the nature of the pancake-brush phase transition.[8] To our knowledge, neutron reflectometry has never been coupled to the influence of spreading concentration in amphiphilic diblock copolymer surface features. If our model is correct, an increased amount of desorbed PEO formed from concentrated spreading solutions could be confirmed by segment density profiles determined from neutron reflectometry.

As one of the major contributions of the present work was the suggestion that dewetting of evaporating diblock copolymer solutions from the air-water interface may be the genesis of various surface feature morphologies in these systems, it is logical that additional experiments be considered that address this effect. The easiest, and perhaps most informative, experiment would be to vary the casting solvent or temperature of the subphase in order to control the rate of solvent evaporation via control over the vapour pressure. Raising the temperature of the subphase should raise the vapour pressure of the solvent and presumably allow access to earlier stages of morphological evolution since the solvent would be more quickly removed, and the polymer would thus vitrify at an earlier time. The same effect would apply to solvents with a higher vapour pressure at room temperature, as they too would likely lead to earlier 'snapshots' of morphology evolution. If one were to consider a change in the solvent however, it would be necessary

to ensure that the spreading coefficient remains strongly positive, and that the block copolymer does not aggregate before deposition—both essential features of the present system.

A basic driving force for this work is the quest for methodologies that permit efficient access to unique and controllable patterns. A relatively easy and potentially interesting twist on interfacial PS-*b*-PEO self-assembly described in this thesis would be to increase the humidity at the Langmuir trough, which could be easily accomplished by boiling a flask of pure water near the trough (i.e. inside the plexiglass box that houses the trough). As the chloroform evaporates, the chloroform-air interface will rapidly cool as heat is transferred into the vaporized chloroform molecules; this temperature gradient will induce condensation of water droplets from the atmosphere within the evaporating polymer solution. Similar 'breath figures'[10] have been shown to efficiently pattern three dimensional, close packed, inverse opaline structures by simply passing a moist air stream through a relatively thick volatile solvent containing polystyrene homopolymer.[11] If employed at the air-water interface with PS-*b*-PEO solutions, breath figure formation coupled to PEO spreading and chain entanglements may produce novel surface structures that are distinct from those we have obtained via solution dewetting in a relatively dry atmosphere.

5.2.2. Suggested Research on Patterning and Properties of Polymer / Nanoparticle Surface Features at the Air-Water Interface

The work described in Chapter 4 combined the pattern-forming properties of the PS-*b*-PEO diblock copolymers investigated in Chapters 2 and 3 with polymer-stabilized

photoluminescent CdS NPs (PS-CdS), in order to direct the organization of NPs into hierarchical structures via a single self-assembly step at the air-water interface. As the morphologies of the observed hybrid surface features are strongly dependent on the presence of the PS-*b*-PEO diblock copolymer, many of the suggestions in the previous section (e.g. variation in solvent, temperature, humidity) may also be applied to the PS-*b*-PEO / PS-CdS blend system in an effort to enhance control over the morphology of potentially functional structures.

Control over the nanoscopic organization of the CdS NPs within a mesoscopic polymeric superstructure has been demonstrated. The need to further control the spatial distribution and alignment of these aggregates will be essential to their implementation into functional devises. Ultimately, novel research into various integration methodologies leading to increased control at the at the micro- macroscopic length scales will be necessary. The multiple compression / expansion studies discussed in the context of the mechanical stability of these hierarchical aggregates may be amenable to alignment of NP / polymer nanowires and nanocables. It is possible that multiple compression / expansion cycles would cause 1D aggregates to follow the path of least resistance on the trough, leading to a high occurrence of nanowires and nanocables orientated parallel to the barriers on the trough, the source of the stress. Obvious alignment was not apparent in our preliminary studies due to the many branch points, nanorings, etc. in this system. These irregular structural elements caused the system to be remain locally disordered over the cycles, so that the film remained macroscopically disordered. Further investigations into this method should be considered when more control of aggregate morphology is achieved at the mesoscopic length scale.

A second possibility that may prove useful toward macroscopic organization of 1D NP / polymer surface features would be to employ an external force at the initial self-assembly step. A potential route to achieving this would be to synthesize magnetic NPs within a similar polymer brush to that of PS-CdS and subsequently direct their interfacial assembly with PS-*b*-PEO using an applied magnetic field. These NPs may be synthesized in an analogous way to the procedure presented in this thesis, however, substituting magnetic material in place of the CdS core. A related technique would be to synthesize a core-shell NP where the synthesis would initially generate a photoluminescent CdS NP, followed by the growth of a paramagnetic shell (CoS, perhaps) at the CdS surface. This would create a second 'molecular handle,' sensitive to the external magnetic field, coupled to the 'molecular handle' of the amphiphilic diblock copolymer, sensitive to self-assembly forces exerted by the air-water interface. The combination and competition of these forces should lead to another level of structural control at the interface of the Langmuir trough. It would be interesting to observe the effect of applying the magnetic field both during the initial self assembly event, when sufficient mobility is still available to the polymer (i.e. the solvent has not completely evaporated), and also after the kinetically-locked aggregates are formed so that the magnetic field would direct the orientation of the entire NP / polymer superstructure. Both methods may lead to increased control over the superstructures and their alignment, and provide routes to more efficient and controllable assembly.

Another more applied study concerning these NP / polymer superstructures would be to investigate their optical properties, in particular their potential applications as materials that both emit and direct light (i.e. novel waveguides containing

photoluminescent NPs). The organization of densely-packed CdS NPs within an optically transparent 1D feature of dielectric polymer matrix may prove to be an interesting structure for internally generating photons via photoluminescence, which could then be guided along the length of the nanocable by total internal reflection. To probe this possibility, an interesting study would employ a near-field scanning optical microscope (NSOM), which is a variant of AMF used in this thesis, on the CdS NP / polymer LB films. NSOM has the additional functionality of a sub-wavelength light source (antenna) at the terminus of the tip of a scanning microscope, thus illuminating and probing near-field radiation in regions of the film to a resolution of ~20 nm,[12] while at the same time probing the topography. Recording the local photoluminescence as the tip rasters across the surface of the sample would provide information pertaining to the location of luminescent NPs (note: individual NPs would not be spatially resolved by this technique). Another interesting possibility would be to couple a focused laser light source to a detecting tip located at some distance from the illuminating source on the same nanocable. If light were to propagate through the NP / polymer aggregate, it should be detectable in the near-field (at the surface of the nanocable) at a certain distance from the illumination point. Such experiments would permit fundamental analysis of potential photonic applications of our 1D NP / polymer superstructures. Studies geared to photonic applications could be continued by varying the interparticle distance between the individual NPs (controlled predominately by the length of the PS brush on the PS-CdS) in an effort to tune the photoluminescent properties via dipole-dipole coupling and through-space energy transfer between NPs.

5.3 References

(1) Cox, J. K.; Yu, K.; Constantine, B.; Eisenberg, A.; Lennox, R. B. *Langmuir* **1999,** *15*, 7714.

(2) Devereaux, C. A.; Baker, S. M. *Macromolecules* **2002**, *35*, 1921.

(3) Cheyne, R. B.; Moffitt, M. M. *Langmuir* **2005**, *21*, 5453.

(4) Baker, S. M.; Leach, K. A.; Devereaux, C. E.; Gragson, D. E. *Macromolecules* **2000**, *33*, 5432.

(5) Li, S.; Clarke, C. J.; Lennox, R. B.; Eisenberg, A. *Colloids and Surfaces A* **1998**, *133*, 191.

(6) Li, S.; Clarke, C. J.; Eisenberg, A.; Lennox, R. B. *Thin Solid Films* **1999**, *354*, 136.

(7) Seo, Y. I., J.-H.; Lee, J.-S.; Kim, J.-H. *Macromolecules* **2001**, *34*, 4842.

(8) Bijsterbosch, H. D.; de Haan, V. O.; de Graaf, A. W.; Mellema, M.; Leermakers, F. A. M.; Cohen Stuart, M. A.; van Well, A. A. *Langmuir* **1995**, *11*, 4467.

(9) Dewhurst, P. F.; Lovell, M. R.; Jones, J. L.; Richards, R. W.; Webster, J. R. P. *Macromolecules* **1998**, *31*, 7851.

(10) Briscoe, B. J.; Galvin, K. P. *J. Phys. D: Appl. Phys.* **1990**, *23*, 1265.

(11) Srinivasarao, M.; Collings, D.; Philips, A.; Patel, S. *Science* **2001**, *292*, 79.

(12) Pohl, D. W., Scanning Near-Field Optical Microscopy. In *Advances in Optical and Electron Microscopy*, ed.; Sheppard, C. J. R.; Mulvey, T., Academic Press, 1990, Vol. 12.